Dissertation

submitted to the

Combined Faculties of the Natural Sciences and Mathematics

of the Ruperto-Carola-University of Heidelberg, Germany

for the degree of

Doctor of Natural Sciences

Put forward by

Dipl.-Phys. Daniel Hengstler

born in: Villingen-Schwenningen

Oral examination: 30. November 2017

Development and characterization of two-dimensional metallic magnetic calorimeter arrays for the high-resolution X-ray spectroscopy

Referees: Prof. Dr. Christian Enss
            Prof. Dr. Heinz Horner

In the framework of this thesis the new two-dimensional detector array *maXs30* was developed, fabricated and characterized. It is optimized for high-resolution X-ray spectroscopy in the energy range up to 30 keV and consists of 8x8 individual metallic magnetic calorimeters. These detectors combine the good energy resolution of crystal spectrometers and the large energy bandwidth of semiconductor detectors and measure the energy of each absorbed photon by the resulting temperature change. This change is converted to a change of magnetization by the paramagnetic alloy Ag:Er, which is read out by sensitive SQUID magnetometers. The detector can be mounted on the side arm of a mobile dry dilution refrigerator and a new 32 channel acquisition system has been developed for this array. The intrinsic energy resolution of the *maXs30* detector was measured to be 7.9 eV (FWHM) and a resolving power of almost 3000 was achieved for X-rays with an energy of 60 keV. The complete *maXs* system was successfully tested during several experiments at the heavy ion storage ring ESR at the GSI, where the Lyman series of Xe^{53+} and the Balmer series of U^{89+} were investigated.

Entwicklung und Charakterisierung von zweidimensionalen Arrays aus metallischen magnetischen Kalorimetern für die hochauflösende Röntgenspektroskopie

Im Rahmen der vorliegenden Arbeit wurde das neue zweidimensionale Detektor-Array *maXs30* entwickelt, hergestellt und charakterisiert. Es ist für die hochauflösende Röntgenspektroskopie im Energiebereich bis 30 keV optimiert und besteht aus 8x8 einzelnen metallischen magnetischen Kalorimetern. Diese Detektoren kombinieren die gute Energieauflösung von Kristallspektrometern und die hohe Energiebandbreite von Halbleiterdetektoren und messen die Energie jedes einzelnen Photons durch die Temperaturerhöhung bei dessen Absorption. Diese wird durch das paramagnetische Material Ag:Er in eine Magnetisierungsänderung umgewandelt, welche durch SQUID-Magnetometer ausgelesen wird. Das Detektor-Array wird am Ende eines Auslegers eines mobilen trockenen Verdünnungskryostaten betrieben. Für das Array wurde ein neues 32-Kanal Datenaufnahmesystem entwickelt. Die intrinsische Energieauflösung des *maXs30*-Detektors wurde zu 7.9 eV (FWHM) bestimmt und ein Auflösungsvermögen von beinahe 3000 für Röntgenenergien um 60 keV erreicht. Das komplette *maXs*-System konnte im Rahmen mehrerer Experimente am Schwerionen-Speicherring ESR der GSI getestet werden, wo unter anderem die Lyman-Serie von Xe^{53+} und die Balmer-Serie von U^{89+} untersucht wurden.

Contents

1. Introduction

Since the publication of the spectral nature of light by Sir Isaac Newton [New30] and the major technical advances in optical spectroscopy by Joseph von Frauenhofer and his investigation of the solar spectrum [Fra17], followed by the development of analytical spectroscopy by Gustav Kirchhoff and Robert Bunsen in the 1860s [Kir60], energy- or wavelength-dispersive spectroscopy of light became an important field of research. The pioneering work by William Lawrence Bragg and William Henry Bragg in the beginning of the 20th century advanced spectroscopy in the X-ray regime, allowing access to the electronic structure of heavier atoms. Since then X-ray spectroscopy became a powerful and important tool in different fields of physics, including material analysis, astronomy and last but not least atomic physics. The theoretical foundation of atomic physics is nowadays given by quantum electrodynamics (QED) which is one of the most precisely tested theories in physics. It strongly evolved after the observation of a small deviation in the atomic structure of the hydrogen atom with respect to the Dirac theory in an experiment by Lamb and Retherford in 1947 [Lam47]. This so-called Lamb shift is attributed to fluctuations of the QED vacuum and can, therefore, be used for high-precision tests of this theory. As it scales with the fourth power of the nuclear charge Z, while the binding energies scale only as Z^2, heavy and highly-charged ions like hydrogen-like U^{91+} are ideal candidates to investigate higher order corrections of QED. Due to the relatively small distance between the innermost electron and the nucleus, they are also highly sensitive to nuclear size effects and additionally allow the study of QED in very intense electric and magnetic fields. However, the corresponding transition energies in such ions are in the range of $10\,keV$ up to more than $100\,keV$ and request detectors with a high energy resolution for such X-rays.

The current working horse for such experiments are semiconductor detectors (i.e. Si or Ge based detectors) that provide a high energy bandwidth and fast response times which allow for coincidence measurements. However, typical commercially available Si(Li) detectors[1] are limited to energy resolutions of about $140\,eV$ at $6\,keV$ that further degrade with the square root of the photon energy. Crystal spectrometers on the other hand are able to provide energy resolutions down to $1\,eV$ [Kub14] in the keV-range and below $100\,eV$ around $50\,keV$ [Cha06], however, suffer from a very small acceptance range and a small detection efficiency. A type of X-ray detector that provides a high energy bandwidth as well as a high energy resolution are low temperature micro-calorimeters that were first proposed in 1935 by F. Simon [Sim35].

---

[1]CANBERRA GmbH, Walter-Flex-Str. 66, 65428 Rüsselsheim, Germany

Such a detector determines the energy of single photons by measuring the temperature change that follows the absorption of each single photon in the detector. Since appropriate cooling-techniques have become available in the 1980s, the development of this detector type has rapidly accelerated, resulting in detectors with energy resolutions below $2\,\mathrm{eV}$ at $6\,\mathrm{keV}$ [Smi12, Heu11]. Several different techniques for the read-out of the temperature were developed, including thermistors [McC05], transition edge sensors [Irw05] and magnetic calorimeters [Büh88, Ens00]. In recent years micro-calorimeters were applied to first measurements investigating atomic physics at electron beam ion traps [Por08] or storage rings [Kra17].

In the case of metallic magnetic calorimeters (MMCs) the temperature rise is monitored by a paramagnetic temperature sensor which is operated in a weak magnetic field. The alignment of the magnetic moments with respect to the field lines is highly temperature dependent and serves as a measure of the temperature. The magnetization of the sensor couples via a superconducting pick-up coil to a highly sensitive SQUID current sensor which can be read out by an appropriate electronics and acquisition system. Compared to other types of low-temperature micro-calorimeters, MMCs additionally provide fast detector responses as well as a very small and predictable non-linearity. A major challenge for all micro-calorimeters is the small active detection area that typically is in the range of $1\,\mathrm{mm}^2$ or below.

In the framework of this thesis the new two-dimensional metallic magnetic micro-calorimeter array *maXs30*[2] with 8x8 pixels was developed and characterized. It is optimized for X-rays with energies up to $30\,\mathrm{keV}$ and is dedicated to high-precision spectroscopy of highly charged ions. Therefore, in chapter 2 a short summary about atomic physics is given, including the special case of highly charged heavy ions and their relevance for QED tests.

As the detector array is based on metallic magnetic micro-calorimeters, chapter 3 gives an overview over the working principle of such a detector and explains the thermodynamic properties of its different components. This includes the absorber, the paramagnetic temperature sensor that is made of dilute Er^{3+} ions in a noble metal as well as its coupling to the read-out coil. Finally the detector response function and a fundamental limit of the energy resolution is discussed together with important noise contributions.

The design of the new detector array *maXs30* is presented in chapter 4, including the results of an optimization process that leads to an expected energy resolution of below $7\,\mathrm{eV}$. The chapter is concluded by the relevant microfabrication techniques that were used to fabricate the detector chips.

The cryostat that provides the temperatures in the mK-range that are necessary

---

[2]Acronyme for **m**icro-calorimeter **a**rray for **X**-ray **s**pectroscopy for up to $30\,\mathrm{keV}$

to operate the detectors, is introduced in chapter 5 together with other experimental techniques that are used in the experiments that are discussed in this thesis. These also include the working principle and important aspects of the SQUID current sensors that are used to read out the magnetization change of the temperature sensors as well as a new 32-channel data acquisition system that was used for some measurements. Additionally the different radioactive sources that were used to characterize the detectors are introduced together with the relevant components of the gas jet target of the Experimental Storage Ring ESR at the GSI[3], where some of the experiments were performed.

In chapter 6 the experimental results are discussed. First the focus is put on the characterization of the different properties of the *maXs30* detector array, including the detector response function, the energy resolution, the linearity as well as the homogeneity across the 64-pixel array. Finally the results of first experiments at the gas jet target at the GSI, that were performed with a *maXs200* detector and a *maXs30* detector array, are discussed.

---

[3]GSI Helmholtzzentrum für Schwerionenforschung GmbH, Planckstraße 1, 64291 Darmstadt, Germany

2. Motivation and physics of highly charged ions

This chapter gives a short overview about relevant aspects of highly charged heavy ions, while a thorough discussion of the physics of highly charged ions can be found in [Bey97, Bey99]. Heavy atoms with a large nuclear charge Z provide excellent environments for the study of quantum electrodynamics in the limit of strong electromagnetic fields. The innermost electron in uranium, for example, is subject to an electric field strength of about 1×10^{16} V/cm, six orders of magnitude larger than the field strength in hydrogen. This field strength is close to the Schwinger limit above which non-linear effects of the electromagnetic field are expected [Sch51]. However, for heavy atoms the resulting many-body systems are difficult to handle theoretically due to the large number of involved electrons. Therefore, hydrogen-like and other highly charged heavy ions with only few remaining electrons are of special interest.

Atomic radius	Z^{-1}
Ionization potential	Z^2
Transition energy	Z^2
Lamb shift	$\alpha^5 Z^4/n^3$
Fine-structure splitting	$\alpha^2 Z^4$
Hyperfine splitting	$\alpha^2 Z^3$

Table 2.1: Scaling of different quantities of hydrogen-like ions with respect to the nuclear charge Z [Bey97].

Table 2.1 lists the Z-dependence of some properties of highly charged ions, where $\alpha \approx 1/137$ denotes the dimensionless fine structure constant. Like many other quantities that describe the energy levels as well as the transition probabilities in highly charged ions they often scale with higher powers of Z. Among these quantities the Lamb shift gives access to high-precision tests of quantum electrodynamics and is, therefore, further discussed below. Being strongest for the $n = 1$ shell and with a relative effect on the transition energies that scales as Z^2, it makes the high-precision measurement of the $1s$ Lamb shift of U^{91+} a major goal in atomic physics.

2.1 Energy levels in hydrogen-like heavy ions

For an adequate description of the electrons in highly charged ions, the non-relativistic Schroedinger equation does not lead to satisfying results, due to the large potentials involved. Together with the spin-orbit coupling of the electron, the relativistic effects

resulting from these potentials are accounted for by the Dirac equation for spin-1/2 particles. In the stationary case and for an electron with rest mass m belging to a hydrogen-like ion with nuclear point charge Z it is given by

$$(-i\hbar c\boldsymbol{\alpha}_k\nabla_k + \boldsymbol{\beta}mc^2 - \frac{Ze^2}{r})\Psi = E\Psi \tag{2.1}$$

with $\boldsymbol{\alpha}_k = \begin{pmatrix} 0 & \boldsymbol{\sigma}_k \\ \boldsymbol{\sigma}_k & 0 \end{pmatrix}$, where $\boldsymbol{\sigma}_k$ denotes the Pauli matrices and $\boldsymbol{\beta} = \begin{pmatrix} \mathbb{1} & 0 \\ 0 & -\mathbb{1} \end{pmatrix}$, with $\mathbb{1}$ being the 2x2-unit matrix.

For the assumed pointlike nucleus the resulting exact solution for the eigenenergies

$$E_{\text{njlm}} = mc^2 \left(1 + \left(\frac{\alpha Z}{n - (j + 1/2) + \sqrt{(j + 1/2)^2 - (\alpha Z)^2}}\right)^2\right)^{-1/2} \tag{2.2}$$

of a state with total angular momentum j can be calculated analytically, where j is given by the sum $\mathbf{j} = \mathbf{l} + \mathbf{s}$ of angular momentum $\mathbf{l}$ and electron spin $\mathbf{s}$. Expanding the result in powers of $\alpha^2 Z^2$ the non-relativistic leading-order term

$$E_0 = -Ry\frac{Z^2}{n^2} \tag{2.3}$$

is obtained with the Rydberg energy $Ry = 1/2mc^2\alpha^2 = 13.6\,\text{eV}$ and the the principal quantum number n. The first-order correction

$$\Delta E_1 = -Ry\frac{Z^4\alpha^2}{n^3}\left(\frac{1}{j + 1/2} - \frac{3}{4n}\right) \propto \alpha^2 Z^4 \tag{2.4}$$

for a state with total angular momentum j describes the shift and splitting of the energy levels due to the fine-structure and includes the relativistic effects as well as the spin-orbit coupling.

Lamb shift   Typically the term Lamb shift is used to denote the difference between the measured binding energy of the electron and the one calculated from solving the Dirac equation for a point nucleus. Besides the finite nuclear size, the two dominant contributions to this shift are electron self-energy and vacuum polarization. Additional small contributions to the Lamb shift are given by nuclear recoil and nuclear polarization corrections. While the finite size of the nucleus can be included in the Dirac equation by choosing an appropriate potential, the self-energy of the

electron and vacuum polarization are treated by quantum electrodynamics and can be described with

$$\Delta E_{\mathrm{lamb}} = \frac{\alpha}{\pi} \frac{(\alpha Z)^4}{n^3} F_{\mathrm{l}}(\alpha Z) m_{\mathrm{e}} c^2 \ , \tag{2.5}$$

where

$$F_{\mathrm{l}}(\alpha Z) \approx \begin{cases} 1, & \text{if } l \neq 0 \\ \ln{(\alpha Z)^{-2}}, & \text{otherwise} \end{cases} \tag{2.6}$$

is a dimensionless function [Bey97].

The self-energy of the electron results from the interaction of the electron itself with its own radiation field, i.e. the emission and reabsorption of virtual photons. The vacuum polarization on the other hand describes the excitation of virtual electron-positron pairs by the interaction photon that mediates the Coulomb interaction between the electron and the nucleus. The corresponding theoretical values for the different contributions to the Lamb shift of the ground state of hydrogen-like uranium U^{91+} are listed in table 2.2.

Contribution	Energy [eV]
Finite nuclear size	198.7
1st order self-energy	355.0
1st order vacuum polarization	-88.6
Nuclear recoil	0.5
Nuclear polarization	-0.2
2nd order QED	±2

Table 2.2: Contributions to the ground state Lamb shift in U^{91+}. Taken from [Bey97].

In light ions ($\alpha Z \ll 1$) the equations 2.3 to 2.5 give a very good approximation of the energy levels and transition energies. Hydrogen-like ions with large nuclear charge Z are, however, sensitive to higher order corrections and for $\alpha Z \to 1$ theoretical approaches based on perturbation theorys with αZ as extension parameter, are no longer valid.

Hyperfine structure An additional, small correction is necessary due to the interaction of the electron spin with the spin of the nucleus. It can be as large as 5 eV in $^{209}\mathrm{Bi}^{82+}$ [Kla94] but can be neglected for many other highly charged ions.

2.2   Transitions in hydrogen-like heavy ions

Figure 2.1 depicts the level structure of hydrogen-like ions including the first three shells and neglecting the hyperfine splitting. Here, the total quantum state of the ion is written as nx_j, where $x = \{s, p, d, f\}$ stands for $l = \{0, 1, 2, 3\}$. From the conservation of the angular momentum $\mathbf{l}$ one can derive selection rules for allowed transitions and finds for the electric dipole (E1) transitions: $\Delta l = \pm 1$ and $\Delta j = 0, \pm 1$. The corresponding transitions are marked with solid lines. The Lyα and Lyβ transitions are part of the Lyman series which contains all the transitions where the final state of the electron corresponds to its ground state, while transitions where the electron in the final state is found in the $(n = 2)$-shell are called Balmer transitions.
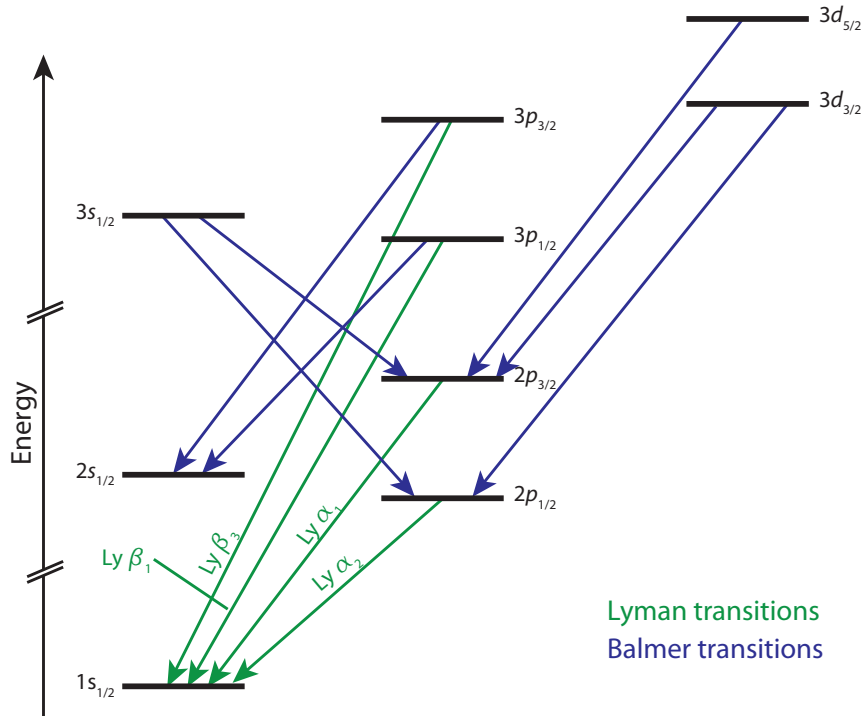
Figure 2.1: E1 transitions in hydrogen-like ions. Lyman transitions are marked in green, while Balmer transitions ending in a $n = 2$ state are shown in blue. Not depicted are possible intrashell transitions.

While higher order transitions like magnetic dipole (M1: $\Delta l = 0$ and $\Delta j = 0, \pm 1$) or electric quadrupole (E2: $\Delta l = 0, \pm 2$ and $\Delta j = 0, \pm 1, \pm 2$) transitions are strongly suppressed in normal hydrogen, the probabilities for these transitions increase rapidly for highly charged ions as shown in table 2.3. For $Z > 40$ the M1 transition from the $2s_{1/2}$ state is even stronger than the rivaling two-photon (2E1) decay [Bey97].

	H ($Z = 1$)	Xe ($Z = 54$)	U ($Z = 92$)
M1: $2s$-$1s$	$2.5 \times 10^{-6}\,\text{s}^{-1}$	$6.3 \times 10^{11}\,\text{s}^{-1}$	$1.9 \times 10^{14}\,\text{s}^{-1}$
Lyα_1	$6.3 \times 10^{8}\,\text{s}^{-1}$	$5.1 \times 10^{15}\,\text{s}^{-1}$	$4.0 \times 10^{16}\,\text{s}^{-1}$
Lyα_2	$6.3 \times 10^{8}\,\text{s}^{-1}$	$5.4 \times 10^{15}\,\text{s}^{-1}$	$4.7 \times 10^{16}\,\text{s}^{-1}$

Table 2.3: Transition probabilities for $(n = 2) \rightarrow (n = 1)$ transitions in highly charged hydrogen-like ions. Taken from [Bey97].

2.3 Helium-like ions

Helium-like ions, i.e. ions with only two remaining electrons, show a much more complicated level structure compared to hydrogen-like ions due to the additional interactions between the two electrons. As simplest many-electron systems they are of special interest to study electron-electron interactions and for tests of parity violating effects [Kar92].

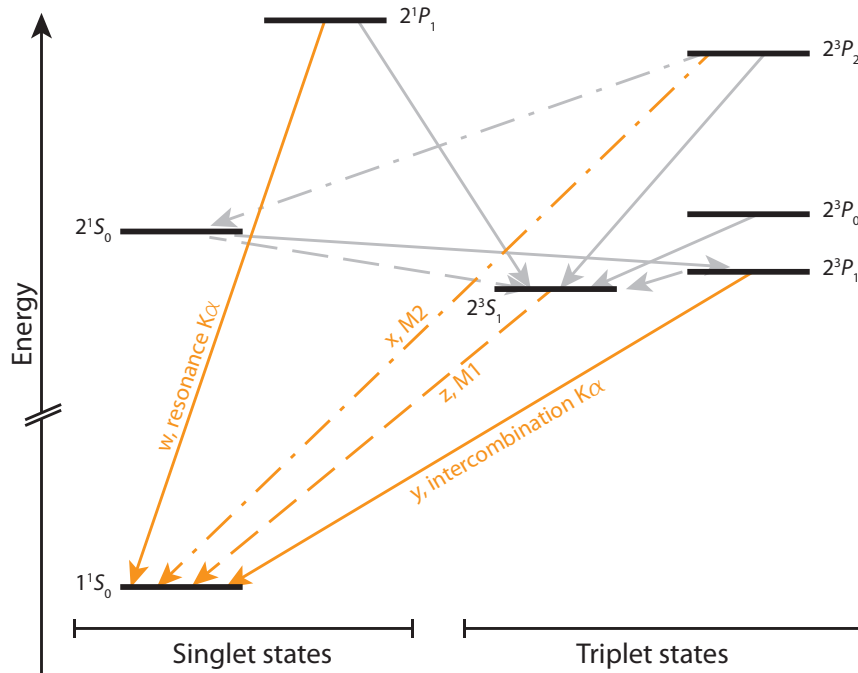**Figure 2.2:** Level scheme and transitions in singly excited helium-like ions. Intrashell transitions are marked in grey, while $(n = 2) \rightarrow (n = 1)$ transitions are marked in orange. Solid lines mark electric dipole transitions, while M1 and M2 transitions are marked with dashed lines. Four relevant transitions in helium-like heavy ions with $Z > 20$ are labeled in Gabriel's notation [Gab72].

Figure 2.2 schematically shows the corresponding level structure for singly excited ions including fine structure and Lamb shift for the first two shells. Here, the notation $n\,^{2S+1}X_J$ is used, where n describes the principal quantum number and $X = \{S, P, D, F\}$ the azimuthal quantum number of the excited electron, while S and J correspond to the total spin $\mathbf{S} = \mathbf{s_1} + \mathbf{s_2}$ and total angular momentum $\mathbf{J} = \mathbf{j_1} + \mathbf{j_2}$ of both electrons. Depicted with solid lines are the E1 single-photon transitions according to the selection rules $\Delta L = \pm 1$ and $\Delta J = 0, \pm 1$, with $J = 0 \nrightarrow J = 0$. While in light atoms with $Z < 20$ the $\mathbf{L} \cdot \mathbf{S}$ coupling and the selection rule $\Delta S = 0$ are still valid for one-electron transitions and transitions between triplet ($S = 1$) and singlet ($S = 0$) states are forbidden, this no longer is valid for heavy ions where $\mathbf{j} \cdot \mathbf{j}$ coupling has to be taken into account due to the much stronger electromagnetic fields. For large nuclear charge Z, however, the $2\,^3P_1$ state can decay via mixing with the $2\,^1P_1$ state to the ground state with a transition probability that is rapidly increasing with Z and that is 14 orders of magnitude larger in U^{90+} than in He. Similarly, the probability for the M1 transition from the $2\,^3S_1$ state to the ground state scales with Z^{10}. For the $2\,^3P_2$ state the direct decay to the ground state is the dominating decay path for ions with $Z > 20$, with a probability that is proportional to Z^8.

2.4 Lithium-like ions

In singly excited lithium-like ions, where the first shell is fully occupied by two electrons, the resulting level scheme and transitions correspond to the Balmer lines in hydrogen-like ions indicated in blue in figure 2.1. However, the associated transition energies differ from hydrogen-like ions as a part of the nuclear charge is screened by the two innermost electrons.

3. Theoretical background of metallic magnetic calorimeters

The detector array developed in the framework of this thesis that is discussed in detail in chapter 4 is based on metallic magnetic calorimeters. This chapter describes the theoretical background needed to understand the properties of such detectors and the behaviour after the absorption of a photon. At the beginning an overview about the working principle is given and thereafter the different parts of the detector will each be adressed in more detail.

3.1 Working principle

A metallic magnetic calorimeter can be used to precisely measure the energy of single X-ray photons. Figure 3.1 shows a schematic drawing of the different parts of such a detector.
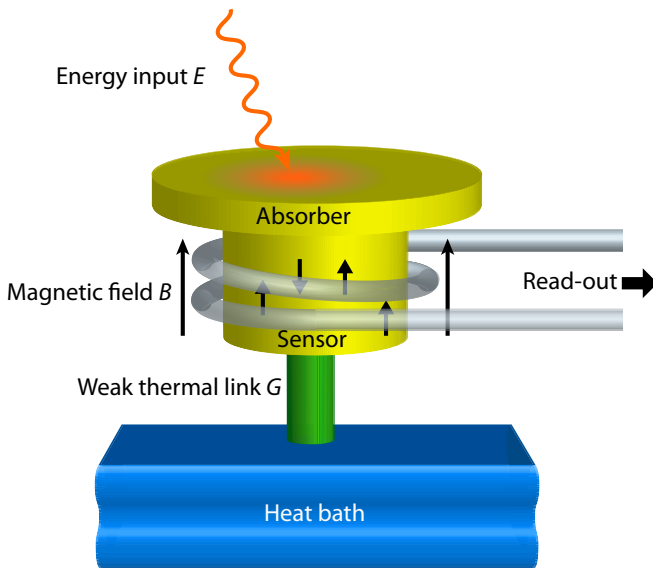
Figure 3.1: Schematic drawing of a metallic magnetic calorimeter consisting of a particle absorber and a paramagnetic temperature sensor in a weak magnetic field that is read out via a superconducting pick-up coil and coupled to a thermal bath by a weak link.

The photons are absorbed within a particle absorber and according to the first law of thermodynamics, the energy E of each photon is thereby converted to a temperature change

$$\Delta T \simeq \frac{E}{C_{\text{tot}}} \ .$$

(3.1)

11

Here C_{tot} denotes the total heat capacity of the detector consisting of the heat capacities of the absorber itself as well as the attached temperature sensor that is used to monitor the temperature change. In first order this heat capacity can be seen as temperature-independent for $\Delta T \ll T$ where T is the working temperature of the detector. As will be shown in chapter 3.2 the choice of the absorber dimensions and its material is relevant for the total absorption efficiency and can be used to adjust energy resolution and active detector area in order to optimize the detector for given experimental constraints.

For a precise determination of the small temperature rise ΔT which is in the order of $100\,\mu\text{K}$ to $1\,\text{mK}$ for the detectors used in this thesis, magnetic calorimeters make use of a paramagnetic temperature sensor. It is in good thermal contact to the absorber, ensuring a fast and complete thermalization of both, absorber and sensor. In a small magnetic field such a material obeys a temperature-dependent magnetization $M(T)$. The temperature change ΔT thus leads to magnetization change

$$\Delta M \simeq \frac{\partial M}{\partial T} \Delta T \ .$$

(3.2)

The sensors used in this thesis are made of silver or gold that is doped with several hundred ppm of the rare-earth element erbium to form a paramagnetic material. The properties of this material are discussed in chapter 3.3.1. The use of a metallic host lattice allows for signal rise times below $100\,\text{ns}$ [Fle09] due to the good coupling between magnetic moments and electrons. These rise times are much faster than the ones for a dielectric host material like Er-doped yttrium aluminium garnet [Büh88] which are connected with the coupling between magnetic moments and phonons. Keeping the rise time of a signal small is especially important in experiments where timing capability is needed, e.g. for coincidence measurements. However, the use of a metallic host comes along with an increased heat capacity due to conduction electrons as well as a stronger coupling between the magnetic moments. Both effects in turn reduce the signal height. After the temperature rise the detector thermalizes again with a heat bath through a weak thermal link, leading to an exponential drop in magnetization. A large decay time increases the dead time of the detector thus limiting the achievable count rate.

The change of sensor magnetization corresponds to a change of magnetic flux

$$\Delta \Phi \propto \Delta M \simeq \frac{\partial M}{\partial T} \frac{E}{C_{\text{tot}}}$$

(3.3)

that is picked-up by a superconducting loop and finally read out by a highly sensitive SQUID[1] magnetometer that will be introduced in section 5.2.1. Details of

---

[1]Superconducting QUantum Interference Device

the pick-up loop and its coupling to the magnetic moments will be discussed in chapter 3.4. According to equation 3.3 it is favorable to decrease the total heat capacity C_{tot} of the detector in order to increase the signal size. This can be done by reducing the detector volume as well as by operating the detector at very low temperatures $T < 100\,\text{mK}$. Furthermore, increasing the steepness of the sensor magnetization $M(T)$ also increases the signal size. The signal shape and the optimal energy resolution will be derived in chapter 3.5.

3.2 Particle absorber

Although it would be possible to absorb the X-ray photons directly in the sensor one would be strongly limited in optimizing the detector for various applications. Introducing a separate particle absorber allows to change the material, active detection area and absorber thickness according to the expected count rates, energies and the type of particle that should be absorbed (for example X-ray or γ-photons, molecules, atoms or α-particles). One of the key features that are important for the absorbing material is a small specific heat as according to equation 3.3 the signal height decreases with increasing heat capacity. Furthermore, a fast, complete and homogeneous internal thermalization of the material is important to obtain a predictable signal shape. In applications with low photon flux a large detection area and a high stopping power which typically increases with the atomic number Z and material density ρ are also requested. As for a given material the stopping power can only be increased by increasing the absorber thickness, increasing the total absorption capability of the detector has a direct impact on the absorber volume and thus on the heat capacity. Another constraint that is important especially for large detector arrays is given by the need to fabricate the absorbers and connect them to the temperature sensors in a reproducible and reliable way.

3.2.1 Absorber material

There are several materials that are suitable as a particle absorber for soft and hard X-rays. Figure 3.2 shows the absorption efficiency[2] for some of these materials plotted against the energy of the incident photon. In the following a short overview of the advantages and disadvantages of the different material types is given.

Dielectric materials Dielectric materials show a very small specific heat as only the phonons contribute with a specific heat of $c_{\text{ph}} \propto T^3$. However the electron-

---

[2]The fraction of incident photons that are actually detected by the detector.
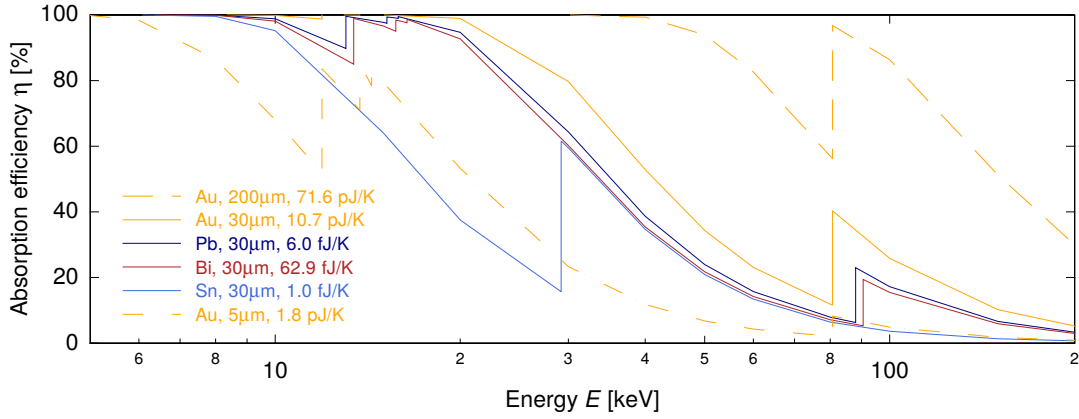
Figure 3.2: Absorption efficiency for several X-ray absorber materials for a given absorber thickness of 30 µm in the energy range of interest for X-ray spectroscopy of highly charged ions. For gold additionally the absorption efficiency for 5 µm and 200 µm thickness are depicted for comparison (data taken from [Hub95]). The corresponding heat capacity of an absorber made of the respective material and with the given thickness and an area of 500 µm × 500 µm at a temperature of 20 mK is also stated. The specific heat values were taken from [Rös04] (Au), [Poo95] (Pb, Sn) and [Col70] (Bi).

hole pairs that are created during the inital interaction between the incoming X-ray photon and the absorber material are very often trapped at lattice defects and recombine only on very long time scales. As the number of trapped electron-hole pairs may change for each registered photon this would lead to a decreased resolving power [McC93].

Superconducting metals   Like dielectrics superconducting materials exhibit a very small specific heat for temperatures far below their critical temperature T_c as electrons that are bound in Cooper pairs no longer contribute to the heat capacity. Thus only the very small phononic contribution remains. Absorbers made of lead and tin have been widely used [Kra13a, Hoo06]. However, most superconducting absorbers have shown a thermalization behaviour that is not yet fully understood [Cos93, Hen12]. This behaviour results most likely from broken Cooper pairs and long relaxation and recombination times of the created quasiparticles. This leads to energy being stored inside the absorber over very long time scales up to several hundreds of milliseconds, whereas intrinsic equilibration times below 1 µs can be achieved when using normal metallic absorbers.

Normal metals   Normal metals benefit from their good thermal conductivity and therefore exhibit a fast and complete thermalization behaviour that can be easily

understood. However, the high thermal conductivity that is provided by the conduction electrons comes along with a contribution to the sepecific heat $c_{\mathrm{e}} \propto T$ that dominates over the second contribution to the specific heat of the phonons $c_{\mathrm{ph}} \propto T^3$ at low temperatures. A very attractive candidate is gold that in addition provides a very large stopping power and can be microfabricated in a reliable manner by all standard techniques including electroplating. The detectors presented in this thesis use absorbers made of gold with a thickness of $30\,\mu\mathrm{m}$ and $200\,\mu\mathrm{m}$, respectively. Another promising candidate is bismuth [Rod14] that, beeing almost a semi metal, exhibits a specific heat per volume that can be more than 150 times smaller than the one of gold at $20\,\mathrm{mK}$ [Col70]. However, also the thermal diffusion is largely suppressed [Iyo04, Hoe06] compared to gold leading to a slower detector response time and a possible degradation in energy resolution [Vai04]. Combinations of Bi and Au [Bro08] or Bi and Cu [Saa07] have been investigated to combine the advantages of both materials.

3.2.2 Thermalization behaviour in absorbers made of gold

In gold the dominating absorption mechanism for X-ray energies below $500\,\mathrm{keV}$ is the photoelectric effect. The following thermalization processes are discussed in detail in [Koz12, Koz00]: The resulting high-energetic electron undergoes electron-electron scattering creating secondary electrons and plasmon[3] excitations that themselves rapidly decay into electron-hole excitations. The resulting non-thermal distribution of electrons further thermalizes mainly by electron-phonon interaction via high-energetic athermal phonons. The complete energy downconversion process typically happens in a small volume on time scales that are faster than the thermal diffusion or the interaction between absorber and temperature sensor and can thus not be resolved by micro calorimeters.

Loss of athermal phonons During the thermalization process it may happen that fast athermal phonons escape the absorber, traverse the temperature sensor and get lost into the substrate without depositing their energy in the detector. This has been observed as a low-energy tail in the spectral lineshape of metallic magnetic calorimeters with high energy resolution [Fle09, Koz13]. This effect can be reduced by introducing stems between absorber and sensor that reduce their direct contact area and thus limit the probability of a direct escape of phonons to the substrate. In [Fle09] it has been shown that such stems can be designed in such a way that they do not limit the signal rise time of the detector.

---

[3]Quantized density oszillations of conduction electrons

Thermalization in large volume absorbers With residual resistivity ratios between $RRR = 5$ and $RRR = 50$ for absorbers made of electroplated gold, thermal diffusion constants between $a = 0.06\,\mathrm{mm^2/\mu s}$ and $a = 0.75\,\mathrm{mm^2/\mu s}$ are possible at $T = 20\,\mathrm{mK}$. Thereby the thermal diffusion may limit the signal rise time in large volume absorbers, resulting in a position dependent signal shape [Pie12] and subsequently in a degradation of energy resolution. The thermal diffusion in gold and its impact on the signal shape is further discussed in [Gam13]. This problem can be cured by introducing a thermal bottleneck between absorber and sensor which limits the signal rise time such that the complete absorber will be thermalized on a timescale shorter than the signal rise time.

3.3   Temperature sensor

The paramagnetic temperature sensor converts the temperature change ΔT of the detector into a change of magnetization that can be read out as shown in chapter 3.4. This conversion is done by a system of magnetic moments which obey a Curie-like behaviour in a magnetic field and therefore show a temperature-dependent alignment with this field. In this chapter the two key properties of the sensor material will be discussed. Both, the specific heat c_z as well as the temperature dependence of the magnetization $M(T)$ will be derived from basic thermodynamic principles.

3.3.1   Sensor material

The detectors that were used in the framework of this thesis are based on sensors made of dilute paramagnetic alloys of the rare-earth metal erbium that has been enriched in ^{168}Er. As a host material silver (Ag:Er) and gold (Au:Er) were used.

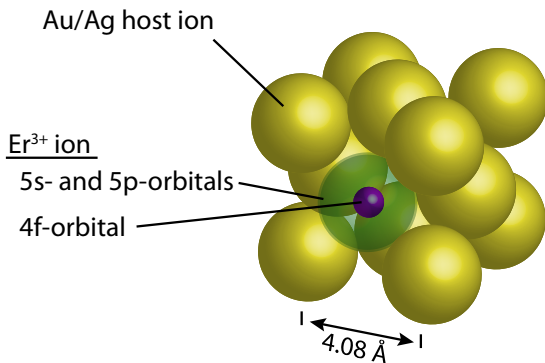**Figure 3.3:** Schematic drawing of a single Er^{3+} ion occupying a regular site in the fcc lattice of the host material. Also shown are the 4f-orbital with the unpaired electrons and the fully occupied larger 5s- and 5p-orbitals.

For the small concentrations of several hundert ppm of erbium, that are typically used for magnetic calorimeters, the erbium atoms occupy regular places in the fcc

lattice defined by the host metal as depicted in figure 3.3 and donate three electrons to the electron gas. The resulting Er^{3+} ions with the electron configuration $[Kr]4d^{10}4f^{11}5s^25p^6$ exhibit a magnetic moment due to the partially filled 4f-shell, where only 11 of the possible 14 electrons are present. As this orbital has a diameter of only $0.6\,\text{Å}$ [Fra76] the 4f-electrons are shielded from the crystal field of the lattice by the surrounding electrons of the 5th shell which has a diameter of $2\,\text{Å}$. We can apply **LS**-coupling and according to Hund's first rule the 4f-electrons arrange in such a way that three electrons remain unpaired and add up to a total spin $S = 3/2$. According to Hund's second and third rule the angular momentum $L = 6$, as well as the total angular momentum $J = L + S = 15/2$ are maximized. The resulting Landé g-factor [Abr70]

$$g_J = 1 + \frac{J(J+1) + S(S+1) - L(L+1)}{2J(J+1)} = \frac{6}{5} \tag{3.4}$$

gives rise to a magnetic moment of

$$\boldsymbol{\mu} = -g_J\mu_B\mathbf{J} \tag{3.5}$$

of the Er^{3+} ion, where $\mu_B = 9.274 \times 10^{-24}\,\text{J/T}$ denotes the Bohr magneton.

At temperatures above $100\,\text{K}$ the parameters above describe the magnetic behaviour of dilute erbium alloys very well [Wil69]. At lower temperatures however, the influence of the crystal field can no longer be neglected which splits the 16fold degenerate groundstate into several multiplets. The energetically most favorable state is a Kramers-Γ_7 doublet and is separated from the next multiplet by $\Delta E/k_B \approx 17\,\text{K}$ [Hah92] in the case of gold as host material and by $\Delta E/k_B \approx 25\,\text{K}$ in the case of Ag:Er [Hah92]. Here $k_B = 8.62 \times 10^{-5}\,\text{eV/K}$ denotes the Boltzmann constant. At the typical working temperatures of magnetic calorimeters below $100\,\text{mK}$ it is thus safe to assume that only the lowest doublet is occupied. Therefore, when a small external magnetic field is applied the system can be described as a two-level system with effective spin $\tilde{S} = 1/2$ and effective Landé g-factor $\tilde{g} = 6.80$ [Abr70]. Below temperatures of $50\,\text{mK}$ to $100\,\text{mK}$ – depending on the erbium concentration and the magnetic field – the influence of the interactions between the magnetic moments increase and they can no longer be treated as non-interacting. The resulting effects will be discussed in section 3.3.3. At even lower temperatures the system shows signs of a spin glass transition [Fle00].

3.3.2   Thermodynamic properties of non-interacting magnetic moments

As shown in section 3.3.1 the properties of Er^{3+} ions in a gold or silver host matrix can be calculated for low concentrations by treating them as an ensemble of independent magnetic moments with effective spin $\tilde{S} = 1/2$ and effective Landé g-factor $\tilde{g} = 6.8$. In a magnetic field B the ground state of the erbium ions exhibits a Zeeman splitting in $2\tilde{S} + 1 = 2$ levels

$$E_\mathrm{i} = m_\mathrm{i}\tilde{g}\mu_\mathrm{B}B \text{ with } m_\mathrm{i} = \pm\frac{1}{2}. \tag{3.6}$$

The complete system of N independent magnetic moments at temperature T has a Helmholtz free energy

$$F = -Nk_\mathrm{B}T \ln z \tag{3.7}$$

with the microcanonical partition function

$$z = \sum_\mathrm{i} \exp\left(-\frac{E_\mathrm{i}}{k_\mathrm{B}T}\right). \tag{3.8}$$

In thermodynamic equilibrium the two levels are occupied according to the Boltzmann distribution and thereby the expectation value for a property A that can take the values a_i in the Eigenstates i is given by

$$\langle A \rangle = \frac{1}{z} \sum_\mathrm{i} a_\mathrm{i} \exp\left(-\frac{E_\mathrm{i}}{k_\mathrm{B}T}\right) \tag{3.9}$$

and we can, therefore, calculate the **heat capacity**

$$C_\mathrm{z} = -T\frac{\partial^2 F}{\partial T^2} = \frac{N}{k_\mathrm{B}T^2}\left(\langle E^2 \rangle - \langle E \rangle^2\right) = Nk_\mathrm{B}\left(\frac{\delta E}{k_\mathrm{B}T}\right)^2 \frac{e^{\delta E/k_\mathrm{B}T}}{\left(e^{\delta E/k_\mathrm{B}T} + 1\right)^2} \tag{3.10}$$

of the whole Zeeman system created by the magnetic moments of the Er^{3+} ions with spin $\tilde{S} = 1/2$ and an energy splitting $\delta E = \tilde{g}\mu_\mathrm{B}B$ of the corresponding two-level system. The resulting curve is shown on the left-hand side of figure 3.4 where the reduced heat capacity $C_\mathrm{z}/Nk_\mathrm{B}$ of an ensemble of N Er3+ ions is plotted against the reduced temperature $k_\mathrm{B}T/\delta E$ for a two-level system with energy splitting $\delta E \propto B$. The heat capacity exhibits a maximum of $C_\mathrm{z} \approx 0.44Nk_\mathrm{B}$ for $k_\mathrm{B}T \approx 0.42\,\delta E$ that is known as Schottky anomaly. In the low and high temperature limit the heat capacity drops to zero as $C_\mathrm{z} \propto e^{-\delta E/k_\mathrm{B}T}$ and $C_\mathrm{z} \propto B^2/T^2$, respectively.
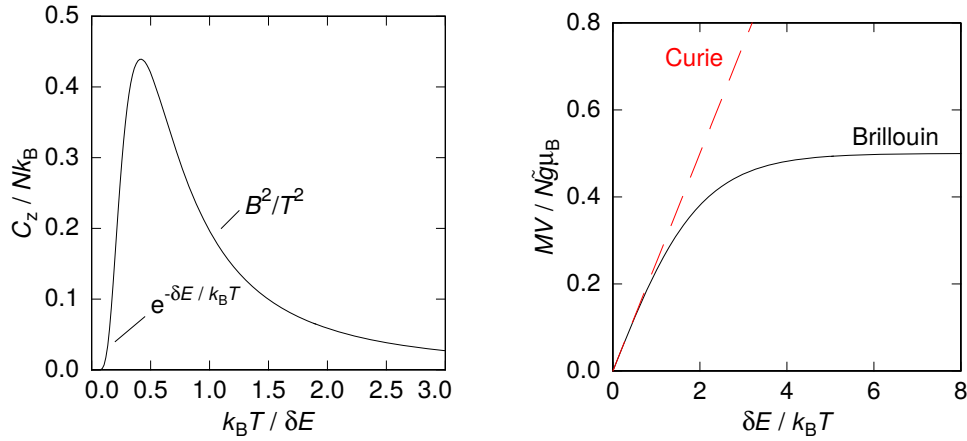
Figure 3.4: Reduced specific heat (**left**) and reduced magnetization (**right**) of a system of N independent two-level systems with energy splitting $\delta E = \tilde{g}\mu_B B$ and spin $\tilde{S} = 1/2$. The high-temperature limit of the magnetization is also depicted.

The **magnetization** of an ensemble of N magnetic moments with spin $\tilde{S}$ in a volume V and in a magnetic field[4] B is given by

$$M = -\frac{1}{V}\frac{\partial F}{\partial B} = -\frac{N}{V}\left\langle\frac{\partial E}{\partial B}\right\rangle = \frac{N}{V}\tilde{g}\tilde{S}\mu_B \mathcal{B}_{\tilde{S}}\left(\frac{\tilde{g}\tilde{S}\mu_B B}{k_B T}\right) \tag{3.11}$$

with the Brillouin function $\mathcal{B}_{\tilde{S}}$ which is $\mathcal{B}_{1/2}(x) = \tanh(x)$ for $\tilde{S} = 1/2$. The right-hand side of figure 3.4 shows the resulting reduced magnetization $MV/N\tilde{g}\mu_B$ of N spin $1/2$ systems. One should note that the scaling of the x-axis is inversely proportional to T. For $T \to \infty$ the known Curie behaviour

$$M \propto \frac{B}{T} \tag{3.12}$$

can be found while for low temperatures ($k_B T \ll \delta E$) the whole system saturates at $M = \frac{N}{V}\tilde{g}\tilde{S}\mu_B$ as more and more magnetic moments are aligned in parallel to the magnetic field.

By calculating the number of spins

$$\Delta N = \frac{\Delta E_z}{\delta E} = \frac{\Delta E_z}{\tilde{g}\mu_B B} = \frac{C_z \Delta T}{\tilde{g}\mu_B B} \tag{3.13}$$

that are flipped by an energy change $\Delta E_z = C_z \Delta T$ of the Zeeman system that is

---

[4]In most places we don't distinguish between flux density B and magnetic field H and we use B for both properties. Wherever needed we distinguish between B and H.

itself caused by a temperature rise ΔT and calculating the subsequent change of magnetization

$$\Delta M = -\frac{1}{V}\Delta N \tilde{g}\mu_\mathrm{B} = -\frac{1}{VB}C_\mathrm{z}\Delta T = \frac{\partial M}{\partial T}\Delta T \qquad (3.14)$$

one can see that the magnetization and the heat capacity of an ensemble of non-interacting magnetic moments are connected by

$$C_\mathrm{z}(B,T) = -VB\frac{\partial M(B,T)}{\partial T} \ . \qquad (3.15)$$

3.3.3   Thermodynamic properties of interacting magnetic moments

The results derived in section 3.3.2 for the heat capacity and magnetization of non-interacting magnetic moments show a qualitatively good agreement with the experimental behaviour of magnetic calorimeters, but quantitatively deviations can be found due to the finite interaction strength between the magnetic moments of the Er^{3+} ions in the sensor material. The sources of these interactions are thoroughly discussed in [Sch00]. While the direct exchange interaction due to an overlap of the wavefunctions of the 4f-electrons can be neglected, two other types of interaction are present.

The first one is the indirect **RKKY**[5] **interaction** [Rud54, Kas56, Yos57] between two dipoles of distance r_{ij} with effective spins $\tilde{\mathbf{S}}_i$ and $\tilde{\mathbf{S}}_j$ that is mediated by the spins of the electrons of the host metal. It can be described with the Hamiltonian

$$\mathcal{H}_{i,j}^{\mathrm{RKKY}} = \Gamma_{\mathrm{RKKY}}\left(\tilde{\mathbf{S}}_i \cdot \tilde{\mathbf{S}}_j\right)F\left(2k_\mathrm{F}r_{ij}\right) \qquad (3.16)$$

and the Kittel-function

$$F(x) = \frac{1}{x^3}\left(\cos x - \frac{\sin x}{x}\right) \ , \qquad (3.17)$$

where k_F denotes the Fermi wave vector of the conduction electrons of the host metal. In first order this interaction is isotropic and favors parallel or antiparallel alignment depending on the distance between the two magnetic moments. Additionally there

---

[5]Ruderman-Kittel-Kasuya-Yosida

is the **dipole-dipole interaction** that can be expressed by the Hamiltonian

$$\mathcal{H}_{i,j}^{\mathrm{dd}} = \Gamma_{\mathrm{dd}} \frac{\tilde{\mathbf{S}}_i \cdot \tilde{\mathbf{S}}_j - 3\left(\tilde{\mathbf{S}}_i \cdot \hat{\mathbf{r}}_{ij}\right)\left(\tilde{\mathbf{S}}_j \cdot \hat{\mathbf{r}}_{ij}\right)}{\left(2k_{\mathrm{F}} r_{ij}\right)^3} \tag{3.18}$$

and exhibits an anisotropic behaviour. Here, $\hat{\mathbf{r}}_{ij} = (\mathbf{r}_i - \mathbf{r}_j)/|\mathbf{r}_i - \mathbf{r}_j|$ denotes the unit vector between the two magnetic moments. The interaction strength expressed by the parameter $\Gamma_{\mathrm{dd}} = (\mu_0/4\pi)(\tilde{g}\mu_{\mathrm{B}})^2(2k_{\mathrm{F}})^3$ depends on the effective Landé g-factor $\tilde{g}_{\mathrm{Au}} = 6.80$ and $\tilde{g}_{\mathrm{Ag}} = 6.84$ [Tao71], respectively. With $k_{\mathrm{F}} = 1.2 \times 10^{10}\,\mathrm{m}^{-1}$ [Kit05] for both discussed host metals gold and silver we calculate $\Gamma_{\mathrm{dd}}^{\mathrm{Au}} = 0.0343\,\mathrm{eV}$ and $\Gamma_{\mathrm{dd}}^{\mathrm{Ag}} = 0.0347\,\mathrm{eV}$. As the strengths of both interactions show the same r^{-3} dependence we can describe their strengths relative to each other with the interaction parameter $\alpha = \Gamma_{\mathrm{RKKY}}/\Gamma_{\mathrm{dd}}$. Unlike the dipole-dipole interaction that is almost independent of the two considered host materials, the RKKY-interaction can be described most precisely with $\alpha = 5$ for $\underline{\mathrm{Au}}$:Er [Fle03], while it is much stronger in the case of $\underline{\mathrm{Ag}}$:Er where $\alpha \approx 15$ provides a good description of the experimental data [Bur08]. The interactions between the magnetic moments could be taken into account in our model by using mean field approximation, but this would imply several approximations and neglect the dipole-dipole interaction. In [Sch00, Fle03] an exact numerical diagonalization of the complete Hamiltonian including the dipole-dipole and the RKKY interaction of up to 10 magnetic moments on a finite cubic lattice with an edge length of about 10 to 20 atoms was performed and the resulting curves for heat capacity and magnetization were compared with results from mean field simulations as well as measurements.
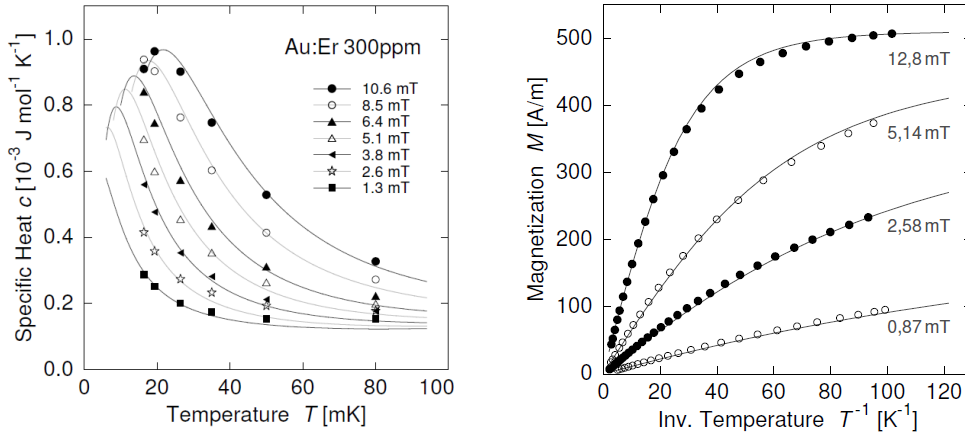
Figure 3.5: Specific heat **(left)** and magnetization **(right)** of a $\underline{\mathrm{Au}}$:Er sensor with an Er^{3+} concentration of $300\,\mathrm{ppm}$ in dependence of the temperature T and magnetic field B, taken from [Fle03]. Shown are experimental data (symbols) as well as simulations (lines) based on the exact diagonalization of the interaction hamiltonian.

The results based on the exact diagonalization are shown in figure 3.5 for a $\underline{\text{Au}}$:Er sample with an Er^{3+} concentration of 300 ppm and are compared to experimental data. Both, the specific heat of the sensor material on the left-hand side as well as the magnetization on the right-hand side show a good agreement between simulation and experiment for different external magnetic fields and temperatures. Comparing the specific heat with the simple model based on non-interacting magnetic moments as depicted in figure 3.4 reveals a qualitatively similar temperature dependence. However, due to the interactions the maximum value of the specific heat is decreased while the Schottky peak broadens with increasing Er^{3+} concentration. The specific heat on the high-temperature side of the curve however increases for larger concentrations and strong interactions. For comparison the electronic specific heat $c_{\text{e}} \propto T$ scales linearly with temperature and has a small but visible effect at higher temperatures for sensors in small magnetic fields, while the phononic contribution scales with $c_{\text{ph}} \propto T^3$ and can be completely neglected in the considered temperature range. The magnetization of the sensor that is plotted versus the inverse temperature T^{-1} exhibits saturation effects already at higher temperatures than in the case of non-interacting magnetic moments. This directly leads to a decrease of the temperature dependence of the magnetization $\partial M/\partial T$ and therefore to a decrease of signal size of the detector.

The good agreement between experiment and theory shows that the thermodynamic properties of erbium-doped noble metals can be well understood. Therefore, it is possible to numerically calculate the detector behaviour based on these simulations and to optimize sensor properties like thickness and Er^{3+} concentration according to experimental needs.

3.3.4 Signal height

As shown in chapter 3.4 the actual signal height of a metallic magnetic calorimeter is directly proportional to the change of magnetization of the sensor. For an energy input E into the absorber the resulting change of magnetization is given by equations 3.1 and 3.2. Based on the simulations described in section 3.3.3 we can calculate the total change of the magnetic moment $\Delta m = V\Delta M$ of a temperature sensor with volume V. Figure 3.6 shows the resulting change Δm per energy input E into a detector for a temperature sensor made of $\underline{\text{Au}}$:Er that is situated in a homogeneous magnetic field B and attached to an absorber made of gold. The simulations are based on an absorber with dimension $500\,\mu\text{m} \times 500\,\mu\text{m} \times 30\,\mu\text{m}$ and a sensor with an erbium concentration of 366 ppm and a size of $300\,\mu\text{m} \times 300\,\mu\text{m} \times 4\,\mu\text{m}$. It also includes interactions between the individual Er^{3+} ions as discussed in section 3.3.3, including a RKKY-interaction with an interaction parameter $\alpha = 5$.
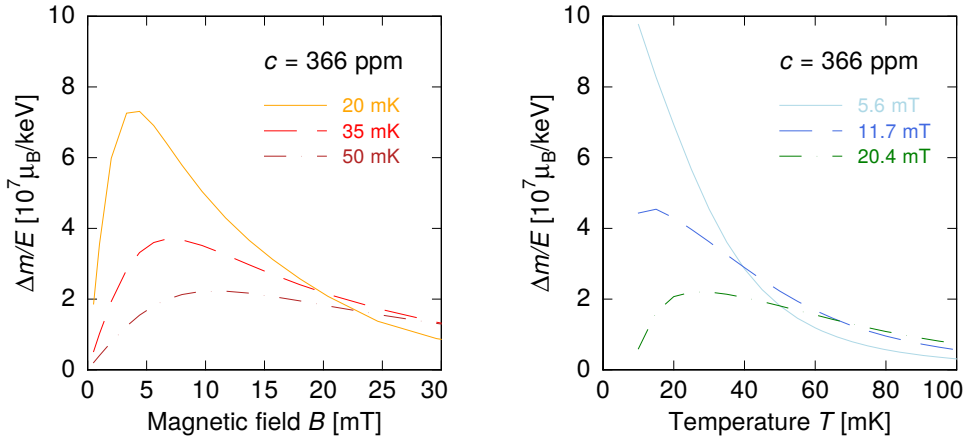
Figure 3.6: Calculated signal height of a paramagnetic <u>Au</u>:Er sensor with an Er^{3+} concentration of 366 ppm per energy input E into the detector in dependence of the applied magnetic field **(left)** and the detector temperature **(right)**. The assumed temperature sensor has a volume of $300\,\mu\text{m} \times 300\,\mu\text{m} \times 4\,\mu\text{m}$ and the attached absorber made of gold a volume of $500\,\mu\text{m} \times 500\,\mu\text{m} \times 30\,\mu\text{m}$. For all calculations a homogeneous magnetic field is assumed.

In the assumption of non-interacting moments the depicted behaviour can be understood by transforming equation 3.14 into

$$\Delta m(B,T) \simeq \frac{C_{\text{z}}(B,T)}{C_{\text{z}}(B,T) + C_{\text{e}}(T) + C_{\text{ph}}(T)} \frac{E}{B} \tag{3.19}$$

using equation 3.1 and the total heat capacity $C_{\text{tot}} = C_{\text{z}} + C_{\text{e}} + C_{\text{ph}}$ of the detector. On the left-hand side the change of the magnetic moment is plotted versus the magnetic field strength. For very small fields, the electronic heat capacity C_{e} dominates and we get a linear dependence $\Delta m \propto B$ as according to equation 3.10 the sensor heat capacity increases with $C_{\text{z}} \propto B^2$. For a given temperature $k_{\text{B}}T > \tilde{g}\mu_{\text{B}}B$ the maximum of the signal height can be found for $C_{\text{z}}(B) = C_{\text{e}} + C_{\text{ph}}$. For larger fields C_{z} increases until $C_{\text{z}}(B,T) \gg C_{\text{e}}(T) + C_{\text{ph}}(T)$ and we obtain $\Delta m \propto 1/B$. In this limit almost the complete energy that is put into the detector is absorbed by the spin system and is used to flip the magnetic moments of the sensor leading to a certain change of magnetization. Therefore, for large magnetic fields the signal height is almost independent of temperature as can be seen also on the right-hand side of figure 3.6 and thus it is less affected by variations of the detector's operating temperature. Though the absolute signal height in this case is comparably small, the achievable energy resolution might still benefit if the detector temperature fluctuates strongly for example due to instabilities in the temperature of the cryostat.

3.3.5 Influence of nuclear quadrupole moments

Nuclear quadrupole moment of ^{167}Er   In addition to the interaction between the magnetic moments discussed in the previous section the detector properties are also affected by the nuclear spin of the erbium ions. Among the naturaly occuring erbium isotopes only ^{167}Er with a natural abundance of 22.9 % and a nuclear spin of 7/2 features a non-zero nuclear spin. In [Fle03, Fle00] the effects of this isotope on the thermodynamic properties of the temperature sensor are discussed in detail and it is shown that the isotope ^{167}Er exhibits an additional heat capacity between 30 mK and 100 mK. As the energy put into this system does not result in a flipping of magnetic moments, no associated change of magnetization, as it would be suggested by equation 3.15, is observed and therefore the signal size is reduced. Therefore, all measurements shown in this thesis were carried out on samples prepared with material that was enriched in ^{168}Er which does not feature a nuclear spin. According to the supplier[6] the remaining fraction of ^{167}Er is only 1.2 %.

Nuclear quadrupole moment of gold   The only naturaly abundant isotope of gold is ^{197}Au with a nuclear spin of 3/2. It also exhibits a large nuclear electric quadrupole moment of 0.55 b [Pow74]. In an ideal gold single crystal the resulting energy levels are degenerate due to the cubic symmetry of the electric field tensors in the fcc lattice. In the presence of an Er^{3+} ion however this symmetry is broken by the modified charge distribution near the erbium ion and by small lattice deformations due to the different size of the erbium and gold ions. The resulting splitting of the energy levels leads to an additional contribution to the specific heat in the temperature range of interest [Her00] that increases with decreasing temperature and is almost independent of small external magnetic fields. In metallic magnetic calorimeters this effect can be observed as an additional fast signal decay when the energy redistributes from the magnetic moments of the Er^{3+} ions into the system of nuclear quadrupole moments with a time constant in the range between 0.2 ms and 1 ms, depending on the applied magnetic field [Fle98, Ens00].

3.3.6 Alternative sensor material $\underline{Ag}$:Er

As discussed in the previous section the use of gold as a host material for the paramagnetic Er^{3+} ions has the disadvantage of an additional heat capacity due to the quadrupole moments of the gold nuclei. With a nuclear spin of $I = 1/2$ both naturally abundant silver isotopes ^{107}Ag and ^{109}Ag lack a nuclear quadrupole moment, thereby making silver an interesting candidate for an alternative host material.

---

[6]*Oak Ridge National Laboratory*, Oak Ridge, TE 37831, USA

However, despite its possible benefits, the use of silver as a host material has the disadvantage that it supports a stronger RKKY interaction between the Er^{3+} ions. This effect is expressed by a larger interaction parameter α that is expected to be in the range of $\alpha = 6.4$ to $\alpha = 13.7$ [Bur08]. A value of $\alpha = 15$ was used to describe the experimental data in [Bur08], where the use of silver as host material in a bulk $\underline{Ag}$:Er sensor was investigated. As the *maXs30* detectors that were developed and fabricated in the framework of this thesis make use of microfabricated $\underline{Ag}$:Er sensors, a numerical description of $\underline{Ag}$:Er is needed. In [Dan05] it was shown that the thermodynamical properties of such a temperature sensor can be derived by appropriate scaling laws for the small concentrations of a few hundred ppm that are of interest for magnetic calorimeters. Based on the numeric simulations of the material $\underline{Au}$:Er, that were discussed in section 3.3.3 and which had been performed with an interaction parameter of $\alpha' = 5$, a scaling for the specific heat

$$c_{Er}(B, T, x, \alpha) = \frac{\alpha'}{\alpha} \times c_{Er}\left(B, T, \frac{\alpha}{\alpha'}x, \alpha'\right) \tag{3.20}$$

as well as for the magnetization

$$M(B, T, x, \alpha) = \frac{\alpha'}{\alpha} \times M\left(B, T, \frac{\alpha}{\alpha'}x, \alpha'\right) \tag{3.21}$$

was performed to allow for a different parameter α for $\underline{Ag}$:Er. Here, x denotes the concentration of Er^{3+} ions. Figure 3.7 shows both properties in dependence of the temperature T for different parameters α for a sensor with an Er^{3+} concentration of $x = 320$ ppm in a magnetic field of $B = 5$ mT.
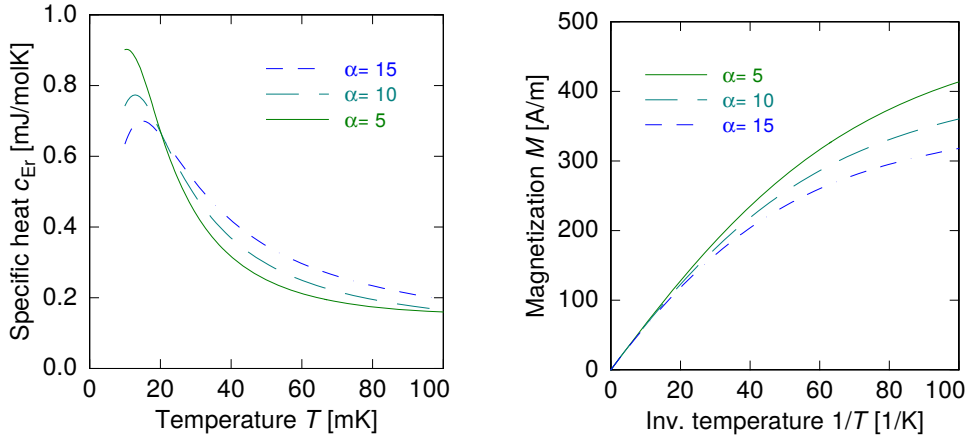

Figure 3.7: Heat capacity **(left)** and magnetization **(right)** of a $\underline{Ag}$:Er sensor with a concentration of 320 ppm that is situated in a magnetic field of 5 mT in dependence of the temperature T and the interaction parameter α.

With increasing interaction strength the maximum specific heat c_{Er} of the magnetic moments is reduced, however, for typical working temperatures of magnetic calorimeters above $20\,mK$ the specific heat increases. The stronger coupling between the magnetic moments also reduces the magnetization M and, therefore, its temperature dependence $\partial M/\partial T$. Accordingly, the increased interaction strength reduces the total signal height in two ways, but nevertheless silver remains an interesting candidate as a host material due to the absent nuclear quadrupole moments.

3.4   Sensor read-out and detector geometry

There are several possibilities of actually implementing the detection principle that is shown in section 3.1, especially regarding the read-out of the magnetization of the temperature sensor. Two of them are schematically shown in figure 3.8; together with further geometries they are discussed in detail in [Fle05]. A simple approach puts a cylindrical paramagnetic temperature sensor directly into the loop of a SQUID magnetometer as depicted on the left-hand side of figure 3.8.
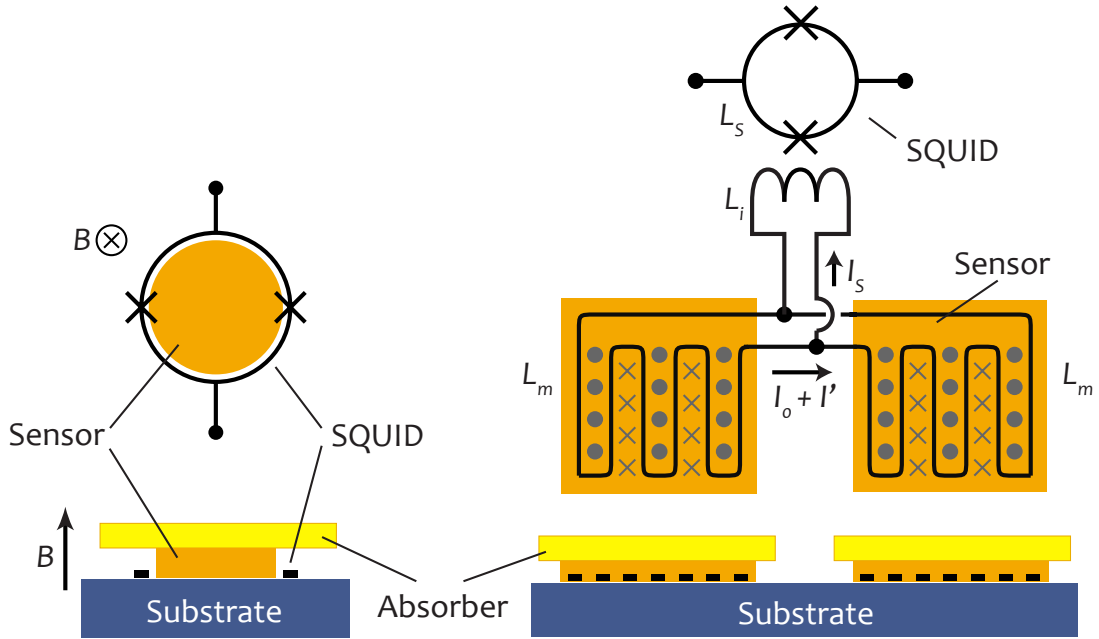
Figure 3.8: Schematic view of two read-out geometries after [Fle05]. **Left-hand side:** A cylindrical sensor placed directly into the loop of a SQUID magnetometer. The magnetic field needed to operate the detector is generated by a separate coil. **Right-hand side:** Gradiometric setup consisting of two planar sensors on top of two meander-shaped pick-up coils. The detector is coupled to a separate SQUID current sensor while the magnetic field is generated by a persistent current I_0 inside the superconducting loop.

The magnetic field that is needed to align the magnetic moments of the sensor has to be generated by an external coil. This setup has been shown to achieve energy resolutions down to 2.7 eV [Lin07]. However, such a setup has several drawbacks, especially when aiming towards large detector arrays. Many of these problems are solved by the setup shown on the right-hand side of figure 3.8 that has been used for the first time in [Bur04] and consists of two parallel planar meander-shaped pick-up coils that are connected in parallel to the input coil of a SQUID current sensor. The planar coils as well as the planar sensors on top can be produced very reliably and in large numbers using microfabrication techniques. Due to the very small distance between sensor and pick-up coil the coupling between the coil and the magnetic moments of the sensor can be improved compared to the cylindrical setup resulting in a larger signal size. The gradiometric setup with two pick-up coils in parallel reduces the influences of external magnetic fields as well as of variations of the chip temperature, as both coils contribute to the signal with different polarities. As shown in section 4.3 such a geometry allows the preparation of a persistent current in the superconducting loop that is used to create the magnetic field which is needed to align the magnetic moments of the paramagnetic sensor. Another disadvantage of the cylindrical setup is the distribution of the magnetic field that is generated by the magnetic moment of the sensor which, being a dipole field, exhibits a $1/r^3$-dependence. Therefore, the magnetic crosstalk between neighbouring detectors is relatively large, making a large spacial separation between individual detectors or additional structures for magnetic shielding necessary. In some applications, however, it may be favorable to keep the detectors closely packed. As we will see in the following section a detector array based on meander-shaped pick-up coils is less prone to crosstalk due to the higher-order multipole characteristic of the involved magnetic fields. The indirect coupling to the SQUID current sensors via a separate coil allows the fabrication of detector and SQUID on different substrates. In this way any influence of power dissipation due to the shunt resistors of the SQUIDs (ref. section 5.2.1) on the detector can be reduced. Due to the aforementioned advantages, the set-up with two gradiometric pick-up coils together with planar sensors is used for the detectors that are discussed in this thesis. In the following sections the magnetic field distribution within the sensor and the dependence of the detector signal on the sensor magnetization are discussed in further detail.

3.4.1 Generation of magnetic field

The highly inhomogeneous magnetic field that is created by a (persistent) current I_0 in the meander-shaped pick-up coil can be simulated using the methode of finite elements. Figure 3.9 shows the simulation results for a 250 nm thick superconducting pickup coil with a center-to-center distance of $p = 10\,\mu$m and a stripe width

of $w = 5\,\mu\mathrm{m}$ performed with the software femm[7]. The superconducting material is assumed as a perfect diamagnet. Also shown is the outline of a $3.2\,\mu\mathrm{m}$ high, planar paramagnetic sensor that is separated from the pick-up coil by a 250 nm thick insulation layer. Due to its small susceptibility the sensor material itself was not included into the simulation.
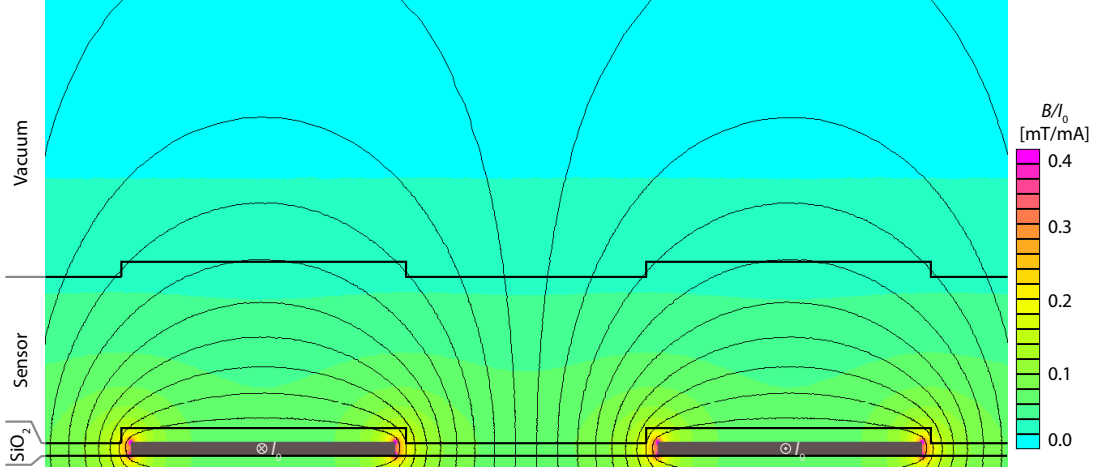

Figure 3.9: Cross-section through two lines of a meander-shaped pick-up coil (dark grey) and the magnetic field lines generated by a persistent current I_0 flowing in the pick-up coil. The resulting field strength is shown in pseudo-colours. The contour of a $3.2\,\mu\mathrm{m}$ thick sensor on top of a 250 nm thin insulation layer is also indicated.

The meander-like geometry leads to a strongly localized field whose strength decreases exponentially with increasing distance from the meander plane [Fle05]. One can define a position-dependent dimensionless geometric factor [Bur04]

$$G(\mathbf{r}/p) = \frac{p}{\mu_0} \frac{|\mathbf{B}(\mathbf{r})|}{I_0} \tag{3.22}$$

that connects the field-generating current I_0 with the magnetic field B at a position $\mathbf{r}$. Here $\mu_0 = 4\pi \times 10^{-7}\,\mathrm{Vs}/(\mathrm{Am})$ denotes the vacuum permeability. The length p can be any characteristic length scale and has been chosen to be the center-to-center distance of the meander stripes. To determine the change of magnetic flux that is created by a change of sensor magnetization as discussed in the following section it is not necessary to know the field configuration in 3-dimensional space. Instead it is sufficient to know the probability distribution of the geometric factors. Figure 3.10 shows this distribution for a $3.2\,\mu\mathrm{m}$ thick sensor, placed 250 nm above a meander-shaped pick-up coil with pitch $p = 10\,\mu\mathrm{m}$, stripe width $w = 5\,\mu\mathrm{m}$ and a thickness of 250 nm.

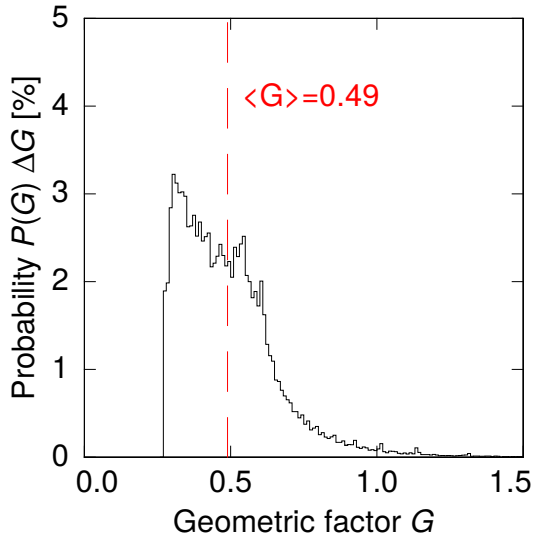[7]Finite Element Method Magnetics by David Meeker (http://www.femm.info)

Figure 3.10: Probability distribution of the geometric factor in a $3.2\,\mu m$ high volume separated by $250\,nm$ from a meander-shaped pick-up coil with pitch $p = 10\,\mu m$, stripe width $w = 5\,\mu m$ and a thickness of $250\,nm$. The corresponding volume is outlined in figure 3.9.

The average geometric factor for this case is $\langle G \rangle = 0.49$ which is only slightly smaller than the corresponding value for a cylindrical sensor inside a SQUID loop with a diameter much larger than the sensor diameter, where $\langle G \rangle = 0.5$ [Fle05]. For meander-shaped pick-up coils with smaller center-to-center distances and thinner sensors on top somewhat higher geometric factors are possible.

3.4.2 Signal read-out

In section 3.3 we have seen how a temperature change of the sensor influences its magnetization $\Delta M(\mathbf{r})$. For each volume element dV at the position $\mathbf{r}$ this change of magnetization couples into the superconducting pick-up loop and generates a magnetic flux change

$$d(\Delta \Phi) = \mu_0 \frac{G(\mathbf{r}/p)}{p} \Delta M(\mathbf{r})\, dV \tag{3.23}$$

inside the meander-shaped pick-up coil with center-to-center distance p. The geometric factor $G(\mathbf{r}/p)$ has already been defined in equation 3.22 and describes the position-dependent coupling strength between the magnetic moment of a volume element dV and the magnetic flux in the pick-up loop. It should be noted that not only the magnetic moments directly inside the superconducting loop contribute to the magnetic flux, but also the magnetic moments that are outside the loop. By integrating equation 3.23 and using equation 3.2 we get the total flux change inside the pick-up coil

$$\Delta\Phi = \int_V \mu_0 \frac{G(\mathbf{r}/p)}{p} \frac{\partial M(B(\mathbf{r}),T)}{\partial T} \Delta T(\mathbf{r}) \, \mathrm{d}V \tag{3.24}$$

$$= \Delta T \int_V \mu_0 \frac{G(\mathbf{r}/p)}{p} \frac{\partial M(B(\mathbf{r}),T)}{\partial T} \, \mathrm{d}V \tag{3.25}$$

following a temperature change $\Delta T(\mathbf{r}) = \Delta T = E/\left(C_\mathrm{e} + \int_V c_\mathrm{Er}(\mathbf{r}) \, \mathrm{d}V\right)$ of the sensor. Here C_e denotes the electronic specific heat of both, absorber and sensor and we assumed the sensor with the additional location-dependent specific heat $c_\mathrm{Er}(\mathbf{r})$ of the Er^{3+} ions to be in thermal equilibrium. The resulting integral can only be solved numerically and with a large amount of computation time due to the complicated spatial dependence of both $B(\mathbf{r})$ and $G(\mathbf{r}/p)$. However, the spatial distributions and position dependences of these parameters are not needed and it is sufficient to know the probability distribution $P(G)$ which also describes the distribution of the magnetic field strength. By introducing the weighted average

$$\langle A \rangle_G = \int P(G) A(G) \, \mathrm{d}G \tag{3.26}$$

of a parameter A, we get the expression

$$\frac{\Delta\Phi}{E} = \frac{V}{C_\mathrm{e} + V \langle c_\mathrm{z} \rangle_G} \left\langle \mu_0 \frac{G}{p} \frac{\partial M}{\partial T} \right\rangle_G \tag{3.27}$$

which can be calculated with reduced computing time and where V denotes the sensor volume.

3.4.3 Gradiometric design and coupling to SQUID current sensor

The detectors used in the framework of this thesis are based on the read-out scheme depicted on the right-hand side of figure 3.8: Two pick-up coils are connected in parallel to form a superconducting loop and are read out inductively by a SQUID that is coupled to the loop via an additional parallel inductance. As the flux in a superconducting loop is conserved, a change of flux $\Delta\Phi$ driven by a magnetization change of one of the two sensors evokes a supercurrent exactly negating the initial flux change. According to Kirchhoff's law and due to the flux conservation in the individual loops a part

$$\Delta I = \frac{\Delta\Phi}{L_\mathrm{m} + 2(L_\mathrm{i} + L_\mathrm{p})} \tag{3.28}$$

of this current also flows through the input coil of the SQUID and can therefore be measured. It depends on the inductances L_m, L_i and L_p of a single meander, the input coil of the SQUID and additional parasitic series inductances due to the wiring between detector and SQUID.

The pick-up coils of the two sensors generate opposing currents ΔI_1 and ΔI_2 for an equivalent flux change. For a perfectly gradiometric detector the resulting current in the input coil of the SQUID

$$\Delta I_\mathrm{s} = \Delta I_1 - \Delta I_2 \tag{3.29}$$
$$= \left(\Delta \Phi_1 - \Delta \Phi_2 \right) / \left(L_\mathrm{m} + 2(L_\mathrm{i} + L_\mathrm{p}) \right) \tag{3.30}$$
$$\propto \Delta T_1 - \Delta T_2 = T_1 - T_2 \tag{3.31}$$

is directly proportional to the temperature difference of the two sensors if we assume that both sensors share a common heat bath and are, therefore, initially at the same temperature. Here, $\Delta \Phi_1$ and $\Delta \Phi_2$ denote the flux changes in the two pick-up coils given by equation 3.27. Therefore, X-ray photons absorbed by these two detectors can be distinguished by the polarity of the resulting flux change $\Delta \Phi_\mathrm{s} = M_\mathrm{is} \Delta I_\mathrm{s}$ in the SQUID, while the amplitude of the signal is proportional to the temperature increase of the affected sensor. With the mutual inductance M_is between the SQUID loop and its input coil we finally get

$$\Delta \Phi_\mathrm{s} = \frac{M_\mathrm{is}}{L_\mathrm{m} + 2\left(L_\mathrm{i} + L_\mathrm{p} \right)} \left(\Delta \Phi_1 - \Delta \Phi_2 \right) \tag{3.32}$$

for the measurable flux in the SQUID in dependence of the flux changes in the two pick-up coils which are induced by a magnetization change of the two paramagnetic temperature sensors.

3.5   Signal shape and energy resolution

To calculate the energy resolution of the detector not only the signal height that was discussed in chapters 3.3 and 3.4 is important but also the actual shape of the signal that will be discussed in the following section. Furthermore the different noise contributions that will be introduced in section 3.5.2 have a large effect on the achievable energy resolution. In section 3.5.3 we will derive a fundamental limit for the energy resolution of microcalorimeters.

3.5.1   Detector signal

To derive the actual detector response to an energy deposition E of a detected particle, we can approximate the detector as a thermodynamic system consisting of two subsystems as depicted in figure 3.11 and as shown in [Fle05]. In this approximation we neglect any heat capacities arising from nuclear quadrupole moments of the host material.
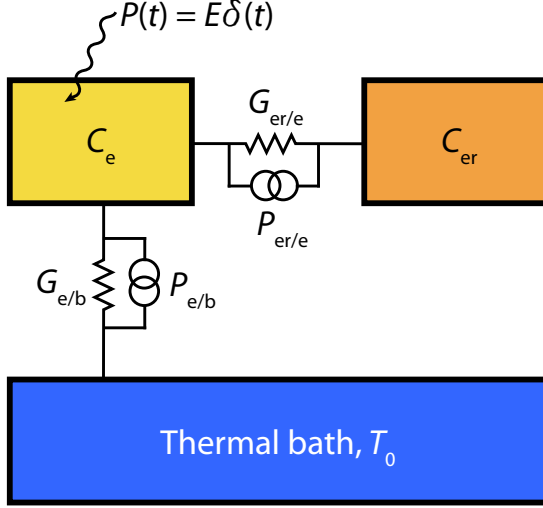

Figure 3.11: Thermodynamic model of a metallic magnetic calorimeter according to [Fle05]. Shown are the two subsystems of the electrons and the Er^{3+} spin system together with the associated heat capacities C_e and C_{er} and the thermal connections between the two systems as well as to the thermal bath. Further details are given in the text.

As the absorber and the temperature sensor are in close thermal contact we can safely assume that electrons and phonons are in thermal equilibrium across the whole detector and therefore we can treat them as a single thermodynamic system with heat capacity $C_e + C_{ph}$. However, at the given working temperatures, this system is dominated by the electrons and we can neglect the phononic heat capacity C_{ph}. The system couples to the system of the magnetic moments of the paramagnetic sensor which exhibits a heat capacity C_{er} as derived in chapter 3.3. The coupling between the two systems can be described by a thermal conductivity $G_{er/e}$. The system of the electrons and phonons also couples to a thermal bath at temperature T_0 via a weak thermal link $G_{e/b}$.

The resulting system is described by the coupled differential equations

$$\dot{E}_e = C_e\dot{T}_e = G_{er/e}\left(T_{er} - T_e\right) + G_{e/b}\left(T_0 - T_e\right) + E\delta(t) \qquad (3.33)$$

$$\dot{E}_{er} = C_{er}\dot{T}_{er} = G_{er/e}\left(T_e - T_{er}\right) \qquad (3.34)$$

for the energy contents E_e and E_{er} and temperatures T_e and T_{er} of the two subsystems following an instant energy input $E\delta(t)$ into the electronic system as described in

chapter 3.2.2. Solving for the temperature change

$$\Delta T_{\mathrm{er}} = T_{\mathrm{er}} - T_0 = \frac{E}{C_{\mathrm{e}} + C_{\mathrm{er}}} \left(-\mathrm{e}^{-t/\tau_0} + \mathrm{e}^{-t/\tau_1} \right) =: \frac{E}{C_{\mathrm{er}}} p(t) \tag{3.35}$$

of the spin system that can be read out as shown in chapter 3.4 yields the fundamental detector response for $t \geq 0$. Here, we also define the responsivity $p(t)$. The temperature of the spin system increases exponentially with the time constant τ_0 up to a maximum value, before the detector thermalizes again to bath temperature following an exponential decay with time constant τ_1. Both time constants obey a complicated dependence on the heat capacities and thermal conductivities involved in the system and are given in [Fle05]. If we assume a detector that is weakly coupled to the thermal bath ($G_{\mathrm{e/b}} \ll G_{\mathrm{er/e}}$) and where $C_{\mathrm{e}} \approx C_{\mathrm{er}}$, we obtain the simple expression

$$\tau_1 = \frac{C_{\mathrm{tot}}}{G_{\mathrm{e/b}}} \tag{3.36}$$

for the signal decay time with the total heat capacity $C_{\mathrm{tot}} = C_{\mathrm{er}} + C_{\mathrm{e}}$ of the detector. In section 3.5.3 we will see that the constraint $C_{\mathrm{e}} \approx C_{\mathrm{er}}$ maximizes the energy resolution of the detector. The rise time of the signal

$$\tau_0 = (1 - \beta)\tau_{\mathrm{K}} \tag{3.37}$$

however depends on the time constant $\tau_{\mathrm{K}} \propto T^{-1}$ which is associated with the Korringa relation of erbium in the host metal describing the interaction strength between the magnetic moments of the spin system and the conduction electrons. Here, $\beta := C_{\mathrm{er}}/(C_{\mathrm{er}} + C_{\mathrm{e}})$ denotes the fraction of the total heat capacity that is located in the spin system.

In the case of detectors with large volume absorbers it might be reasonable to introduce an artificial thermal bottleneck between the electronic systems of sensor and absorber as explained in section 3.2.2. In this case the interaction time between the spin system and the electrons of the sensor is much faster than the time constant associated with energy flow between absorber and sensor. Therefore, we can merge the heat capacities of the spin system and of the electrons of the sensor to a single subsystem of the detector. Together with the system of conduction electrons of the absorber we receive an analogous system to the one discussed before and the resulting signal shape does not differ from equation 3.35. Assuming $C_{\mathrm{s}} \approx C_{\mathrm{a}}$ for the heat capacities of sensor and absorber as well as a much weaker thermal link between sensor and heat bath compared to the one between absorber and sensor, we can derive the associated time constants. While the signal decay time is still given by equation

3.36, the rise time $\tau_0 = C_a/(2G_{a/s})$ is now given by the thermal link with thermal conductivity $G_{a/s}$ between the absorber and the paramagnetic sensor.

3.5.2 Noise contributions

In this section different intrinsic noise sources contributing to the total noise of metallic magnetic calorimeters are briefly discussed. Together with additional noise contributions from the SQUID current sensors, which are used for the detector read-out and considered in chapter 5.2.1, they limit the achievable energy resolution.

Thermal fluctuation noise

A very fundamental contribution to the noise of all microcalorimeters results from thermodynamic energy fluctuations between the different subsystems of the detector. The fluctuations can be described as a frequency-independent noise source with a spectral power density $S_P = 4k_B T^2 G$ which is proportional to the thermal conductivity G among the respective pair of connected subsystems. We can calculate the resulting noise density using the thermodynamic model of the detector depicted in figure 3.11 and discussed in the previous section. Omitting the energy input by an absorbed photon and introducing the two corresponding noise sources $P_{e/b}$ and $P_{er/e}$ in parallel to the thermal links, the resulting thermodynamic system is described by

$$\dot{E}_e = C_e \dot{T}_e = G_{er/e}(T_{er} - T_e) + G_{e/b}(T_0 - T_e) + P_{e/b} - P_{er/e} \tag{3.38}$$

$$\dot{E}_{er} = C_{er}\dot{T}_{er} = G_{er/e}(T_e - T_{er}) + P_{er/e} \ . \tag{3.39}$$

Assuming $C_e \approx C_{er}$ and $\tau_0 \ll \tau_1$ and solving for the energy fluctuations in the spin system we get after Fourier transform the spectral power density

$$S_{E_{er},td}(f) = k_B C_{er} T^2 \left((1-\beta)\frac{4\tau_0}{1+(2\pi\tau_0 f)^2} + \beta\frac{4\tau_1}{1+(2\pi\tau_1 f)^2} \right) \tag{3.40}$$

as derived in [Fle05]. The spectral power density is depicted in figure 3.12 and consists of two plateaus with cut-off frequencies $(2\pi\tau_0)^{-1}$ and $(2\pi\tau_1)^{-1}$. Assuming a spin heat capacity $C_{er} = 10\,\text{pJ/K}$, a working temperature of $T = 20\,\text{mK}$, a rise and decay time of $\tau_0 = 1\,\mu\text{s}$ and $\tau_1 = 1\,\text{ms}$ as well as $\beta = 1/2$, the first plateau has a value of $S_{E_{er},td} = 4 \times 10^{-3}\,\text{eV}^2/\text{Hz}$. If we assume $\partial\Phi/\partial E = 10^{-3}\,\Phi_0/\text{eV}$, this converts to a flux noise $S_{\Phi,td} = (\partial\Phi/(\beta\partial E))^2\,S_{E_{er},td} \approx 2 \times 10^4\,(\mu\Phi_0)^2/\text{Hz}$ in the pick-up coil. The actual flux change for a 10 keV photon in such a detector would be $10\,\Phi_0$.
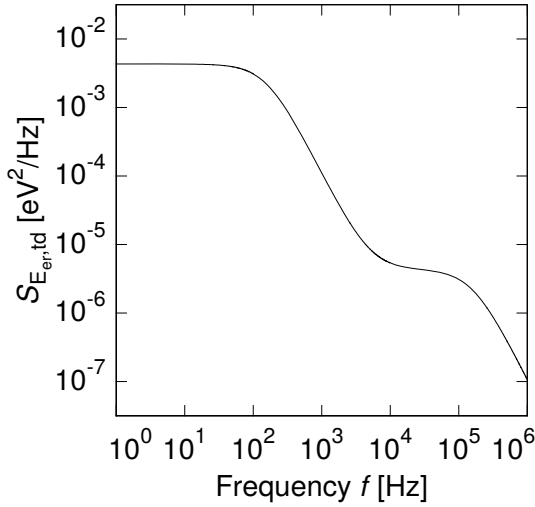
Figure 3.12: Spectral power density of the thermodynamic energy fluctuations for a detector with spin heat capacity $C_{\mathrm{er}} = 10 \, \mathrm{pJ/K}$, a rise time of $\tau_0 = 1 \, \mu\mathrm{s}$ and a decay time of $\tau_1 = 1 \, \mathrm{ms}$ as well as $\beta = 1/2$ at a working temperature of $T = 20 \, \mathrm{mK}$.

Magnetic Johnson noise

All non-superconducting metallic components in close vicinity of the superconducting pick-up coil or the SQUID contribute to the total noise by random electron movements that arise from the finite detector temperature. The potentially most dominant sources are the sensor and absorber of the detector itself as well as the sample holder commonly made of brass or copper to obtain a good thermal conductivity. According to Maxwell's equations the Brownian motion of the electrons leads to a changing magnetic field which couples to the pick-up coil or directly to the SQUID. In [Pie08, Pie12] the spectral power density

$$S_{\Phi,\mathrm{J}}\left(f\right) = \frac{2.376}{4\pi}\mu_0^2 k_{\mathrm{B}} T \sigma A p \left(\mathrm{e}^{-2\pi d/p} - \mathrm{e}^{-2\pi(d+h)/p}\right) \tag{3.41}$$

for the magnetic flux noise of a metallic cuboid at temperature T with electrical conductivity σ and height h was derived based on a method described in [Har68, Ens00]. The cuboid is located in distance d to a meander-shaped pick-up coil with center-to-center stripe distance p and an effective overlap area A. For a $5 \, \mu\mathrm{m}$ thick gold sample with a residual resistivity ratio of $RRR = 2.2$ and, therefore, a conductivity of $54 \times 10^6 \, \mathrm{A/(Vm)}$ at a temperature of $20 \, \mathrm{mK}$ which is located in a distance of $300 \, \mathrm{nm}$ from a $300 \, \mu\mathrm{m} \times 300 \, \mu\mathrm{m}$ large detection coil with $p = 10 \, \mu\mathrm{m}$ pitch, we get a noise density of $S_{\Phi,\mathrm{J}}\left(f\right) \approx 0.7 \, (\mu\Phi_0)^2/\mathrm{Hz}$. In first order this noise contribution is frequency-independent. For high frequencies, however, only a fraction of the metallic volume contributes to the noise due to the skin effect and a cut-off can be observed. For the parameters given above the skin depth $\delta = \sqrt{2/(2\pi f \mu_0 \sigma)}$ is smaller than the height of the noise-producing volume only for frequencies f above $100 \, \mathrm{MHz}$ which is much higher than the frequency range of interest and this effect can be neglected.

Paramagnetic loss noise

An additional noise contribution that is very important in the low frequency regime has been described in [Dan05] and could be traced back to the Er^{3+} ions in the sensor material. It obeys a frequency dependence of $S_{\Phi,\mathrm{Er}} \propto f^{-\zeta}$ where the exponent $\zeta = 0.8 \dots 1$ slightly depends on the geometry and preparation technique of the sensor. This spectral noise power density surprisingly does not depend on temperature between $30\,\mathrm{mK}$ and $2\,\mathrm{K}$ and is proportional to the number of erbium ions in the sensor [Fle03]. A possible source could be fluctuations of the magnetic moments that have been shown to generate a $1/f$-noise in spin glasses [Kog81]. However, the typical operating temperatures of metallic magnetic calorimeters are still more than one order of magnitude above the spin glass transition of $\underline{\mathrm{Au}}$:Er. Moreover, in contrast to the temperature-independent contribution in erbium sensors, the power density for spin glasses drops rapidly with increasing temperatures. Measurements of the suszeptibility of $\underline{\mathrm{Au}}$:Er sensors have shown that these noise contributions can be described by the imaginary part of the suszeptibility [Hof12, Wiß13], showing that the noise is related to and resulting from the finite and broadly distributed response time of the orientation of interacting clusters of magnetic moments.

Empirically, the resulting noise of a sensor made of gold containing N_{Er} erbium ions that is read out by a meander-shaped pick-up coil with center-to-center stripe distance p and geometric factor G as described in chapter 3.4 can be described with a power density

$$S_{\Phi,\mathrm{Er}} = \frac{\mu_0^2 \langle G^2 \rangle}{p^2} S_{\mathrm{m}}(f) N_{\mathrm{Er}} \tag{3.42}$$

with $S_{\mathrm{m}}(f) \approx 0.12\,\mu_{\mathrm{B}}{}^2 \times (f/\mathrm{Hz})^{-\zeta}$ describing the fluctuations of the magnetic moment of a single erbium ion. For a detector with $\langle G^2 \rangle = 0.25$, $p = 10\,\mu\mathrm{m}$ and $N_{\mathrm{Er}} = 5 \times 10^{12}$ we get a noise contribution of $S_{\Phi,\mathrm{Er}}(1\,\mathrm{Hz}) \approx 5 \times 10^4\,(\mu\Phi_0)^2/\mathrm{Hz}$. Accordingly, this noise contribution is typically higher than the Johnson noise up to frequencies in the $100\,\mathrm{kHz}$ range and it is in the same order of magnitude as the thermodynamic energy fluctuations at low frequencies.

3.5.3 Fundamental limit of the energy resolution

Based on the signal shape that was discussed in section 3.5.1 and on the thermodynamic energy fluctuations derived in section 3.5.2 one can calculate the expected energy resolution of a magnetic calorimeter. By neglecting all noise sources besides the fluctuations , i.e. neglecting noise sources described in the previous section as well as the read-out noise, the result will be a fundamental limit on the energy

resolution. The achieveable resolution depends on the actual method that is used to estimate the energy from a recorded signal. In [Fle03] the method of optimal filtering is thoroughly described and applied to magnetic calorimeters. For the Gaussian line broadening of the detector one derives

$$\Delta E_{\text{FWHM}} = 2\sqrt{2\ln 2}\left(\int\limits_0^\infty SNR^2(f)\,\mathrm{d}f\right)^{-1/2} \tag{3.43}$$

for the full-width at half-maximum of the detector line broadening, where

$$SNR^2(f) = \frac{|\tilde{p}(f)|^2}{S_{\text{E}_{\text{er}},\text{td}}(f)} \tag{3.44}$$

denotes the squared signal-to-noise ratio of the detector responsivity $\tilde{p}(f)$ that was defined in 3.35 in the frequency domain and the noise density $S_{\text{E}_{\text{er}},\text{td}}(f)$ of the thermodynamic noise. Given the thermal model shown in figure 3.11 this yields the exact solution for the energy resolution

$$\Delta E_{\text{FWHM}} = 2\sqrt{2\ln 2}\sqrt{4k_{\text{B}}T^2C_{\text{e}}}\left(\frac{G_{\text{e/b}}}{G_{\text{er/e}}} + \frac{G_{\text{e/b}}^2}{G_{\text{er/e}}^2}\right)^{1/4} \tag{3.45}$$

as shown in [Fle03], which approximates to

$$\Delta E_{\text{FWHM}} \approx 2\sqrt{2\ln 2}\sqrt{4k_{\text{B}}T^2C_{\text{e}}}\left(\frac{1}{\beta(1-\beta)}\frac{\tau_0}{\tau_1}\right)^{1/4} \tag{3.46}$$

for $\beta = C_{\text{er}}/(C_{\text{er}} + C_{\text{e}}) \approx 1/2$ and $\tau_0 \ll \tau_1$. As equation 3.46 shows, the energy resolution is best for $\beta = 1/2$ and thus matching heat capacities of absorber and sensor. To improve the energy resolution of a magnetic calorimeter one can moreover decrease the heat capacity C_{e} and operate the detector at low temperatures. A better energy resolution could also be achieved by a faster signal rise time or a slower decay time. However, the former is limited by the Korringa relation as explained in section 3.5.1 and can, therefore, not be increased arbitrarily, while increasing the decay time would also increase the dead time of the detector and limit its capabilities for high-rate applications.

The right-hand side of figure 3.13 depicts the signal-to-noise ratio for a micro-calorimeter with an absorber heat capacity of $C_{\text{e}} = 10\,\text{pJ/K}$, $\beta = 1/2$, a rise time of $1\,\mu\text{s}$ and a decay time of $1\,\text{ms}$ which is operated at $20\,\text{mK}$. The associated responsivity is shown on the left-hand side and the corresponding thermodynamic noise
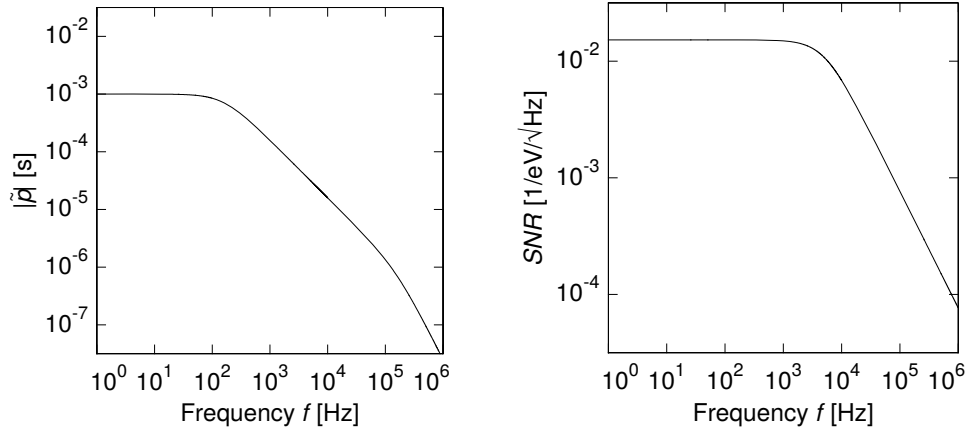
Figure 3.13: Responsivity $|\tilde{p}(f)|$ **(left)** and signal-to-noise ratio SNR **(right)** for a detector with spin heat capacity $C_{er} = 10\,\mathrm{pJ/K}$, a rise and decay time of $\tau_0 = 1\,\mathrm{\mu s}$ and $\tau_1 = 1\,\mathrm{ms}$ as well as $\beta = 1/2$ at a working temperature of $T = 20\,\mathrm{mK}$.

density is depicted in figure 3.12. According to equation 3.46 such a detector is fundamentally limited to an energy resolution of around $2\,\mathrm{eV}$.

4. Two-dimensional detector array *maXs30*

In the framework of this thesis a new two-dimensional detector array based on metallic magnetic calorimeters was designed, optimized, fabricated and characterized. While the results of the characterization measurements will be discussed in chapter 6.1, the design considerations, optimization and fabrication are discussed on the following pages. On the one hand this new detector should bridge the gap of energy ranges between the existing one-dimensional detector arrays based on metallic magnetic calorimeters *maXs20* [Sch12, Heu11] and *maXs200* [Pie12] that are optimized for the detection of X-rays with energies up to 20 keV and 200 keV, respectively. On the other hand it should open a door towards new two-dimensional arrays and to larger pixel counts.

The detector is optimized for X-ray energies up to 30 keV and aims especially for an increased detection area while at the same time keeping the good energy resolution of metallic magnetic calorimeters. It can be conveniently equipped with 10 μm to 50 μm thick absorbers depending on the application. In a configuration with a 30 μm thick absorber made of gold it has an absorption efficiency above 80 % for X-rays with energies up to 30 keV. Apart from spectroscopy of highly charged ions this detector can also be applied for example for the investigation of the 29.2 keV-doublet of the isotope ^{229}Th [Kaz14, Sch16, Pon17]. With a stopping power above 40 % for X-rays with energies up to 45 keV (ref. figure 3.2) it is perfectly suited for the high resolution spectroscopy of Ly$_\alpha$-transitions of hydrogen-like ions with a nuclear charge up to $Z = 65$. The very interesting Ly$_\alpha$-transition of hydrogen-like U^{91+} with an energy of around 100 keV is also still absorbed with an absorption efficiency of 25 %. The large energy bandwidth of the detector allows simultaneous measurements of Balmer-transitions occurring at lower energies and therefore allows for in-situ Doppler correction in beam-time experiments. At the same time the high energy resolution allows a precise measurement of transition energies.

4.1 Detector optimization

As discussed in chapter 3 the key properties of a metallic magnetic calorimeter are well understood and therefore its expected energy resolution can be calculated. Based on the principles discussed in chapter 3.5 a complete numerical optimization of a single *maXs30* detector was performed for a given working temperature of $T = 20$ mK. The data entering in the simulations are summarized in table 4.1 apart from the spe-

cific heat and the temperature dependence of the magnetization of the temperature
sensor that were determined numerically, and in good agreement with experimental
values, as discussed in chapter 3.3.3.

Miscellaneous		Meander-shaped pick-up coil	
Working temperature	20 mK	Pitch	10 µm
Signal rise time	3 µs	Line width	5 µm
Signal decay time	3 ms	Thickness	250 nm

Temperature sensor	
Relative strength of RKKY interaction α	12.5
RRR of sputtered $\underline{\text{Ag}}$:Er	2.4
$1/f$ noise per erbium ion $\sqrt{S_\Phi^{\text{Er}}}(1\,\text{Hz})$	$0.117\,\mu\Phi_0/\sqrt{\text{Hz}}$
Exponent ζ of $1/f$ noise $S_\Phi^{\text{Er}} \propto f^{-\zeta}$ of erbium ions	0.9
Thickness of insulation between pick-up coil and sensor	250 nm

SQUID current sensor		Absorber (made of Au)	
Input inductance	1.7 nH	Active area	500 µm × 500 µm
Input sensitivity	12.5 µA/Φ_0	Thickness	30 µm or 20 µm
White noise $\sqrt{S_\Phi^{\text{w}}}$	$0.2\,\mu\Phi_0\,/\sqrt{\text{Hz}}$	Specific heat	1.46×10^{-5} J/Kmol
$1/f$ noise $\sqrt{S_\Phi^{1/\text{f}}}(1\,\text{Hz})$	$5\,\mu\Phi_0/\sqrt{\text{Hz}}$	RRR	7-30
Exponent of $1/f$ noise	0.9		
Parasitic inductance	0.5 nH		

Table 4.1: Parameters entering the optimization of the *maXs30* detector array.

While the working temperature is limited by the cryostat that is used to operate the
detector, the absorber dimensions are given by the application as discussed at the
beginning of this chapter. The signal decay time was chosen such that a signal rate
of more than $10\,\text{s}^{-1}$ per absorber could easily be handled by the detector. Several
of the parameters are constrained by the microfabrication techniques that are used
to fabricate the detector array as discussed in section 4.4. These parameters include
the residual resistivity ratios RRR for sputtered $\underline{\text{Ag}}$:Er and electroplated gold that
are a measure for the number of defects and determine the thermal conductivity
of these materials at low temperatures. With a typical residual resistivity ratio
between $RRR = 7$ and $RRR = 30$ for the electroplated absorber made of gold
we get a thermal diffusion constant of $a = 0.1\,\text{mm}^2/\mu\text{s}$ to $0.5\,\text{mm}^2/\mu\text{s}$. Assuming a
maximum characteristic length scale of $l_{\text{diff}} = \sqrt{(l/2)^2 + (l/2)^2 + h^2} = 0.36\,\text{mm}$ for
photon absorption in the corner of an absorber with length $l = 500\,\mu\text{m}$ and height
$h = 30\,\mu\text{m}$, we get a characteristic time constant for thermal equilibration of the
planar absorber of the order of $l_{\text{diff}}^2/a = 1.3\,\mu\text{s}$ to $0.3\,\mu\text{s}$. As discussed in section 3.2.2

the rise time of $3\,\mu s$ was chosen such that no position dependence due to finite thermal diffusion is expected even in the case of the smallest assumed residual resistivity ratio. The thickness of the pick-up coil as well as the thickness of the insulation layer that galvanically separates the temperature sensor from the read-out are also determined by the microfabrication process. Principally smaller values for the center-to-center distance p and the width w of the pick-up coil are possible, however, $p = 10\,\mu m$ and $w = 5\,\mu m$ were chosen to increase the fabrication yield for the large detector arrays. For the SQUID current sensor typical parameters of state-of-the-art SQUIDs produced by our group were assumed. For the parasitic inductance between pick-up loop and SQUID current sensor a typical value of $L_p = 0.5\,nH$ was assumed.

Parameters that were varied during the simulation include the persistent current I_0 in the pick-up coil that generates the magnetic field inside the sensor, the height h and area A_s of the temperature sensor as well as its erbium concentration c. The meander-shaped pick-up coil is assumed to occupy the complete area of the sensor. For different sets of varied parameters the signal-to-noise ratio and the resulting energy resolution were calculated according to equations 3.44 and 3.46. Here, not only thermodynamic energy fluctuations but also all other noise sources as described in chapter 3.5.2 and 5.2.1 were included. The resulting optimum values of these parameters for a *maXs30* detector with $30\,\mu m$ thick absorbers are shown in table 4.2.

Temperature sensor		Meander-shaped pick-up coil	
Er^{3+} conc. c	$119\,ppm$	Inductance of single meander L_m	$3.81\,nH$
Thickness h	$4.07\,\mu m$	Coupling to SQUID $\partial\Phi_s/\partial\Phi$	$2.0\,\%$
Area A_s	$(371\,\mu m)^2$	Optimal field current I_0	$67.3\,mA$
Heat capacity C_{er}	$10.0\,pJ/K$		

$\rightarrow$ Energy resolution $\Delta E_{\mathrm{FWHM}} = 6.15\,eV$

Table 4.2: Resulting design parameters from a numerical optimization for a *maXs30* detector with an absorber thickness of $30\,\mu m$ and an absorber heat capacity of $10.7\,pJ/K$ at a temperature $T = 20\,mK$.

With the given constraints an energy resolution of $\Delta E_{\mathrm{FWHM}} = 6.15\,eV$ could be achieved for an optimal detector array. One finds that the heat capacity of the sensor is optimal for $C_{er} \approx C_e$, as suggested in section 3.5.3, leading to an equal distribution of the absorbed energy between the two subsystems of the detector.

However, in contrast to previous detectors that were fabricated in our group and that made use of a temperature sensor made of Au:Er (e.g. [Sch12, Heu11]), the concentration of the erbium ions in the sensor material Ag:Er could not be varied arbitrarily during fabrication with co-sputtering[1] techniques. Therefore, the erbium

---

[1]Simultaneous sputter deposition from two sputter targets, e.g. from a pure gold target and a

concentration was restricted to $c = 320\,\mathrm{ppm}$ by the available $\underline{\mathrm{Ag}}$:Er sputter target that was used to fabricate the sensors. Additionally an reduced sensor and meander area of $298\,\mu\mathrm{m} \times 298\,\mu\mathrm{m}$ was used to fabricate the *maXs30* detectors that were characterized in the framework of this thesis. Thereby enough space for the wiring, that is necessary for the detector operation, could be created underneath the absorbers. The overall increased spin heat capacity $C_{\mathrm{er}} > C_{\mathrm{e}}$ leads to a slightly less temperature-dependent signal height according to equation 3.19. With an absorber thickness of $30\,\mu\mathrm{m}$ and the aforementioned sensor properties an energy resolution of $6.95\,\mathrm{eV}$ would be expected. The very small deviation compared to the global optimum of the detector shows that small deviations of single parameters during the detector fabrication have only a small influence on the detector performance.

Additionally, for the *maXs30* detector arrays that were used in the framework of this thesis we aimed for absorbers with only $20\,\mu\mathrm{m}$ thickness as no experiments with X-ray energies above $60\,\mathrm{keV}$ were planned for these detectors. The corresponding design parameters of the fabricated detectors are shown in table 4.3. Due to the reduced absorber heat capacity the expected energy resolution improves to $6.14\,\mathrm{eV}$.

Temperature sensor		Meander-shaped pick-up coil	
Er^{3+} conc. c	$320\,\mathrm{ppm}$	Inductance of single meander L_{m}	$2.46\,\mathrm{nH}$
Thickness h	$3.5\,\mu\mathrm{m}$	Coupling to SQUID $\partial\Phi_{\mathrm{s}}/\partial\Phi$	$2.4\,\%$
Area A_{s}	$(298\,\mu\mathrm{m})^2$	Optimal field current I_0	$69.9\,\mathrm{mA}$
Heat capacity C_{er}	$17.8\,\mathrm{pJ/K}$		

$$\rightarrow \text{Energy resolution } \Delta E_{\mathrm{FWHM}} = 6.14\,\mathrm{eV}$$

Table 4.3: Design parameters of the actual *maXs30* detector arrays fabricated in the framework of this thesis with an absorber thickness of $20\,\mu\mathrm{m}$ and an absorber heat capacity of $7.16\,\mathrm{pJ/K}$ at a temperature $T = 20\,\mathrm{mK}$.

Figure 4.1 shows the different calculated contributions to the noise of the detector signal that enter the simulation of the fabricated *maXs30* detector discussed above. For better comparability the different contributions that are discussed in section 3.5.2 are recalibrated in terms of flux noise in the SQUID current sensor. The SQUIDs themselves contribute to the total noise with a frequency-independent white noise and a $1/f$-component that increases towards lower frequencies. Both contributions are discussed in section 5.2.1. For high frequencies, above about $1\,\mathrm{kHz}$, the white noise of the SQUID current sensors dominates while for frequencies below $5\,\mathrm{Hz}$ the SQUID noise and the $1/f$ noise of the erbium ions with the power density $S_{\Phi_{\mathrm{s}},\mathrm{Er}} = (\partial\Phi_{\mathrm{s}}/\partial\Phi)^2 S_{\Phi,\mathrm{Er}}$ are the most important contributions. The intermediate frequency range is dominated by the thermodynamic energy fluctuations $S_{\Phi_{\mathrm{s}},\mathrm{td}} = (\partial\Phi_{\mathrm{s}}/\partial\Phi)^2 (\partial\Phi/(\beta\partial E))^2 S_{\mathrm{E}_{\mathrm{er}},\mathrm{td}}$ between the different thermal subsystems of

highly doped $\underline{\mathrm{Au}}$:Er target.

the detector. The Johnson noise $S_{\Phi_s,J} = (\partial\Phi_s/\partial\Phi)^2 S_{\Phi,J}$ of the absorber and sensor is negligible in the complete frequency range.
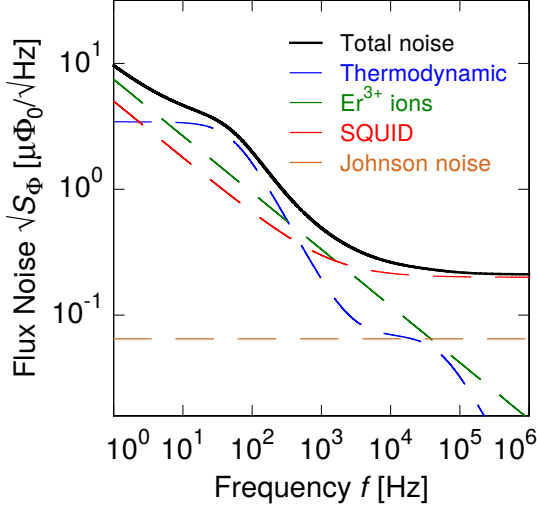

Figure 4.1: Calculated total magnetic flux noise in the SQUID and contributions of the individual noise sources for the *maXs30* detector with an absorber thickness of $20\,\mu m$ described in tables 4.1 and 4.3 at a working temperature of $T = 20\,mK$.

4.2   Design

The *maXs30* detector array consists of 64 absorbers that are connected to 64 paramagnetic temperature sensors[2] made of Ag:Er. Pairs of two sensors are read out by a superconducting niobium loop[3] implementing the gradiometric read-out scheme described in chapter 3.4.3. The array and all the necessary wiring are microfabricated in a cleanroom on a silicon substrate as will be discussed in detail in section 4.4.

The left-hand side of figure 4.2 shows a technical drawing of a complete *maXs30* chip including the detector array and all connection lines that was done with the software Virtuoso® [4] and that was used to fabricate the detector. A photographic image of the final chip is shown in the following chapter in figure 5.9. Each absorber (1), shown in transparent color, features an area of $500\,\mu m \times 500\,\mu m$ and is designed to have a thickness of about $30\,\mu m$. Depending on the exact application the thickness of the absorber may however be varied. Alltogether the 64 pixels provide a total detection area of $16\,mm^2$. With the gap between the absorbers being only $20\,\mu m$ wide, a filling factor of $93.3\,\%$ is achieved in the active region of the detector chip.

---

[2]In the following the combination of an absorber and the attached temperature sensor will also be referred to as 'pixel'.

[3]The combination of two pixels and their common pick-up loop will also be called a '(single/gradiometric) detector'.

[4]Cadence Design Systems, Inc., Bagshot Road, Bracknell, Berkshire, RG12 OPH, United Kingdom

Together with the high stopping power of each single absorber only few X-rays are therefore expected to hit the substrate where they might deposit heat leading to additional unwanted signals in the surrounding detectors. Underneath the absorbers the associated planar temperature sensors (2) are depicted in orange. In the corners of the chip four dedicated squares made of gold (3) can be seen on which flexible clamps may be positioned to mechanically press the chip to an experimental platform. The 32 detectors channels (i.e. micro-calorimeter pairs) are divided into four almost identical groups of eight detector channels that share common lines for preparing the persistent current in the way that is shown in section 4.3. The right-hand side of figure 4.2 depicts a detailed view of one such group.
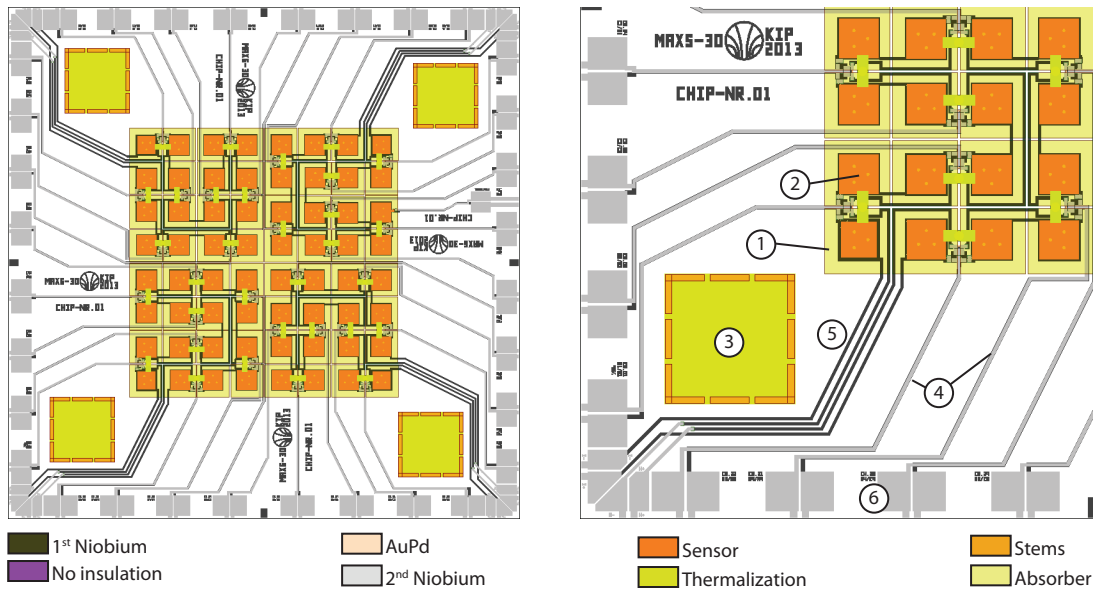

| 1st Niobium | AuPd |
| No insulation | 2nd Niobium |

| Sensor | Stems |
| Thermalization | Absorber |

Figure 4.2: Technical drawing of the complete *maXs30* detector chip with a close-up showing one quadrant of the chip: (1) absorber (shown in transparent color); (2) planar temperature sensor; (3) squares for easier handling and pressing of the chip; (4) read-out lines; (5) connecting lines to simultaneously prepare the persistent current in all eight single detectors of each quadrant; (6) pads to contact the individual lines via wire bonding.

The active area of the detector array is surrounded by the wiring which includes the lines for the read-out (4) of the detectors as well as for the preparation of the persistent current (5) that creates the magnetic field needed for the operation of the detectors. All the lines can be connected by wire bonding to the appropriate bonding pads (6) at the edge of the chip. The complete pick-up coil as well as all the connecting lines that are required to support large electric currents up to $100\,\text{mA}$ to prepare and carry the persistent current are marked in black in figure 4.2 and are routed in such a way that they can be fabricated in a single continuous layer without the need of a superconducting connection between two different layers. The meander-

shaped pick-up coils of the individual pixels are hidden underneath the planar sensors (2). The read-out lines (4) connecting the pick-up coil of each single detector to the bonding pads (6) that can be connected to the current-sensing SQUID, however, are realized as microstrips as they only have to carry currents in the $10\,\mu A$-range. By layering the go-and-return line of each detector read-out on top of each other the inductance of this line is greatly reduced, leading to less electromagnetic crosstalk between the different detector channels as well as a reduction of parasitic inductances in the read-out circuit. The inductance of a microstrip with length l, width w and an insulation thickness g between go-and-return line is given by $L_{\mathrm{ms}} = \mu_0 lg/w$. With typical parameters of the *maXs30* detector we therefore get $L_{\mathrm{ms}} < 50\,\mathrm{pH}$ which is small compared to the other involved inductances which are in the nH range.

Two out of the 32 micro-calorimeter pairs are prepared in a special way. One of them allows to drive a current through a small additional extension of the sensor, thereby creating a thermal pulse and providing a specific and controllable energy input. In absence of an appropriate external X-ray source with a large enough count rate in a single line, such pulses could be used to monitor drifts of the signal height that may arise due to temperature fluctuations during longer detector operations. The other special detector is not fully gradiometric as the size of one of the two sensors is reduced to 90 %.
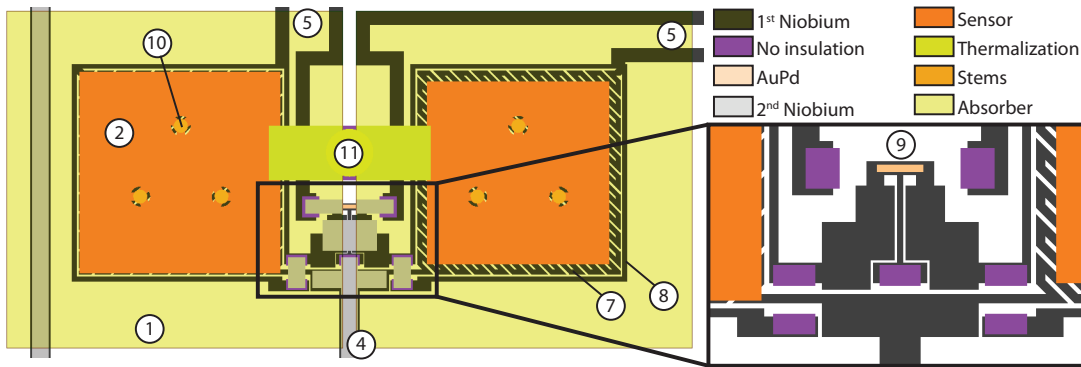

Figure 4.3: Technical drawing of a non-gradiometric single *maXs30* detector. On the right a close-up of the central region is shown. Depicted are: (1) absorber (shown in transparent color); (2) paramagnetic temperature sensor; (4) read-out lines; (5) connecting lines to prepare the persistent current; (7) superconducting pick-up coil; (8) superconducting loop enclosing each meander; (9) persistent current heater; (10) stems connecting absorber and sensor; (11) thermalization. For better visibility the absorbers as well as the second niobium layer have been suppressed in the close-up image.

Therefore, the detector is slightly sensitive to changes of the bath temperature and can thus be used to correct the signal height for such temperature changes as described in detail in [Sch16]. This is especially important as the design of all the

other detectors is highly gradiometric as will be shown in the following as well as in section 6.1.7. Figure 4.3 shows a detailed view of such a non-gradiometric detector. The superconducting pick-up coil (7) as well as the connections for supplying the persistent current (5) are depicted in black. Each of the two meander-shaped pick-up coils is enclosed by an additional superconducting loop (8) to shield against fluctuations of external magnetic fields and to decrease electromagnetic crosstalk between neighbouring detectors. Designing the meander-shaped coils in a diagonal way as shown in [Fle05] increases this effect as the currents flowing at the edge of the sensor cancel each other. The pick-up coil is drawn with a linewidth of $6.5\,\mu m$ to achieve the desired linewidth of $5\,\mu m$ after a potential overetching during the microfabrication of this layer. In between the two pixels the pick-up loop has a small extrusion. On top of this extrusion a small resistor (9) shown in light orange and made of the alloy AuPd with a ratio of approximately 1:1 is situated to prepare the field generating persistent current as described in section 4.3. The resistor is contacted by a second layer of niobium lines shown in light grey that is galvanically isolated from the first layer by a thin insulation layer made of silicon oxide. Where an electrical contact between first and second layer of wiring is needed this insulation layer has an opening depicted in purple. The extrusion is partly covered by a small superconducting niobium plane to minimize its inductance. As explained above the read-out lines (4) that are ultimately connected to the input coil of a SQUID current sensor are designed as microstrips. In contrast to earlier microcalorimeters that have been produced in our group (e.g. [Pie12, Sch12, Heu11]) both contact points of the microstrips to the pick-up loops are completely symmetric, leading to a significantly improved balancing of the two calorimeters of each channel as we will see in section 6.1.7. This highly gradiometric design again reduces crosstalk between different detectors and facilitates the preparation of the persistent current at temperatures below $1.2\,K$ as shown in section 4.3.

On top of each pick-up coil, separated by the insulation layer, the paramagnetic sensor (2) made of Ag:Er is located, depicted in dark orange. Each sensor is connected to the associated absorber (1) via three stems (10). With a diameter of $20\,\mu m$ the three stems only cover $0.38\,\%$ of the absorber area, thereby greatly reducing the probability of loosing athermal phonons as explained in section 3.2.2. Each stem in turn only has direct contact to a small part of the sensor which is connected to the main part of the sensor by three thermal links made of Ag:Er. This limits the signal rise time to ensure a complete thermalization of the large volume absorber as shown in chapter 3.2.2. The thermal connection (11) from the sensor to the heat bath is done by a layer of $300\,nm$ thick gold with well defined dimensions that should lead to a thermalization time of around $3\,ms$ at a temperature of $20\,mK$. Due to the two-dimensional and close-packed design of the array, in contrast to earlier designs (e.g. [Pie12, Sch12, Heu11]) the thermal bath itself can no longer be provided by a

large heat sink made of gold at an edge of the chip that is then connected to the experimental holder with bonding wires made of gold. However, the thermalization has to be done in the third dimension through the substrate of the silicon chip.

Pick-up coil		Microstrips for read-out	
Material	Nb	Material	Nb
Thickness	250 nm	Bottom line width	30 µm
Line width	5 µm	Top line width	24 µm
Pitch	10 µm	Thickness bottom line	250 nm
		Thickness top line	400 nm
		Thickness insulation	250 nm
Temperature sensor		X-ray absorber	
Material	A̲g:Er (320 ppm)	Material	Au
Area	298 µm × 298 µm	Area	$(500\,\mu\text{m})^2$
Thickness*	3.5 µm	Thickness*	30 µm
Number Er^{3+} ions*	5.9×10^{12}	Heat capacity*	$11\,\text{pJ}\,\text{K}^{-1}$
Persistent current heater		Stems	
Material	AuPd	Material	Au
Length	20 µm	Diameter	20 µm
Width	5 µm	Height	7 µm
Thickness	60 nm	Fraction of abs. area	0.38 %
Resistance	$8.8\,\Omega$		
Link to thermal bath		Link between absorber and sensor	
Material	Au	Material	A̲g:Er +Au
Signal decay time	3 ms	Signal rise time	3 µs

Table 4.4: Design parameters of the *maXs30* detector to be operated at $T = 20\,\text{mK}$. The parameters marked with a star (*) depend on the thickness of the absorber which may be adapted to experimental needs. In this case the thickness of the sensor can be changed accordingly during fabrication without changing the lateral design of the detector to keep an optimized energy resolution.

Therefore, it is planned to etch holes through the silicon to fill them afterwards with gold or copper in order to achieve a very good thermal contact to the backside of the chip which can then be thermally connected to the experimental holder. The first step to create these thermal links – the etching of the holes – was developed in the framework of this thesis and is explained in section 4.4. As the filling of the holes with gold was not yet available, the etching of the silicon was omitted for the detectors that are discussed in this thesis. Instead a large heat bath made of A̲g:Er

and a passivation layer made of gold has been sputter deposited on the backside of the chip. With the large heat capacity of the Er^{3+} ions this layer should act as a thermal reservoir that absorbs any heat that is created by the absorption of an X-ray in a detector in such a way that neighbouring detectors do not suffer from thermal crosstalk. In table 4.4 the most important design parameters of the relevant detector structures are summarized.

Next generation　While the detectors characterized and used in the framework of this thesis exhibit the design shown above, an improved design has already been drawn and fabricated in the cleanroom. The new generation exhibits not only one, but four non-gradiometric detectors, one in each corner of the detector array as well as four detectors with the ability to create thermal pulses. Thereby it should be possible to better correct for temperature gradients on the chip when correcting for temperature fluctuations. Additionally, the bonding pads for the SQUID read-out have been modified to match the novel symmetrized 3-bond-pad scheme of the new SQUID current sensors produced in our group and to further decrease the susceptibility to fluctuating external magnetic fields.

4.3　Preparation of the persistent current

The magnetic field that is needed to operate the paramagnetic sensor as discussed in section 3.3 is created by a persistent current I_0 circulating in the superconducting niobium loop underneath the sensors. Figure 4.4 schematically depicts the process of the preparation of this current. When the current I_0 is first supplied (step 1) it mainly flows through the boxes surrounding the individual pick-up coils[5] due to their much smaller inductance compared to the inductances of the meanders. By feeding a short current pulse I_H to the resistor on top of the persistent currrent switch, i.e. a the small extrusion of the pick-up loop, the switch is locally heated above the critical temperature of niobium of $9.2\,\text{K}$ (step 2). Therefore, the current I_0 flows through the only remaining superconducting connection and thereby through both meanders. Due to the thermal pulse also one of the two read-out lines is driven normalconducting as it contacts the pick-up coil in the center of the extrusion next to the resistor. Therefore, even at temperatures below $1.2\,\text{K}$ where the connecting bonding wires made of aluminium between detector and SQUID chip are superconducting the direct path through both meanders remains the only superconducting connection and preparing the persistent current at such temperatures should be more reliable. After the short heat pulse the chip cools down again and the niobium becomes again superconducting. Due to the flux conservation in superconducting loops the persistent

---

[5]In the following the meander-shaped coils will also be referred to as 'meander'.

current I_0 is flowing through the meanders even if the current source supplying the field generating current is now switched off. In the *maXs30* detector array the field current and heater lines of all eight detectors of each quadrant are connected in series and therefore in all these detectors the persistent current is prepared simultaneously.
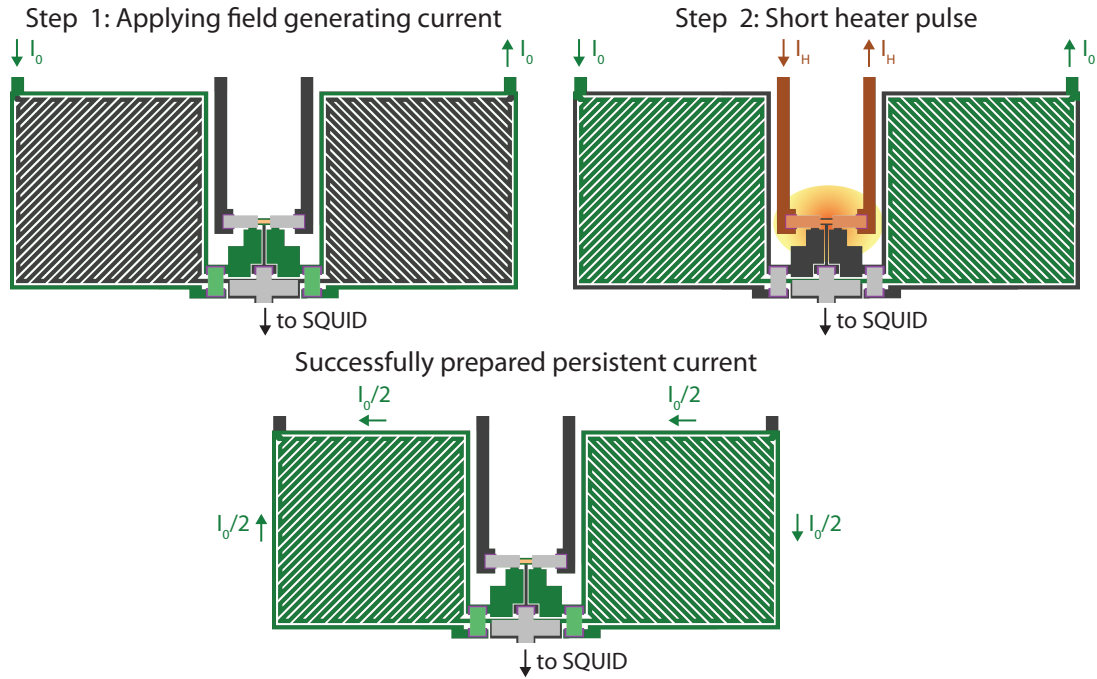

Figure 4.4: Preparation of the persistent current that is needed to operate the detectors. The different lines fabricated in the first and second niobium layer are colored in: (black/grey) 1st/2nd layer without current; (dark/light green) 1st/2nd layer with field current; (dark/light orange) 1st/2nd layer with heater current. A description of the individual steps is given in the text.

4.4 Microfabrication

The detector arrays used in the framework of this thesis were produced with microfabrication techniques that are explained in more detail in [Zao06, Pie08] in a multi-layer-process on a silicon substrate. The use of 2 inch and 3 inch silicon wafers[6] allows the simultaneous fabrication of up to 16 and 36 *maXs30* detector chips, respectively. The wafers are thermally oxidized with a 240 nm thick SiO_2 layer.

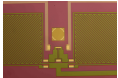[6]Si-Mat Germany Silicon Materials, Viktor-Frankl-Str. 20, 86916 Kaufering, Germany
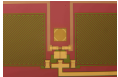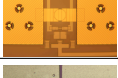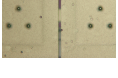
No		Layer	Material	Photo resist	Technique	RRR
1		Pickup-coil and first layer of wiring	250 nm Nb	5214E	Sputter dep. and dry/wet etching	≥ 5.1
2		First insulation	25 nm to 50 nm Nb_2O_5	5214E IR	Anodisation and Lift-off	n.a.
3		Second insulation	250 nm to 300 nm SiO_2	5214E IR	Sputter dep. and lift-off	n.a.
4		Persistent current switch heater	60 nm AuPd	5214E IR	Sputter dep. and lift-off	1.2
5		Second layer of wiring	400 nm Nb	5214E IR	Sputter dep. and lift-off	≥ 6.4
6		Third insulation	250 nm SiO_2	5214E IR	Sputter dep. and lift-off	n.a.
7		Thermal links to heat bath	300 nm Au	5214E IR	Sputter dep. and lift-off	2.1
8		Etch stop on front side	500 nm Au	5214E IR	Sputter dep. and lift-off	2.1
9		Temperature sensors	3.5 μm Ag:Er + 100 nm Au	nLOF 2070	Sputter dep. and lift-off	2.4
10		Heath bath on back side	2 μm Ag:Er + 500 nm Au	-	Sputter dep.	-
11		Stems	Au	6632	Two-layer process with absorbers	7-30
12		Absorbers	20 μm to 30 μm Au	125nXT	Electroplating and lift-off	7-30

Table 4.5: The different layers and their materials of the *maXs30* detector that was fabricated and characterized in the framework of this thesis. Also shown are the photoresist and the techniques that were used to process each layer as well as the residual resistivity ratio of each layer where applicable. The latter has was on test structures from the same wafer as the actual *maXs30* detectors apart from the electroplated gold. A larger version of the images can be found in appendix A. Photoresists marked with 'IR' are processed as image reversal resists.

All of the fabrication is done in-house, most of it in a cleanroom environment to minimize the number of defects on the chip due to micrometer-sized dust particles. Table 4.5 summarizes the 12 layers of the *maXs30* detector array. Microscopic photographs of each layer are shown in the table and can be found in a larger version in appendix A. The photoresists[7] that are used to transfer the design of the different detector layers to the actual wafer can either be exposed with UV light in a mask aligner[8] as described in [Pie12] or by a new maskless aligner[9] that allows contactless exposure as well as an automated alignment of the different layers of the detector array. Apart from the first insulation layer and the absorber layer including the stems, the deposition of the different materials is done by sputter deposition. The primary UHV sputtering system[10] that is situated in the cleanroom and reaches base pressures down to 2×10^{-9} mbar is equipped with the necessary targets to produce the layers made of Nb, AuPd, $\underline{Ag}$:Er and Au. Each layer except the first one is fabricated using a lift-off process, while the first niobium layer that contains most of the wiring and all structures that are required to carry supercurrents in the 10 mA to 100 mA-range is fabricated by sputter depositing a continuous niobium layer on the bare substrate followed by an etching process. The latter can either be done by wet etching with a solution of hydrofluoric acid (HF), nitric acid (HNO_3) and water in a ratio of 1:6:10 or by a dry etching process using SF_6 in the ICP-RIE[11] plasma etcher SI 500C[12] as described in [Möh15]. The first insulation layer is done by an anodizing process resulting in a 25 nm to 50 nm thick Nb_2O_5 layer. For that purpose the wafer is put in a solution of ethylene glycole ($C_2H_6O_2$), water and ammonium pentaborate ($NH_4B_5O_8$) in a ratio of 25:19:4 and a voltage of 25 V is applied between the first niobium layer and a second electrode in the solution. During this process all parts that have to provide an electrical contact to the second niobium layer or act as a surface for contacting the chip are protected by a layer of photoresist. The additional SiO_2 insulation layers can either be deposited by reactive rf-sputtering in the DCA system or in a sputtering system[13] outside the cleanroom that reaches a base pressure around 5×10^{-7} mbar. The paramagnetic sensor material $\underline{Ag}$:Er is covered in-situ with an additional thin layer made of gold to prevent oxidation and to thereby enable a better sticking of the stems to the sensor. The erbium concentration of the $\underline{Ag}$:Er sensor is determined in an independent measurement in a commercial SQUID

---

[7]AZ Electronic Materials; now part of Merck Performance Materials GmbH, Rheingaustrasse 190-196, 65203 Wiesbaden, Germany

[8]Süss MJB3; Süss MicroTec AG, Schleissheimer Straße 90, 85748 Garching, Germany

[9]HIMT MLA 150; Heidelberg Instruments Mikrotechnik GmbH, Tullastrasse 2, 69126 Heidelberg, Germany

[10]DCA Instruments Oy, Vajossuonkatu 8, 20360 Turku, Finland

[11]Inductively Coupled Plasma - Reactive Ion Etching

[12]SENTECH Instruments GmbH, Schwarzschildstraße 2, 12489 Berlin, Germany

[13]Alcatel SCM 601 from Alcatel Vacuum Technology France SAS; now part of Pfeiffer Vacuum SAS, Annecy, 98 avenue de Brogny, France

magnetometer system[14] on the excess material which is removed during the lift-off process of the sensor layer. The measurements are performed in a temperature range from 2 K to 300 K in a magnetic field of 1 T and are then fitted with simulated data based on the theory discussed in section 3.3.3. After the fabrication of the absorbers in a two-layer process that is discussed in the following section the wafers are cut with a dicing saw [15] into the individual detector chips.

Fabrication of the absorber on stems   The absorbers are fabricated together with the stems in a process that uses a two-layer photoresist mold and that is described for 5 µm thin absorbers in detail in [Sch12]. After the structuring of the stems as holes in a first layer of photoresist made of AZ6632[7] a seed layer made of 100 nm thick gold and a sacrificial layer of 50 nm thick niobium are deposited on top. For structuring the absorbers of the *maXs30* detector the photoresist AZ125nXT[7] that can be processed with a thickness of up to 100 µm and that was investigated in [Kra13b] is used. The wafer is spin coated with 2000 rpm for 15 s and thereafter baked for 50 min at 100 °C in an oven. Then the non-absorber areas are exposed by a UV laser with a dose of 25 nJ/µm² in the mask less aligner MLA 150. After removing the unexposed parts with the developer AZ826MIF[7] for 90 s a hardbake is performed for 10 min at 100 °C.
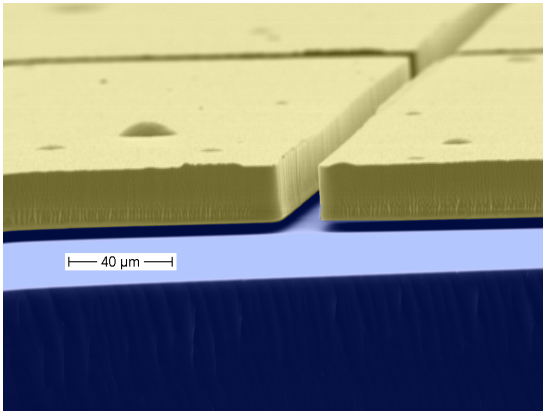

Figure 4.5: Colored SEM image of 25 µm thick absorbers (yellow) that have been fabricated on a silicon substrate (blue). The absorbers are standing on three stems each and have 20 µm wide gaps between each other.

Afterwards the surface is cleaned by ion milling in the load lock of the DCA sputtering system. In this step the sacrifical layer made of niobium acts as a protection layer and prevents the sputtering of gold atoms. Else the latter might thereafter be deposited on the side walls of the photoresist and would prevent an even growth of the gold layer during the following electroplating. To remove remaining niobium a dry etching step in the ICP-RIE etcher is performed. Afterwards the absorbers are electroplated

---

[14]QD MPMS® XL from Quantum Design Inc, 10307 Pacific Center Court, San Diego, CA 92121, USA

[15]DAD-2H/6 from Disco HI-TEC EUROPE GmbH, Liebigstrasse 8, 85551 Kirchheim b. München, Germany

together with the stems in the electroplating solution Techni Gold 25 ES[16] with a current density of $1\,\mathrm{mA/cm^2}$ at a temperature of $60\,°\mathrm{C}$. In this step the seed layer acts as the cathode on which the gold is deposited. Compared to sputter deposited gold, electroplated gold allows for a much higher residual resistivity ratio and thus a better thermal conductivity. Additionally electroplating minimizes the amount of deposited excess material. Finally, the photoresists are removed together with the residual seed layer between the absorbers. Figure 4.5 depicts a colored SEM picture of the resulting $25\,\mathrm{\mu m}$ high absorbers that have been fabricated for test purposes on a bare silicon substrate.

Etching of holes through the silicon substrate As discussed in section 4.2 it is planned for the thermalization of future detectors to establish a direct thermal contact from each micro-calorimeter pair on the front side of the detector chip to the wafer backside. The first step - the etching of the holes through the wafer has successfully been developed in the framework of this thesis. A hard mask made of $2\,\mathrm{\mu m}$ thick sputter deposited aluminium is used to define the areas that are to be etched. First the thermal SiO_2 layer coating the silicon substrate is removed in the inductively coupled plasma etching system SI 500C at a temperature of $15\,°\mathrm{C}$ and a pressure of $0.5\,\mathrm{Pa}$. As etching gas CHF_3 with a flow of $50\,\mathrm{sccm}$ is used as discussed in [Möh15].
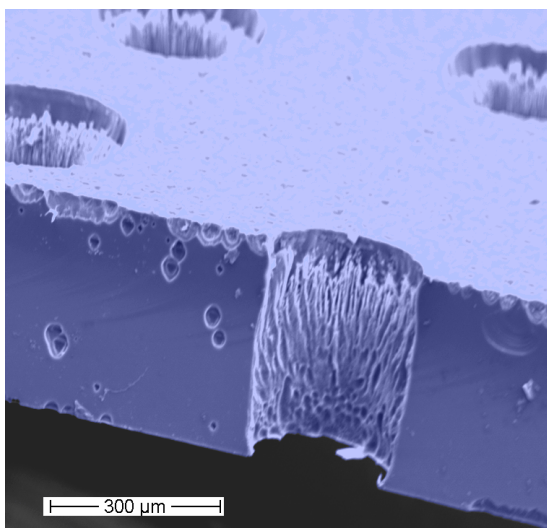
Figure 4.6: Colored SEM image of a cross-section trough a hole with a diameter of $200\,\mathrm{\mu m}$ etched through a $300\,\mathrm{\mu m}$ thick silicon wafer with ICP-RIE etching.

The subsequent anisotropic etching of the silicon substrate is also done with a dry etching process and is based on several parallel reaction mechanisms that are described in [Jan94]. A chemical isotropic etching is done by $F^\bullet$ radicals originating from SF_6 that enters the reactor with a flow of $125\,\mathrm{sccm}$. To passivate the side-walls of the developing holes a flow of $9\,\mathrm{sccm}$ O_2 is added to the process gas. The forming

[16]Technic Deutschland GmbH, Baukauer Straße 125, D-44653 Herne, Germany

passivation layer of SiO_xF_y is stable at the processing temperature of $-90\,°C$ and protects the silicon underneath from further etching. By adding a physical etching component the passivation layer at the bottom of the hole is removed and the $F^\bullet$ radicals are able to further etch the silicon. Figure 4.6 shows a colored SEM image of several holes with a diameter of $200\,\mu m$ demonstrating the steep side walls of the holes.

5. Experimental Methods

This chapter introduces the cryostat that was used to cool down the detector arrays to the operating temperatures in the millikelvin range as well as the read-out of the detector using SQUID current sensors and the actual setup of the different experiments. Finally an overview over the utilized radioactive calibration sources is given as well as a description of the internal gas target of the experimental storage ring at the GSI[1] where some of the measurements were performed.

5.1 Cryogenics

In this section the cryostat including the wiring and thermometry is described. Special attention is given to the side arm on which the detector arrays can be mounted and that allows to operate the detectors as close as possible to external X-ray sources.

5.1.1 Cryostat

The detectors were operated in a dry dilution refrigerator of type BF-LD250[2] that reaches a base temperature below $10\,\mathrm{mK}$. Figure 5.1 shows a sketch and a photograph of the principal components of the cryostat. The cooling technique based on the dilution of ^{3}He from a concentrated phase into a dilute ^{3}He/^{4}He phase is discussed in detail in [Pob92, Ens05]. In contrast to the other cooling technique that is commonly used to reach millikelvin temperatures and which is based on adiabatic demagnetization of paramagnetic salt pills, this technique provides a continuous cooling. This is especially beneficial as the used cryostat is dedicated for experiments at electron beam ion traps and storage rings, where an efficient usage of available beam time is desired. For the same reason the necessary pre-cooling to temperatures around $4\,\mathrm{K}$ is not done by liquid nitrogen and liquid helium which would require frequent access to the cryostat to refill the liquids. Instead pre-cooling is done by a two-stage pulse tube cooler[3] which supplies a temperature around $3.5\,\mathrm{K}$. To reduce vibrations from the pulse tube to the other parts of the cryostat, it is mechanically isolated and only connected via thick, flexible copper ribbons that provide the necessary thermal contact. The complete cryostat may be operated via remote control and provides a

---

[1]GSI Helmholtzzentrum für Schwerionenforschung GmbH, Planckstraße 1, 64291 Darmstadt, Germany

[2]BlueFors Cryogenics Oy, Arinatie 10, 00370 Helsinki, FINLAND

[3]PT410 from Cryomech, Inc., 113 Falso Drive, Syracuse, New York 13211, USA

fully automatic cooldown that facilitates the operation of the cryostat in different places, where continuous access can not be guaranteed, like at storage rings or in underground laboratories.
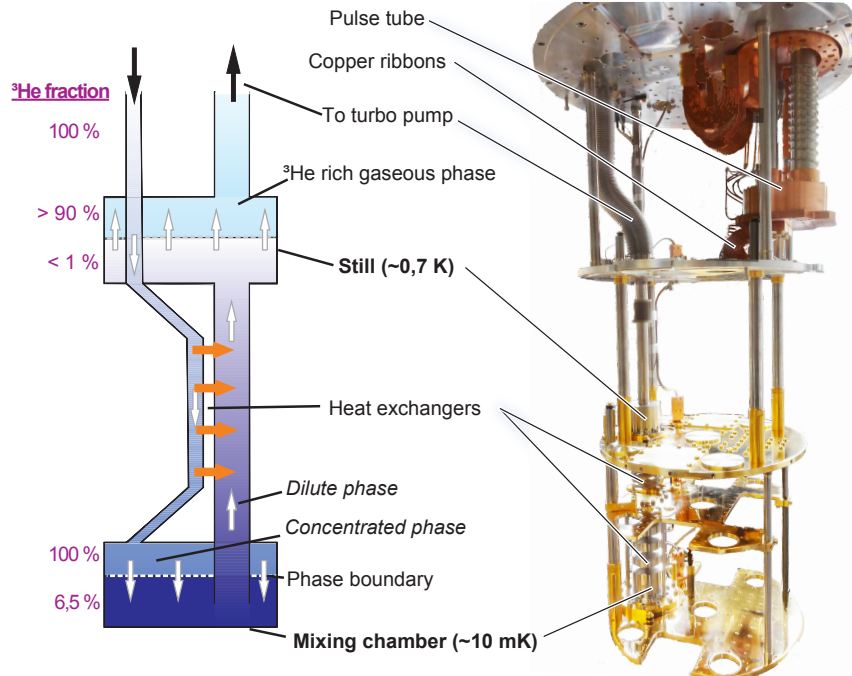

Figure 5.1: Schematic illustration [Pon17] and photograph of the principal components of the pulse tube cooled dilution refrigerator that was used for the experiments.

5.1.2   Side arm

The cryostat is equipped with a home made 40 cm long side arm on which the detector arrays as well as the SQUID current sensors used for the read-out of the detectors are placed. This helps to position the detector arrays as close as possible to any external X-ray source in order to maximize the achievable count rates where geometrical constraints hinder the mounting of the cryostat directly next to the source. Figure 5.2 depicts a photograph of the vacuum tube of this side arm mounted on the vacuum can of the cryostat as well as a technical drawing showing a cross section through the different parts of the arm. The actual cooling finger of the side arm is made of copper to ensure a good thermal conductivity and is split into two parts: one inner arm (7) and a surrounding square tube (6). The inner arm is directly attached to the mixing chamber platform of the cryostat and provides a good thermal contact to the experimental platform (8) that is screwed directly onto this arm and can in this configuration be cooled down to temperatures between 15 mK and 20 mK.
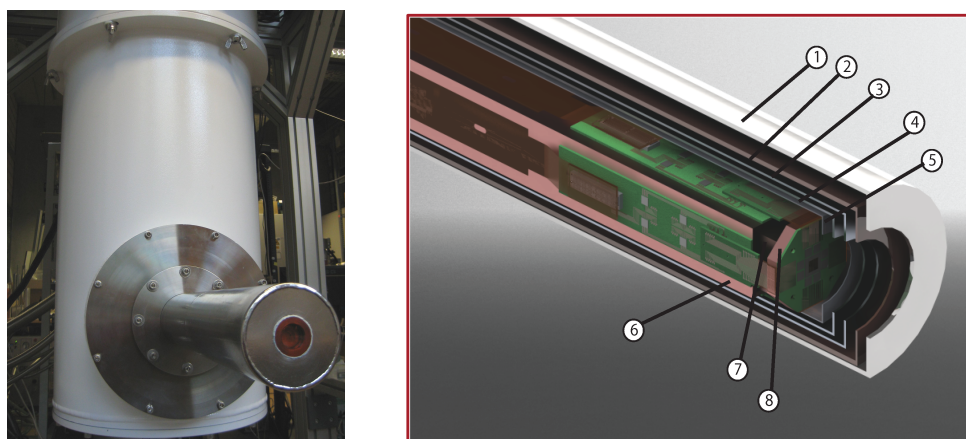
Figure 5.2: Left-hand side: Photograph of the side arm equipped with an X-ray window made of polyimide. **Right-hand side:** Technical drawing of the side arm with (1) vacuum tube made of a soft magnetic alloy; (2-4) radiation shields made of copper and aluminium, respectively; (5) niobium tube for additional magnetic shielding; (6) outer and (7) inner copper arm; (8) experimental platform for the detector array. Further details are given in the text.

The outer square tube on the other hand supports the circuit boards with the low-temperature amplifiers for the read-out that will be introduced in section 5.2.1. It is thermally isolated from the inner arm to minimize heating effects on the experimental platform due to the amplifiers. To cool down the outer arm itself it is attached to the mixing chamber platform with copper braids. Both arms were annealed at 850 °C for 48 h in order to increase their thermal conductivity.

The complete copper arm is surrounded by three thermal radiation shields (2-4) that are thermally connected to the different temperature stages of the cryostat and are made of aluminium (at 0.7 K and 3.5 K) and copper (at 50 K), respectively. They are enclosed by an outermost tube (1) with an outer diameter of 80 mm that acts as a vacuum tube and also as the first stage of the magnetic shielding as it is made of a soft magnetic alloy[4]. A very good magnetic shielding from external fields is needed for the operation of the SQUID current sensors as well as the detector array, especially in environments with variable magnetic fields. The magnetic shielding is further improved by the innermost radiation shield that is made of aluminium and has a temperature of around 700 mK. At this temperature it is superconducting and expels magnetic fields due to the Meissner effect. The magnetic shielding is completed by an superconducting shield[5] made of niobium (5) that is directly attached to the copper arm. To prevent direct thermal contacts between the different shields spacers made of polystyrene are inserted between them at the end of the arm.

---

[4]Magnetic Shields Ltd, Headcorn Road, Tonbridge, Kent, TN12 0DS, United Kingdom
[5]WHS Sondermetalle, Industriepark ob der Tauber, Waltersberg 24, 97947 Grünsfeld, Germany

To allow X-ray radiation from external sources to enter the cryostat the radiation shields and the vacuum can are equipped with X-ray windows in front of the detector. The radiation shields are each equipped with a 6 µm thin Mylar foil[6] coated with about 40 nm aluminium with a diameter of 19 mm. As outermost, vacuum-tight window either a 25 µm thin foil[7] made of DuraBeryllium® with a diameter of 13 mm can be used if high transmissivity is needed, or alternatively a 150 µm thick polyimide foil with a diameter of 19 mm if a larger acceptance angle is required.

5.1.3   Wiring

The wiring for the read-out and operation of the SQUID current-sensors that are discussed in section 5.2.1 as well as the field and heater lines that are needed to prepare the persistent current (ref. section 4.3) in the detector are made of a copper-nickel alloy[8] between room temperature and the 3.5 K stage. The use of copper-nickel instead of copper involves a smaller thermal conductivity between the different temperature stages. The wiring for field and heater lines that have to carry currents up to 200 mA as well as the wires of the voltage measurement of the read-out, that is performed in a three-wire measurement to increase its accuracy, have a diameter of 200 µm and an electrical resistivity of 1.57 Ω/m. All other wires are made of smaller diameter of 100 µm and a resistivity of 6.47 Ω/m to reduce their thermal conductance. For the lower temperature stages wires consisting of superconducting niobium-titanium multifilaments in a copper-nickel matrix[9] with a diameter of 50 µm were used to reduce the electrical power dissipation. To minimize the susceptibility to external magnetic fields all wires that form a go-and-return line are made of twisted pairs or twisted triples, respectively. On all temperature stages of the cryostat the wires were thermally anchored to ensure the lowest possible heat load on the colder stages. At the mixing chamber the wiring ends in high density connectors[10]. These are connected to semi-rigid, multi-layer circuit boards[11] that are attached to the four sides of the outer copper side arm where they are connected to four circuit boards on which the second stage SQUID arrays are placed as depicted in figure 5.3.

Each of these boards is equipped with a total of 8 second-stage SQUID channels. The first-stage SQUIDs are directly attached to the experimental holder in close distance to the detector array and are connected to the second stage SQUIDs with flexible

---

[6]ES301865 from Goodfellow GmbH, 61213 Bad Nauheim, Germany

[7]MOXTEK, 452 West 1260 North, Orem, UT 84057, USA

[8]Alloy 30 from Isabellenhütte, Eibacher Weg 3-5, 35683 Dillenburg, Germany

[9]Purchased from European Advanced Superconductors; now Bruker EAS, Ehrichstraße 10, 63450 Hanau, Germany

[10]LTH/LSH series from Samtec, 520 Park East Boulevard, New Albany, IN 47150, USA

[11]Würth Elektronik GmbH & Co. KG, Circuit Board Technology, Salzstraße 21, 74676 Niedernhall, Germany
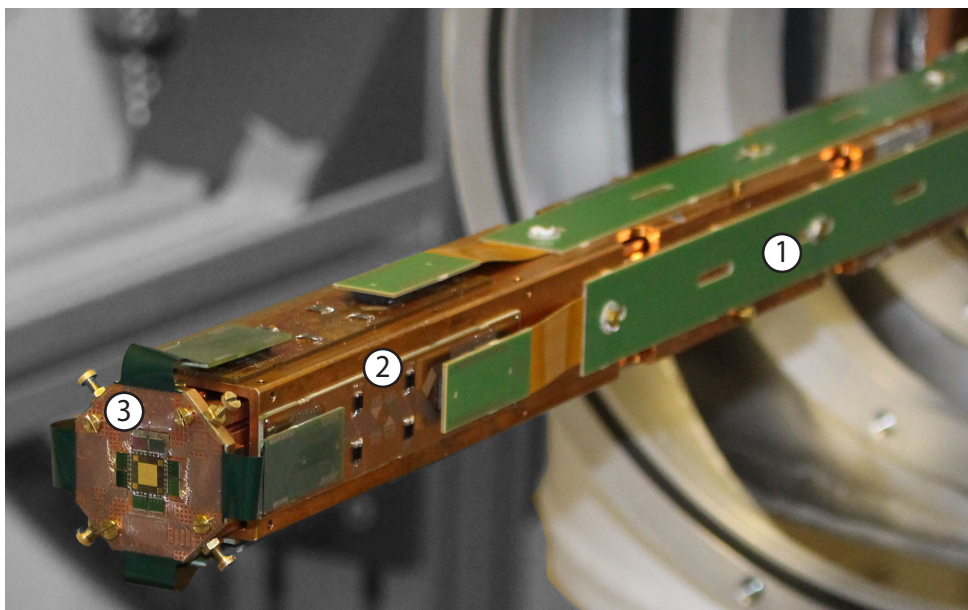
Figure 5.3: Photograph of the end of the side arm including the semi-rigid circuit boards (1), the amplifier circuit boards (2) and the detector platform (3).

circuit boards. The experimental platform will be described in more detail in section 5.3. Altogether the cryostat is equipped with 32 two-stage SQUID channels at the end of the arm and 3 additional channels ending on the mixing chamber platform.

5.1.4 Thermometry

All the relevant temperature stages (at around $50\,\mathrm{K}$, $3.5\,\mathrm{K}$, $700\,\mathrm{mK}$, $10\,\mathrm{mK}$) of the cryostat and the end of the inner side arm are equipped with resistance thermometers. They are read out with an AC resistance bridge Model 370 in combination with the Scanner 3716, both from Lake Shore Cryotronics[12]. The thermometer at the end of the side arm is made of RuO and shows a sensitivity of $\mathrm{d}\log\left(R\right)/\mathrm{d}\log\left(T\right) \approx 1.4$ in the range between $20\,\mathrm{mK}$ and $40\,\mathrm{mK}$. Calibration towards even lower temperatures was done by mounting the thermometer on the mixing chamber platform and taking the thermometer of the mixing chamber that was delivered with the cryostat as reference thermometer.

---

[12]LakeShore Cryotronics Inc, 575 McCorkle Boulevard, Westerville, Ohio, USA

5.2   Data read-out

In section 3.4 it was shown how an incident X-ray photon changes the magnetic flux in the pick-up coil of a magnetic calorimeter. Thereby it creates a current I_S in the input coil of a SQUID current sensor that creates a magnetic flux $\Delta\Phi_S = M_{is}I_S$ in the SQUID via the mutual inductance M_{is} between SQUID loop and the input coil. In the following section the basic working principle of a SQUID current sensor is shown as well as the two-stage SQUID setup that was utilized for the measurements and that includes a low temperature amplifier as well as a linearization of the SQUID signal. The chapter closes with a description of the new 32-channel data acquisition system that was set up in the framework of this thesis.

5.2.1   SQUID current sensor

SQUID[13] current sensors are devices that allow a highly sensitive determination of a change of magnetic flux $\Delta\Phi_S = M_{is}I_S$ that is created by a current I_S in an input coil of the SQUID. They are based on the Josephson effect [Jos62] and explained in detail in [Cla04]. Below, the basic principles of two-stage dc-SQUID current sensors that have been used in the framework of this thesis are summarized.

Working principle of a dc-SQUID

Figure 5.4 shows a schematic illustration of a dc-SQUID. A dc-SQUID consists of a superconducting loop that is interrupted by two so called Josephson junctions.
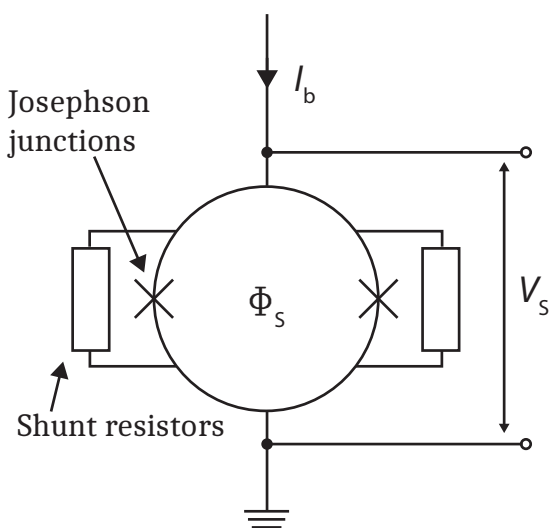

Figure 5.4: Schematic drawing of a dc-SQUID consisting of a superconducting loop that is interrupted by two Josephson junctions. The junctions are shunted to prevent hysteretic behaviour of the SQUID.

---

[13]Superconducting Quantum Interference Device

These can be realized for example by very thin non-superconducting contacts, typically in the order of a few nanometers thick and allow magnetic flux to enter or leave the loop. To avoid hysteretic behavior of the SQUID, both junctions are shunted with a resistor. If a dc-SQUID is operated with a small bias current I_b, the Cooper pairs [Coo56] of the superconducter can tunnel through the thin barriers and carry the current without a voltage drop over the SQUID as long as the current does not exceed a certain critical current I_c. This critical current depends on the magnetic flux Φ_S that is enclosed by the SQUID loop and shows a periodic behaviour where the periodicity is given by the magnetic flux quantum $\Phi_0 = h/2e \approx 2.07 \times 10^{-15}\,\text{Wb}$. For larger currents $I_b > I_c$ the current can no longer be carried only by Cooper pairs but also by quasiparticles that tunnel through the barrier. This leads to a voltage drop V_S across the SQUID that is depicted on the left-hand side of figure 5.5 in dependence of the bias current I_b for the two extreme values of the magnetic flux Φ_S in the SQUID.
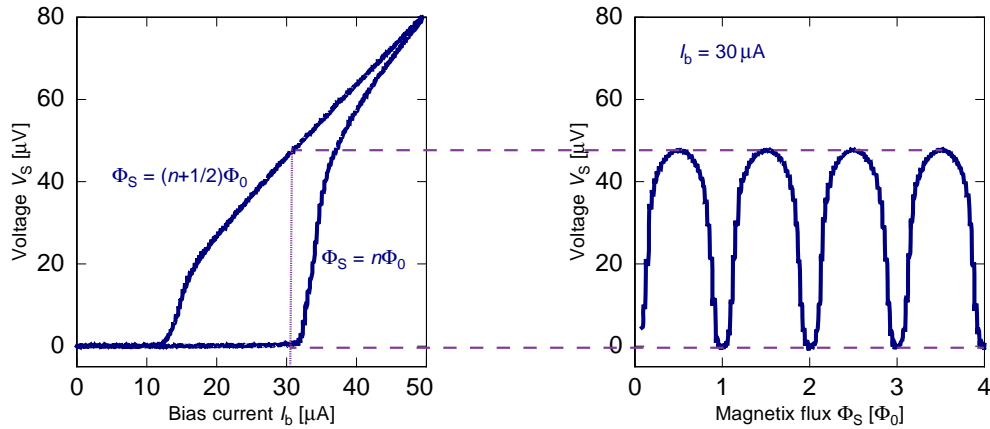
Figure 5.5: Current-voltage characteristics **(left)** for the two extreme values of the enclosed magnetic flux Φ_S and voltage-flux characteristics **(right)** for a constant bias current I_b of a dc-SQUID. Here n denotes a natural number.

The dependence of the IV-characteristics on the enclosed magnetic flux Φ_S for large enough bias currents leads to a flux-dependent voltage drop $V_S(\Phi_S)$ as depicted on the right-hand side of figure 5.5. This behaviour can be used to precisely monitor a flux change, however due to the periodic nature of the $V\Phi$-characteristics the resulting signal would be highly non-linear as soon as signals get larger than $\Phi_0/4$. This disadvantageous behaviour can be eliminated by a feedback mechanism that will be described in the following section.

Two-stage setup and linearization of the SQUID signal

In a single-stage SQUID setup as shown in the previous section the noise of the read-out chain would be dominated by the noise of the room temperature electronics[14] that is used to provide the bias current I_b and to measure the voltage drop V_S. To increase the signal and to thereby decrease the influence of the room temperature electronics with respect to the signal a low-noise amplifier is needed. In a two-stage SQUID setup a second SQUID, for example a N-SQUID series array, operated at low temperatures is used for this purpose as depicted in figure 5.6.
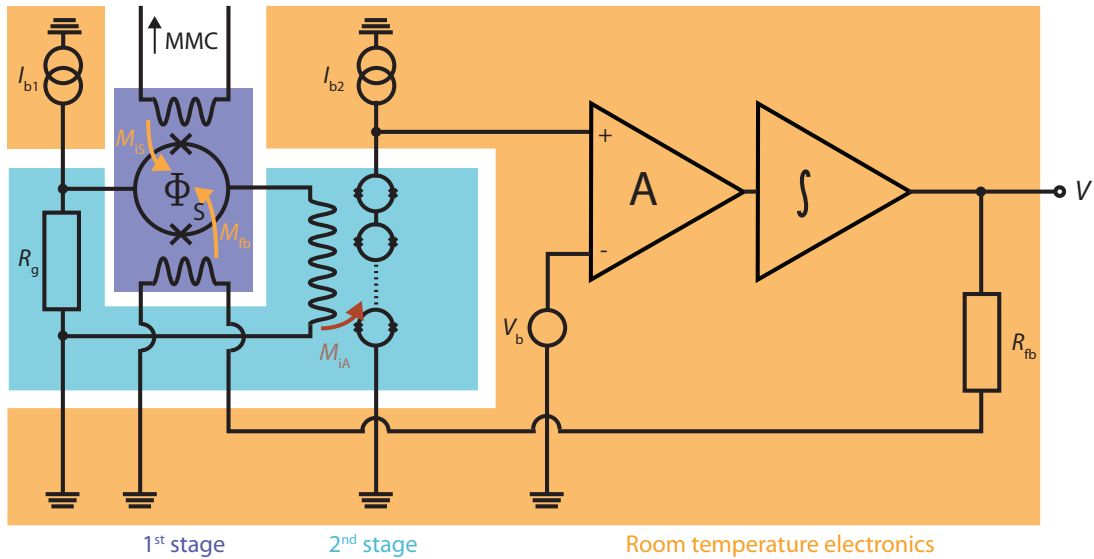

Figure 5.6: Schematic drawing of a two-stage SQUID configuration. The first-stage SQUID is marked in violet and is operated in voltage-bias mode. The second-stage SQUID, which acts as a low-temperature amplifier and consists of an N-SQUID series array that is operated in current-bias mode, is marked in blue. The voltage drop across this SQUID array is read out by a room temperature electronics marked in orange. To linearize the signal a feedback mechanism is implemented that keeps the first-stage SQUID at a constant working point. All the current sources that are necessary to operate the SQUIDs are also part of the room temperature electronics.

The second-stage SQUID array is operated with a bias current I_{b2} as shown in the previous section. If the magnetic flux in the individual SQUID cells of the array is the same, their $V\Phi$-characteristics add up coherently and behave like a single SQUID with N times higher V_S. The first-stage SQUID is operated with a voltage bias to decrease the heat-load in close vicinity of the detector array and to match the low impedance input of the second-stage SQUID amplifier. For this purpose the bias

---

[14]XXF-1 from Magnicon GmbH, Barkhausenweg 11, 22339 Hamburg, Germany

current I_{b1} flows through a gain resistor with resistance R_g. If this resistance is much smaller than the resistance of the SQUID in the normal conducting state, the current generates an almost constant voltage bias while only a current $I \ll I_{b1}$ flows through the SQUID and the input inductance of the second-stage SQUID that is connected in series to the first-stage SQUID. As this current I depends on the magnetic flux in the first-stage SQUID such a setup can be used to convert a magnetic flux change Φ_S in the first-stage SQUID into a flux change in the amplifier array. Thereby the power dissipation at the first-stage SQUID can be reduced up to one order of magnitude. Instead, a larger amount of power is dissipated in the gain resistor which can however be placed far away from the first-stage SQUID.

As shown in the previous section the $V\Phi$-characteristics of a SQUID is highly non-linear and not even monotonous. Therefore, it is necessary to linearize the signal which is done with a technique called flux-locked loop. A flux change $\Delta\Phi_S$ in the first-stage SQUID, for example caused by a magnetic calorimeter, leads to a current change in the input coil of the second-stage SQUID where it generates a voltage drop. This is amplified with respect to an offset voltage V_b by a differential room temperature amplifier. The resulting voltage difference is integrated and fed back to the first-stage SQUID via a feedback resistance R_{fb}. The thereby generated current I_{fb} flows through a feedback coil and generates a flux $M_{fb}I_{fb}$ in the first-stage SQUID that exactly compensates the initial flux change $\Delta\Phi_S$. As a result the SQUID is always operated at the same point of the $V\Phi$-characteristics – the so-called working point – and the voltage drop across the feedback resistor can be used as linearized output signal that is proportional to the flux change Φ_S. For maximum sensitivity the bias voltage V_b is chosen in such a way that the steepness of the $V\Phi$-characteristics and for that reason also the signal-to-noise ratio is maximized at the working point while the bias currents I_{b1} and I_{b2} are chosen in a way that the voltage swing is maximized.

In summary a current I_S in the input coil of the first-stage SQUID, that is for example created by a temperature change of a connected micro-calorimeter as shown in chapter 3.4, creates an output voltage

$$V = \frac{R_{fb}}{M_{fb}}\Delta\Phi_S = R_{fb}\frac{M_{iS}}{M_{fb}}I_S \tag{5.1}$$

where M_{fb} and M_{iS} are the mutual inductances between the corresponding coils and the SQUID loop. They are given by $M = k\sqrt{L_S L_x}$ where k is a geometric coupling factor, L_S the inductance of the SQUID loop and L_x the inductance of the corresponding coil coupling to the SQUID.

Noise contributions

A two-stage SQUID setup as shown in the previous section shows several additional contributions to the noise of the detector. They can be divided into a frequency-independent white noise and a $1/f$-component that increases towards lower frequencies. The dominatiing contribution is the noise of the SQUIDs themselves while the additional white noise contributions due to the gain resistor and the room temperature electronics are negligible if the voltage swing of the second-stage SQUID is large enough. The white noise of the SQUIDs is generated by the shunt resistors with a resistance R which generate in-phase and out-of-phase voltage noise that can be interpreted as a magnetic flux noise with power density

$$S_{\Phi_S}^{w} = \frac{18 k_B T L_S^2}{R} \tag{5.2}$$

for an ideal SQUID geometry with SQUID inductance L_S [Tes77, Bru82]. For a SQUID with $R = 8\,\Omega$ and $L_S = 80\,\mathrm{pH}$ at a working temperature of $T = 200\,\mathrm{mK}$ we, therefore, calculate a white noise level of $\sqrt{S_{\Phi_S}^{w}} \approx 100\,\mathrm{n}\Phi_0/\sqrt{\mathrm{Hz}}$. The relatively high temperature that is assumed in this case is due to self-heating effects in the shunt-resistors and decoupling from the phonon bath. The additional $1/f$-contribution which dominates at low frequencies shows a typical noise density in the order of $\sqrt{S_{\Phi_S}^{1/f}} \approx 5\,\mu\Phi_0/\sqrt{\mathrm{Hz}} \times f^{-\xi}$, where $\xi = 0.6 \dots 1.2$ [Kem16]. The exact origin of this noise source is not yet fully understood, one possible reason are flipping magnetic moments on the surface of the SQUID loop [Koc07] originating at least in parts from adsorbates [Kum16, dG17].

5.2.2   Data acquisition and signal processing

For data acquisition two different systems were used. For all characterization and spectroscopic measurements that only involved up to two detector channels a digitizer card[15] with two input channels was used. It has a resolution of 12 bit and a maximum sampling frequency of 100 MHz. For each triggered signal 16384 samples are saved, the acquired number of samples however may be up to eight times larger due to oversampling. Depending on the situation either 25 % or 50 % of the saved samples are acquired before the actual trigger. For non-gradiometric detectors these so-called pretrigger samples contain information about the chip temperature which can be used to correct for temperature variations. Depending on the desired measurement settings the two channels can either be used independently where each channel has a separate internal trigger engine, or they can be used in conjunction where one

---

[15]CompuScope 12100 from GaGe, 900 North State Street, Lockport, IL 60441, USA

channel is used as a trigger channel and the other channel is used for the actual data. That allows to heavily filter the trigger channel with a band pass filter[16] while at the same time the data can be acquired with different filter settings. This digitizer also allows the acquisition of untriggered noise. These so-called baselines were used to apply an optimal filtering algorithm [Fle03] to the data to extract the pulse height from the individual signals.

New parallel acquisition system for up to 32 channels   For the read-out of up to 32 channels a new acquisition system was set up in the framework of this thesis. It is based on two 16-channel digitizer cards SIS3316[17] with a maximum sampling rate of 125 MHz per channel and a resolution of 16 bit. Both cards are combined in a VME crate and read out via a SIS1100/3100[17] connection based on an optical gigabit link. Due to a double-memory system these cards support simultaneous acquisition of data and data transfer to the computer allowing for high throughput. Internally each channel is split into a trigger channel and an unmodified data channel. The cards feature individual trigger engines for each channel that are based on a moving average window and a FIR[18] filter. In this way the characteristics of an internal bandpass filter are modelled and the use of additional external filters is no longer necessary. Furthermore, the trigger engine implements a constant fraction discriminator which has the task to trigger all signals at the same time relative to the time of the signal maximum regardless of the signal height. In contrast to a fixed threshold discriminator the use of a constant fraction discriminator is beneficial for optimal filtering where it is assumed that all signals show the same signal shape which includes reaching the signal maximum always after the same time interval after triggering. The cards support oversampling up to a factor of 512 and by default 16384 samples are saved for each triggered event.

The acquisition software that was written in the framework of this thesis is distributed to several C++ programs to ensure scalability and modularity. Figure 5.7 shows a simplified flowchart of the software architecture. The main work is done by three programs which are all launched by the separate ***PAQS_Launcher***. The distribution to individual programs supports the utilization of multi-core processors. To transfer data as well as control signals between the programs a way of inter-process communication is needed. In the current version of the programs this is based on named pipes offered by the operating system by creating FIFO[19] structures that are stored in external files. By replacing the modules that are responsible for the commu-

---

[16]SR560 from Stanford Research Systems, 1290-D Reamwood Avenue, Sunnyvale, CA 94089, USA
[17]Struck Innovative Systeme GmbH, Harksheider Str. 102, 22399 Hamburg, Germany
[18]Finite Impulse Response
[19]first in, first out

nication with other modules that support TCP/IP[20] even distributing the programs
to different computers might be possible in future versions of the acquisition system.
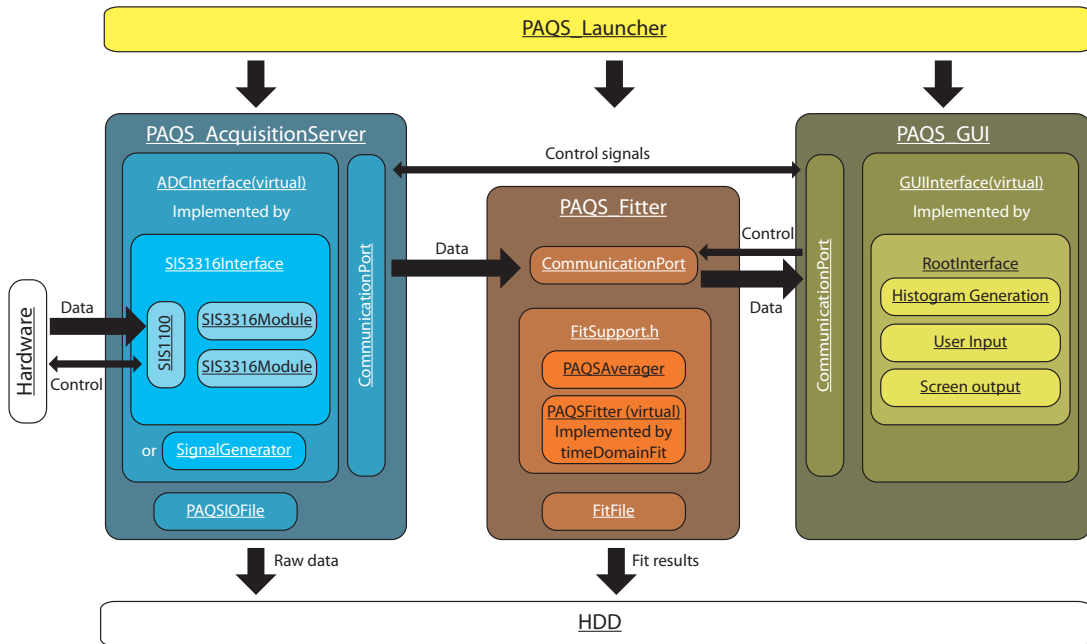

Figure 5.7: Flowchart of the software for the new data acquisition system. Further details
are given in the text.

The **PAQS_AcquisitionServer** is responsible for the direct control of the actual
hardware and for saving the triggered raw signals to disk. Furthermore it determines
relevant timestamps of each recorded signal and calculates some basic features, like
signal area and raw signal height, that can be determined in a single pass through
the associated array of digitized voltage values. The polarity of each pulse is also
determined with the help of additional information about the trigger signal which are
read from the ADC. For other digitizer cards that do not offer appropriate informa-
tion, the polarity can be determined for example by the sign of the signal area. The
knowledge about the polarity is essential for the subsequent distribution of the sig-
nals to the appropriate *PAQS_Fitter* programs as the two polarities of each read-out
channel are directly connected to two different pixels (ref. section 3.4.3). The core of
the *PAQS_AcquisitionServer* is the virtual class *ADCInterface* that defines a general
interface for digitizers. This includes functions to set or read ADC parameters, to
start and stop the acquisition and to read the actual data. Currently this class is
implemented for two combined SIS3316 digitizers for the actual data acquisition as
well as for a simple signal generator that is able to create artifical signals to test
the acquisiton software and algorithms. Due to the modular approach, exchanging

---

[20]Transmission Control Protocol based on the Internet Protocol

the actual digitizer only requires deriving a new class from *ADCInterface* and an implementation of the functions that are defined within this base class without the need for changing other parts of the *PAQS_AcquisitionServer* like the communication module or the *PAQSIOFile*. The latter is responsible for saving the raw data as well as the acquisition settings for each channel.

To account for small differences in the different pixels of a detector array it is important to configure the fitting procedure for each pixel individually. Therefore, the **PAQS_Fitter** is launched twice per ADC channel (once for positive and negative signals). It is responsible for any data analysis that involves advanced signal processing which is, therefore, not done initially by the *PAQS_AcquisitionServer*, like for example the determination of the actual signal amplitude from the raw data by fitting algorithms. The amplitude is saved to disk by the *FitFile* together with other fit results like rise and decay time of the signals. All fitting parameters are appended to the corresponding signal which is thereafter sent to the *PAQS_GUI*. The *PAQS_Fitter* also provides a module to average signals which is necesseray to configure several of the possible fitting algorithms. So far only an algorithm based on the method of least squares, comparing each signal with a user-defined averaged pulse, was implemented. Therefore, all measurements done with this acquisition system are analysed with this method. However, expanding the algorithm with other fitting techniques by deriving of the virtual interface class *PAQSFitter* can be done in future. For example the additional acquisition of baseline signals and implementation of a module performing fast Fourier transform would allow the use of an optimal filtering algorithm.

The **PAQS_GUI** serves as graphical user interface and displays the raw signals as well as the associated data like the signal amplitude. This program also creates a histogram from the incoming data, thereby showing a live amplitude spectrum during acquisition. It communicates with the *PAQS_AcquisitionServer* to acquire available settings of the digitizers, to read and set these settings and to start or stop the acquisition. Communication with the *PAQS_Fitters* includes accepting and rejecting individual signals by the user to compose the average signal that is needed to configure the fitting modules.

Besides the acquisition of signals additionally a 32-channel virtual oscilloscope was implemented to allow the monitoring of the output signals of all the SQUID electronics while remotely tuning the parameters of the 32 SQUID channels. Additionally a possibility for noise measurements between $10\,\mathrm{Hz}$ and $4\,\mathrm{MHz}$ was included.

5.3   Experimental setup

The different detector arrays *maXs200* and *maXs30* that were used in the framework of this thesis were mounted on a dedicated experimental platform at the end of the side arm described in section 5.1.2. Figure 5.8 depicts a CAD drawing of the platform and shows the position of the detector and the first-stage SQUID chips. Additionally depicted is a collimator that may optionally be placed above the detector to protect the SQUIDs and the substrate of the detector chip from incident X-rays.
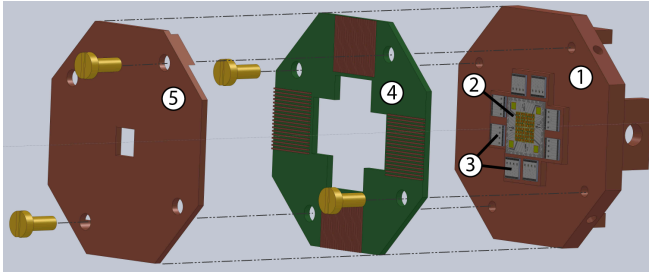

Figure 5.8: Exploded drawing of the experimental platform (1) including the detector chip (2) and first-stage SQUID chips (3), the circuit board (4) and the optional collimator (5).

To ensure a good thermal conductivity the platform and the collimator were made of copper and in addition the platform was annealed at $800\,^\circ$C for 12 h to further increase its thermal conductivity. Figure 5.9 depicts a close-up photograph of the detector setup showing the aforementioned detector and SQUID chips.
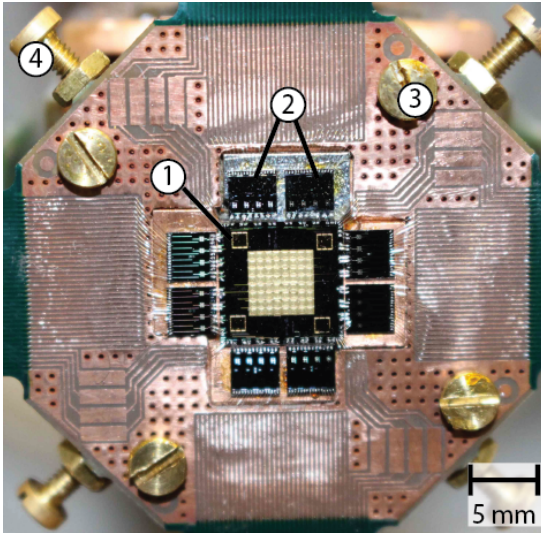
Figure 5.9: Exemplary photograph of a detector setup including a *maXs30* detector chip (1) that is surrounded by eight SQUID chips (2), each providing four first-stage SQUID current-sensors of the types *HDSQ1-FE* or *HDSQ2d-FE*, respectively. For better visibility the collimator was removed. The screws (3) that fix the circuit board to the platform can also be used to mount the collimator. The superconducting niobium shield that is part of the magnetic shielding is supported by screws (4) in the side of the platform.

A hole in the circuit board allows the chips to be glued directly to the experimental platform with the low temperature varnish GE-7031[21] to ensure a good thermal contact to the side arm. To minimize the heat load from the SQUID chips to the detector array special care was taken to ensure a small gap between the individual

---

[21]LakeShore Cryotronics Inc, 575 McCorkle Boulevard, Westerville, Ohio, USA

chips. On the other hand the size of the gap was chosen as small as possible (typically around 300 µm) to reduce the length, and thereby the parasitic inductance, of the bonding wires that create the electrical contact between the chips. The wires have a diameter of 25 µm, are connected using wedge-bonding and typically have a length of around 500 µm. Between detector chip and first-stage SQUID chips each contact is made by two bonds in parallel to further reduce their parasitic inductance.

Detectors Besides the two-dimensional *maXs30* detector array that was described in detail in chapter 4, a *maXs200* detector array was used for the experiments performed in the framework of this thesis. This linear detector array is thoroughly described in [Pie12]. It features eight single pixels with an absorption area of 500 µm × 2000 µm each and is depicted on the left-hand side of figure 5.10.
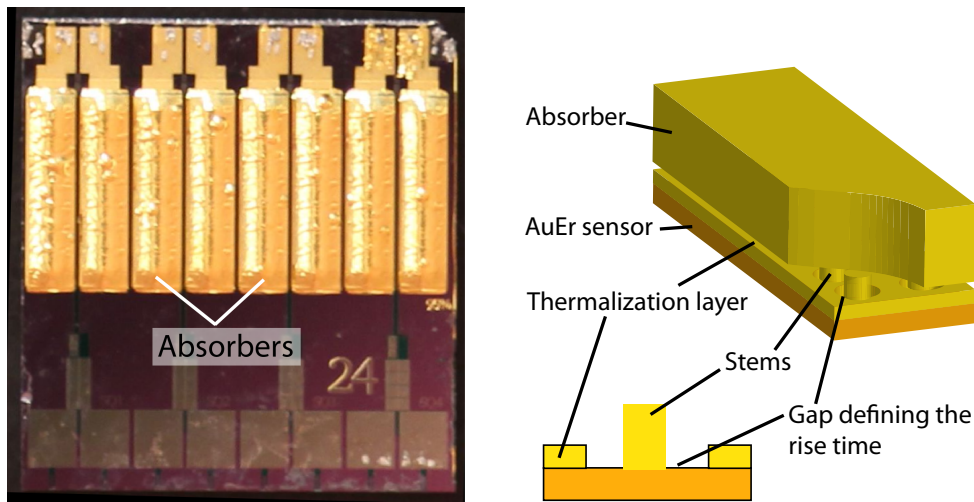
Figure 5.10: Left-hand side: Photographic image of the *maXs200* detector chip used for one of the experiments at the GSI. **Right-hand side:** Schematic drawing of a single *maXs200* absorber resting on stems. Also shown is the extra thermalization layer to ensure quick thermal equilibration across the large area temperature sensor. The holes inside this layer reduce the signal rise time of the detector.

The absorbers are made of 200 µm thick gold and – in contrast to the detector described in [Pie12] – are separated from the associated Au:Er sensor by 16 stems made of gold, each with a diameter of 30 µm. The right-hand side of figure 5.10 shows a schematic drawing of a single absorber and its associated sensor. To increase the thermal conductivity along the relatively large sensor an additional layer made of 2.5 µm thick gold is electroplated on top of the sensor before fabricating the stems and the absorber. To limit the signal rise time, this layer is recessed circularly around each stem with a diameter of 50 µm as depicted in figure 5.10. Therefore, the signal rise time is given by the thermal conductivity of the small sensor region between

stems and thermalization layer, resulting in an expected signal rise time of about $10\,\mu s$ matching the time in which position dependencies of the signal shape were found [Pie12]. With the Er^{3+} concentration of $750\,ppm$, a sensor height of $3.5\,\mu m$ and a field generating persistent current of $70\,mA$ an energy resolution below $30\,eV$ is expected for this detector at a working temperature of $20\,mK$.

First-stage SQUIDs   As first-stage SQUID chips home-made chips of the types *HDSQ1-FE* and *HDSQ2d-FE*, each with four independent single-stage SQUID current-sensors, were used. On these chips two slightly different designs of gradiometric washer SQUIDs that are described in detail in [Fer15, Her16] are present. Table 5.1 summarizes typical values for the parameters of both designs that are relevant for the characterization and read-out of metallic magnetic calorimeters according to equations 5.1 and 3.32. However, these values may slightly vary for individual SQUIDs.

	Design 1	Design 2
Mutual inductance $1/M_{\mathrm{fb}}$ [$\mu A/\Phi_0$]	12.7	12.4
Mutual inductance $1/M_{\mathrm{iS}}$ [$\mu A/\Phi_0$]	35.5	35.8
Input coil inductance [nH]	1.60	1.28

Table 5.1: Relevant parameters of the first-stage SQUID current-sensors that were used in the framework of this thesis; taken from [Her16].

Second-stage SQUIDs   Figure 5.11 shows a photograph of one of the four circuit boards with the amplifier arrays that are attached to the outer copper arm. The amplifier SQUIDs that were used in the experiments are arrays of the type *C6X16FL*[22] as well as home-made SQUID arrays of the types *HDSQ1-A16* and *HDSQ2d-A16*.
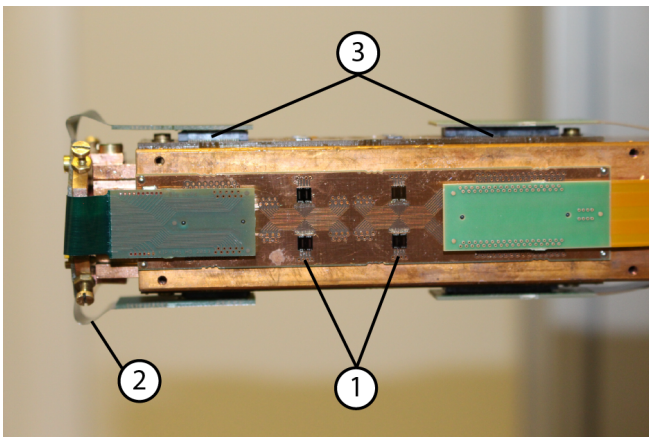

Figure 5.11: Amplifier board with eight 16-SQUID arrays distributed over four individual chips (1) mounted on the side arm of the cryostat. Also visible are the semi-rigid circuit boards (2) with the high density connectors[10] (3).

---

[22]PTB, Abbestr. 2-12, 10587 Berlin, Germany

All three designs feature two series arrays per chip, each consisting of 16 individual SQUID cells. The chips were glued onto the respective circuit boards with the same varnish[21] that has been used as for the chips on the experimental platform. To increase the thermal contact of the chips to the outer copper arm, copper vias through the circuit board were included underneath the SQUID chips.

The highly modular design with first-stage SQUIDs on the detector platform and multiple separated second-stage SQUID boards facilitates the quick and easy exchange of defect amplifier SQUIDs or even the detector platform. Therefore, it is for example even possible to exchange the detector during a beam time at a storage ring in order to adjust the detector properties according to the investigated excited ions. The flexible parts of the circuit boards allow the space-saving mounting of detector and amplifier boards on different sides of the side arm. The setup is completed by the superconducting niobium shield that acts as a magnetic shielding for the detector arrays as well as the first- and second-stage SQUIDs as explained in section 5.1.2. It is held in place by the edges of four brass screws at the sides of the platform which ensures a good mechanical contact to reduce vibrations of the detector with respect to the shield. Otherwise magnetic flux that might be trapped in the niobium shield would create additional flux noise in the detector or the SQUIDs. This solution without the need of additional holes was chosen to maximize the shielding effect. To finally reduce magnetic Johnson noise by the copper platform a $1\,\mu m$ thick superconducting niobium layer has been deposited beneath two of the SQUID chips as well as on the bottom side of the collimator that is facing the detector.

5.4 X-ray sources

In the following the two external radioactive X-ray sources that were used to calibrate the individual spectra discussed in section 6.2 and to characterize the detectors are briefly discussed. Thereafter the basic working principle of the gas jet target that is located at the experimental storage ring (ESR) at the GSI[23] is shown. At this target several experiments with highly charged ions were performed in the framework of this thesis.

5.4.1 ^{241}Am source

The main calibration source was an ^{241}Am source that undergoes an α-decay to ^{237}Np with a half-life of 433 years. The α-particle created in that process is absorbed by the housing of the source. The X-rays and γ-photons that are emitted during the

---

[23]GSI Helmholtzzentrum für Schwerionenforschung GmbH, Planckstraße 1, 64291 Darmstadt, Germany

decay or in the subsequent deexcitation of the daughter atom, however, may leave the encapsulated source through a $250\,\mu m$ thick beryllium window. The resulting energy spectrum is described in detail in [Pie12] and covers a range from $10\,keV$ up to $60\,keV$ and is, therefore, perfectly suited to study the detector response and non-linearity of a metallic magnetic calorimeter over a large energy range. Relevant intensities and energies can be found in [Des03, Lép08, Bea67, Bé10]. The activity of the source[24] that was used for the characterization of the *maXs30*-detector was $370\,kBq$. For the measurements at the GSI a similar ^{241}Am calibration source was used, however with a different housing.

5.4.2 ^{55}Fe source

The isotope ^{55}Fe undergoes an electron capture process with a half-life of 2.74 years. As the captured electron originates with a high probability from the K-shell the daughter atom ^{55}Mn remains in an excited state and deexcites by emission of Auger electrons or X-ray photons. The electrons are stopped by a $200\,\mu m$ thick beryllium window while the X-rays that are dominated by the K_α and the K_β lines around $5.9\,keV$ and $6.5\,keV$ can penetrate the window. The K_α line exhibits a hyperfine splitting of $12\,eV$ that can be resolved by high resolution X-ray detectors. The respective energies and intensities can be found in [Höl97][25]. The source[26] used in the described experiments had an activity of around $5\,MBq$ at the time of the measurements.

5.4.3 Gas jet target at the ESR

The highly charged ions that acted as an X-ray source for some of the performed measurements were produced at the GSI in Darmstadt. For these experiments the cryostat was transported and set up at the gas target of the ESR together with the detector. In the following a short overview about the generation of the highly charged ions and the interaction processes within the gas target that lead to X-ray emission is given.

---

[24]Eckert & Ziegler Nuclitec GmbH, Gieselweg 1, 38110 Braunschweig, Germany

[25]Corrected values for some lines according to private communications with E. Förster can be found in [Lin07].

[26]Nycomed Amersham plc, now GE Healthcare, Amersham Place, Little Chalfont, Buckinghamshire, HP7 9NA, United Kingdom

Beam generation and storage

An overview over the facilities at the GSI is given in [Spi05]. In order to produce highly charged ions, low to medium charged ions are initially accelerated up to $11\,\mathrm{MeV/u}$ in the $120\,\mathrm{m}$ long linear accelerator UNILAC[27]. Thereafter they are accelerated further in the ring accelerator SIS18[28] with a circumference of $216\,\mathrm{m}$ up to $90\,\%$ of the speed of light. On their way to the ESR the relativistic ions then pass a stripper foil typically made of carbon. Due to interactions with the electrons of the thin foil the ion is stripped by most or all of its remaining electrons and enters the ESR as highly charged ion. At the heavy ion storage ring ESR the highly charged ions are accumulated, focused and decelerated [Fra87]. By using an electron cooler the velocity spread can be minimized down to 1×10^{-5}. With a circumference of around $108\,\mathrm{m}$ and a rigidity of $10\,\mathrm{T\,m}$ ions from helium up to bare uranium can be stored with velocities between $10\,\%$ and $90\,\%$ of the speed of light.

Internal gas jet target

In the internal gas jet target of the ESR that is described in detail in [Gru89, Rei97], the stored ion beam can be crossed with a vertical gas stream. Several gases, amongst others H_2, N_2 and Xe are available with target densities ranging from $2 \times 10^{12}\,\mathrm{cm}^{-3}$ to $5 \times 10^{13}\,\mathrm{cm}^{-3}$. Depending on the ion energy, ion charge state, target density and mass of the target atoms different interaction processes between the ion beam and the gas target might occur. Most of these processes result in excited highly charged ions that emit XUV and X-ray radiation during deexcitation, which may leave the interaction chamber via several X-ray windows made of steel, diamond or beryllium. Typically the gas target was a vertical beam with a diameter of $5\,\mathrm{mm}$ leading to a small but relevant uncertainty of the exact interaction point and thereby causing a Doppler broadening as shown in the following section.

Measurements at the internal gas target

In the framework of this thesis three different measurement campaigns at the gas target of the ESR have been performed [Kel14, Hen15]. An exemplary photograph showing the cryostat next to the gas target is depicted in figure 5.12. The exact measurement conditions of each campaign including beam energy, type of the gas target and beam as well as position of the magnetic micro-calorimeter relative to the gas target are given in the appropriate sections of chapter 6.

---

[27]Universal Linear Accelerator
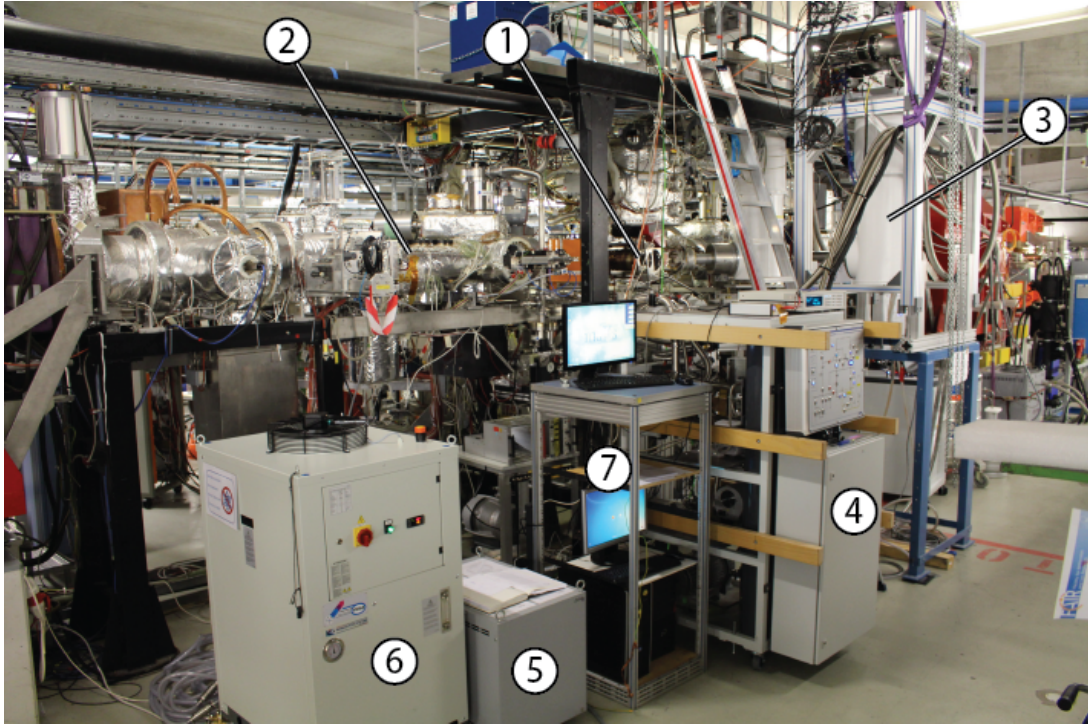[28]Schwerionensynchrotron 18 - German for "'Heavy Ion Synchrotron 18"'

Figure 5.12: Exemplary photograph of the measuring setup at the gas jet target (1) of the ESR (2) from the third measurement campaign. The magnetic calorimeter was mounted in the cryostat (3). The additional equipment of the setup is also depicted: gas handling system, thermometry and valve control (4) of the cryostat; compressor (5) that creates the needed pressure for the pulse tube cooler; cooling water supply (6); computers for remote control of the cryostat and data acquisition (7).

One important aspect of measurements at the ESR is the Doppler shift and the associated Doppler broadening of the X-ray lines that are emitted from the highly charged ions. The Doppler shifted energy in the laboratory frame

$$E^{\text{lab}} = E^0 \frac{1}{\gamma \left(1 - \beta \cos \theta\right)} \tag{5.3}$$

of an X-ray photon with energy E^0 in the rest frame of the emitting ion only depends on the beam velocity v, given by the Lorentz factor $\gamma = 1/\sqrt{1 - \beta^2}$ with $\beta = v/c$ and on the azimuthal angle θ between the forward direction of the ion beam and the direction of detection. Due to the finite size of the gas target as well as of the detector the detection angle slightly varies for each detected photon resulting in a

Doppler width

$$\Delta E^{\mathrm{D}} = E^0 \left(\frac{1}{\gamma \left(1 - \beta \cos \left(\theta + \delta \theta\right)\right)} - \frac{1}{\gamma \left(1 - \beta \cos \left(\theta - \delta \theta\right)\right)} \right) \qquad (5.4)$$

where

$$\delta \theta = \arctan \left(\frac{\sqrt{s_{\mathrm{d}}^2 + s_{\mathrm{t}}^2 \sin^2 \theta}}{2d} \right) \qquad (5.5)$$

is the spread in detection angle that depends on the size s_{d} of the detector, the horizontal width s_{t} of the gas target and their distance d to each other.

To minimize the Doppler broadening it is, therefore, beneficial to decrease the beam energy. However this also decreases the X-ray intensities as a low energetic beam is absorbed stronger by the residual gas of the storage ring resulting in a decreased beam intensity. Reducing the size of the detector and increasing the distance between detector and gas target also reduces the Doppler width, however results in a smaller solid angle covered by the detector, again resulting in reduced intensities. Reducing the size of the gas target on the other hand would have direct positive impact and is currently under investigation. For the micro-calorimeter arrays that were used in the framework of this thesis and that have a pixel size between 0.5 mm and 2 mm the size of the detector pixels is negligible compared to the gas target with a diameter of 5 mm.

6. Experimental Results

In this chapter the results of the different measurements that were performed and analyzed in the framework of this thesis are presented. First the characterization of the *maXs30* detector is discussed, followed by a discussion of a spectrum of the calibration source ^{241}Am that was measured with this detector. The chapter is concluded with the results of the measurement campaigns at the Experimental Storage Ring ESR that were performed with the *maXs30* and the *maXs200* detector arrays, respectively.

6.1 Characterization of the *maXs30* detector

This section contains all the characterization measurements of the two-dimensional *maXs30* detector array that was developed and fabricated in the framework of this thesis and that is discussed in detail in chapter 4. This includes the determination and discussion of the energy resolution, the signal shape and the detector linearity. Furthermore, the crosstalk between different pixels is discussed as well as the variation of characteristic detector parameters over the 64-pixel array. The measurements were performed in three different runs on the chips *maXs30w1_09* and *maXs30w1_10* which originate from the same wafer, each of them focussing on different aspects of the detector.

6.1.1 Meander inductance

The inductance of the superconducting pick-up loop which is made of niobium can be determined in a noise measurement at temperatures between $1.2\,\mathrm{K}$ and $9.2\,\mathrm{K}$. In this temperature range the SQUID and the pick-up loop itself are superconducting but the bonding wires that connect the pick-up loop with the input coil of the SQUID current sensor and that are made of aluminium are still normal conducting. Therefore, at a temperature T the bonds with resistivity R exhibit a frequency-independent current noise with power density

$$S_{\mathrm{I}}^{\mathrm{b}} = \frac{4k_{\mathrm{B}}T}{R} \tag{6.1}$$

that couples directly to the SQUID via the mutual inductance M_{is} and thereby creates a flux noise $S_{\Phi_{\mathrm{S}}}^{\mathrm{b}} = M_{\mathrm{is}}^2 S_{\mathrm{I}}^{\mathrm{b}}$. Together with the resistance of the bonding wires

the total inductance L of the circuit forms a lowpass filter with the cut-off frequency $f_c = R/(2\pi L)$. Including the additional white noise $S_{\Phi_S}^{S,w}$ of the SQUID itself (ref. section 5.2.1) this results in an expected total noise with noise density

$$S_{\Phi_S} = M_{is}^2 S_I^b \frac{1}{1+(f/f_c)^2} + S_{\Phi_S}^{S,w} = M_{is}^2 \frac{4k_B T}{R} \frac{1}{1+(f/f_c)^2} + S_{\Phi_S}^{S,w} \qquad (6.2)$$
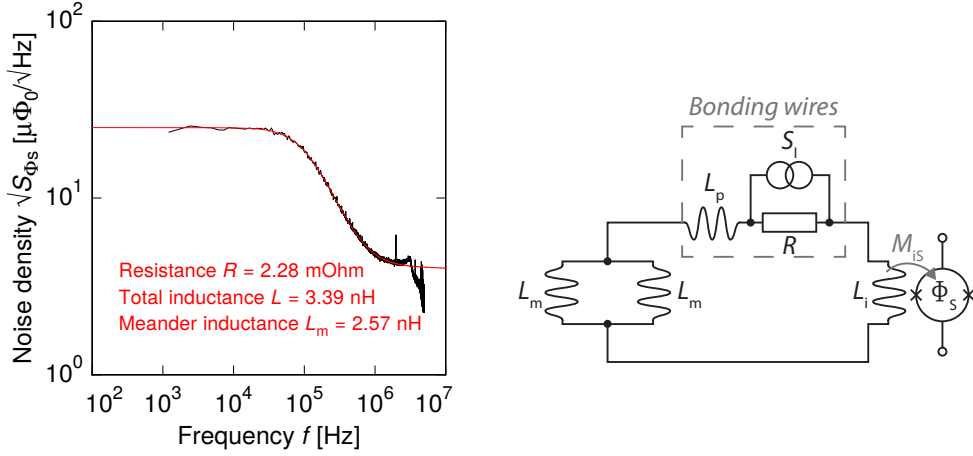
expressed as apparent flux noise in the SQUID.

Figure 6.1: Left-hand side: Measured noise density of the flux noise in the SQUID loop. Superimposed in red is a numerical fit describing the data. **Right-hand side:** Equivalent circuit including the detector, the SQUID current sensor and the bonding wires.

Figure 6.1 shows the measured flux noise S_{Φ_S} of a typical single detector channel of a *maXs30* detector in the SQUID at a temperature of 3.9 K in dependence of the frequency f. The measured data from 1 kHz to 5 MHz is shown in black, while a numerical fit based on equation 6.2 is superimposed in red together with the corresponding fit parameters. The agreement of data and the expected behaviour according to equation 6.2 is very good. The second cut-off around 3 MHz is due to the limited bandwidth of the SQUID feedback loop and was not included in the fit. The resulting total inductance of the circuit of $L = 3.39$ nH is composed of the inductances $L_m/2$ of the pick-up coil, L_i of the input coil of the SQUID and the parasitic inductance L_p. The latter is dominated by the inductance of the bonding wires that has been determined for two parallel bonds in independent measurements to be around (0.14 ± 0.04) nH per mΩ of bonding resistance, depending on the actual arrangement of the two bonding wires. An additional small contribution due to the approximately 4 mm long microstrip of the read-out of this specific detector channel is assumed to be 0.046 nH according to section 4.2. In total the expected parasitic inductance of this detector is around $L_p = 0.37$ nH. For the SQUID input coil of

SQUIDs of the same design an input coil inductance of $L_i = 1.74\,\mathrm{nH}$ was measured. Therefore, we can calculate the inductance

$$L_\mathrm{m} = 2(L - L_\mathrm{p} - L_i) = 2.57\,\mathrm{nH} \tag{6.3}$$

of a single meander. This value is only $0.11\,\mathrm{nH}$ or $4\,\%$ larger than the expected value of $2.46\,\mathrm{nH}$ (ref. table 4.3) and therefore matches the expected value perfectly within the uncertainty of the inductance of the bonding wires.

6.1.2 Absorber thickness

From the measurements with the ^{241}Am calibration source one can determine the intensity ratio of the two dominant γ-lines of the ^{241}Am source at $26.3\,\mathrm{keV}$ and $59.5\,\mathrm{keV}$. As the intensities of these lines are very well known from literature and taking into account absorption between source and detector by air or X-ray windows, one can calculate the expected ratio of photons that hit the detector. By comparing measured and expected ratio, the ratio of the absorption efficiencies η_{26} and η_{60} for both lines can be calculated. The left-hand side of figure 6.2 shows the expected ratio η_{26}/η_{60} as a function of the absorber thickness d.
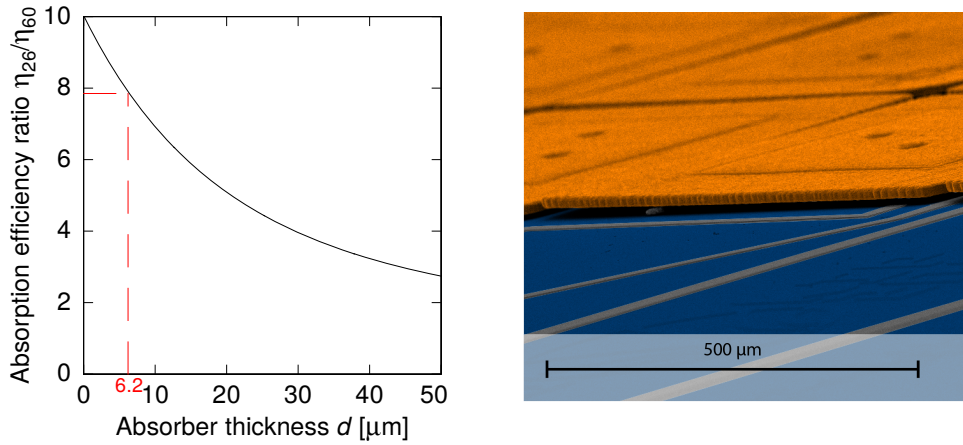
Figure 6.2: Left-hand side: Ratio of the absorption efficiencies for photons with an energy of $26.3\,\mathrm{keV}$ and $59.5\,\mathrm{keV}$, in dependence of the thickness of an absorber made of gold. The value that was determined for the investigated absorbers is marked in red. **Right-hand side:** Colored SEM image of *maXs30* absorbers from the same wafer as the detector chips that were investigated in the framework of this thesis.

From the measured intensities and including all known absorption by X-ray windows and air between source and detector a ratio of $\eta_{26}/\eta_{60} = 7.85$ was determined from the measurement, corresponding to an absorber thickness of $6.2\,\mu\mathrm{m}$. In principle the

technique above is a very good and reliable way to determine the absorber thickness, however, it is for example prone to unknown self-screening inside the source. Therefore, the thickness was additionally determined by a light microscopic measurement, resulting in a thickness of $(7.5 \pm 0.5)\,\mu\text{m}$. This measurement is also supported by a mass measurement of 55 absorbers that have been manually removed from a separate detector chip from the same wafer. With the mass of about $2.2\,\text{g}$ and taking into account the density of pure gold of $19.3\,\text{g/cm}^3$ this measurements yields a thickness of $(8.5 \pm 1.0)\,\mu\text{m}$. Taking into account all three measurements, an absorber thickness of $d \approx 7\,\mu\text{m}$ is assumed for further analyses in this thesis. This thickness is significantly smaller than the thickness of $20\,\mu\text{m}$ that was intended during the electroplating of the absorbers. Possible reasons are for example the formation of gas bubbles within the photo resist molds that could prevent the deposition of gold or a parasitic area that was accidentally electroplated alongside the absorbers.

6.1.3 Sensor magnetization

Figure 6.3 depicts the magnetic flux Φ_S in the SQUID current sensor, that is proportional to the magnetization of the paramagnetic sensor, in dependence of the inverse temperature. The left-hand side shows the data for the purposely non-gradiometric detector for a nominal field-generating current of $50\,\text{mA}$. Superimposed is the expectation for a non-gradiometric detector with an asymmetry of the sensors of about $18\,\%$ for different field-generating currents, based on the simulations described in section 3.3.6. The asymmetry of $18\,\%$ corresponds to the designed difference in size of the two sensors of the non-gradiometric detector. The measurement shows a good agreement with the simulation for an interaction parameter $\alpha = 12.5$ and a current of $25\,\text{mA}$ down to a temperature of about $30\,\text{mK}$, while for lower temperatures a decoupling of the detector temperature from the heat bath of the cryostat can be observed. The reduced current could be explained by a critical current of the niobium structures during the preparation of the field-generating persistent current of about $25\,\text{mA}$. This could be due to weak spots in the meander that might have been introduced during the wet etching process of the first niobium layer due to an inhomogeneous etching. The right-hand side shows the magnetization curve of a gradiometric detector of another chip from the same wafer for two different nominal currents. In contrast to the plot on the left-hand side the magnetization is given in $\text{m}\Phi_0$ instead of Φ_0, showing that the overall magnetization change is reduced by a factor of about 1000 compared to the non-gradiometric detector. In a perfectly gradiometric detector the signals of both pixels would compensate each other and no resulting change of magnetization for a change in temperature could be observed. Therefore, the observed signal is attributed to a very small asymmetry of around 1.5×10^{-4} of both pixels with respect to each other.
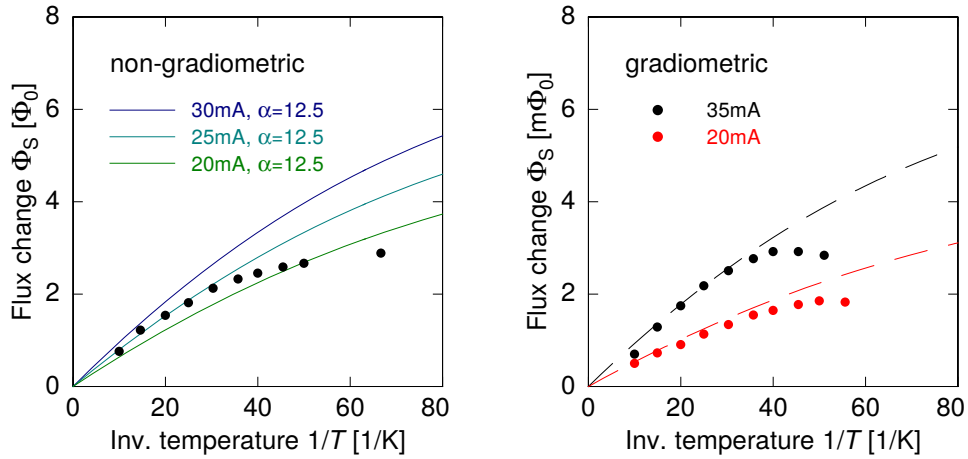
Figure 6.3: Left-hand side: Measured magnetization for the non-gradiometric detector of the *maXs30* detector array with a field-generating current of around 25 mA. Superimposed is the expectation for different currents for a detector with an asymmetry of 18 %. **Right-hand side:** Measured magnetization for a gradiometric detector for two different nominal field-generating currents and expected behaviour for a detector with an asymmetry of 1.5×10^{-4}.

It can be either due to the meander-shaped pick-up coil or due to a difference of the sensor volumes or their Er^{3+} concentration. Such variations in the microfabricated structure are of course likely to be different for each detector and, therefore, a single magnetization measurement can not be used to determine the field-generating current with a high precision for such a gradiometric detector. However, the observed scaling of the magnetization curve with the nominal current suggests that the preparation of the provided current was indeed successful and that this detector allows for field-generating currents of at least up to 35 mA.

6.1.4 Signal height

Figure 6.4 depicts the signal height following the absorption of a K_α photon of the ^{55}Fe calibration source for a nominal field-generating current of 50 mA in dependence of the temperature of the mixing chamber platform. This measurement was taken with a pixel of the non-gradiometric detector in parallel to the magnetization measurement discussed in section 6.1.3. Superimposed are the expected signal heights for an absorber with a thickness of 7 μm and a sensor made of Ag:Er. Different interaction parameters between $\alpha = 10$ and $\alpha = 15$ and field-generating currents from 20 mA to 30 mA were taken into account. Again a very good agreement is given for $\alpha = 12.5$ and a current of 25 mA with a perfect agreement down to temperatures of 30 mK, while at lower temperatures a decoupling from the bath temperature is
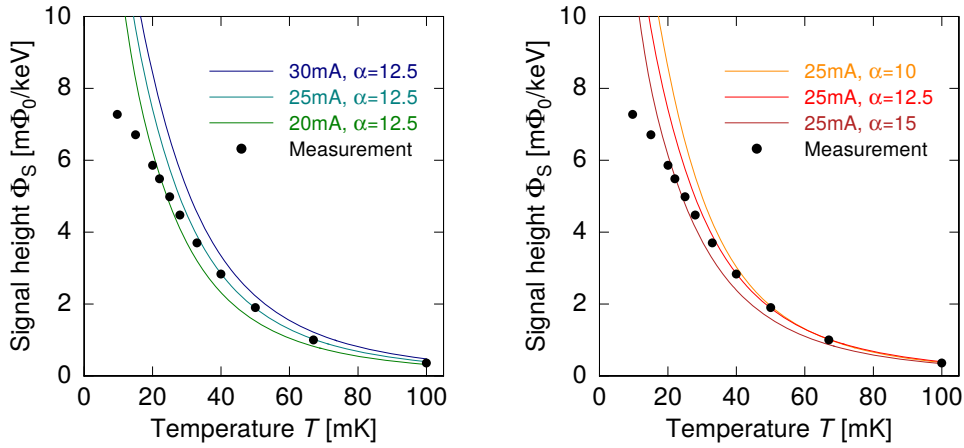
Figure 6.4: Signal height of a *maXs30* detector with an absorber thickness of 7 µm for a field-generating current of around 25 mA. Superimposed are simulations for an interaction parameter $\alpha = 12.5$ and different field-generating currents **(left)** and for a field-generating current of 25 mA for different interaction parameters α **(right)**.

observed. Together with the magnetization measurement shown in section 6.1.3 this measurement encourages the use of $\alpha = 12.5$ for the following analyses of the *maXs30* detector array.

6.1.5 Signal rise

To investigate the signal rise, measurements with very short time windows were performed on few individual pixels of the *maXs30* detector. Thereby about 500 samples could be acquired within the signal rise resulting in a very well defined signal shape. The left-hand side of figure 6.5 shows the first 10 µs of a single pulse after the absorption of a γ_{2-0} photon from an ^{241}Am source with an energy of about 59.5 keV at a nominal field generating current of 20 mA and a temperature at the end of the copper arm of about 16 mK. According to the associated signal height the detector itself probably has a slightly higher temperature of about 24 mK. The very small noise level during this measurment allows to avoid averaging several signals and thereby distorting the actual signal shape. A pure single exponential rise as it would be expected from the simple thermodynamic model shown in section 3.5.1 and expressed in equation 3.35 is superimposed in green and can not fully describe the measured behaviour. However, the measured data can be perfectly described by the fit function

$$A(t) = \Theta(t - t_0) A \left(e^{-(t-t_0)/\tau_d} - a_1 e^{-(t-t_0)/\tau_1} - a_2 e^{-(t-t_0)/\tau_2} \right) \tag{6.4}$$

that is shown in red. Here, A denotes the overall amplitude and t_0 an offset to account for the time difference between the actual start of the signal and the trigger time. The signal rise is described by the sum of two exponentials with time constants τ_1 and τ_2 and relative amplitudes a_1 and a_2, where $a_1 + a_2 = 1$. Possible explanations for these two contributions to the signal rise are discussed further below. On these short time scales the signal decay can be approximated with a single exponential decay with time constant τ_{d}.
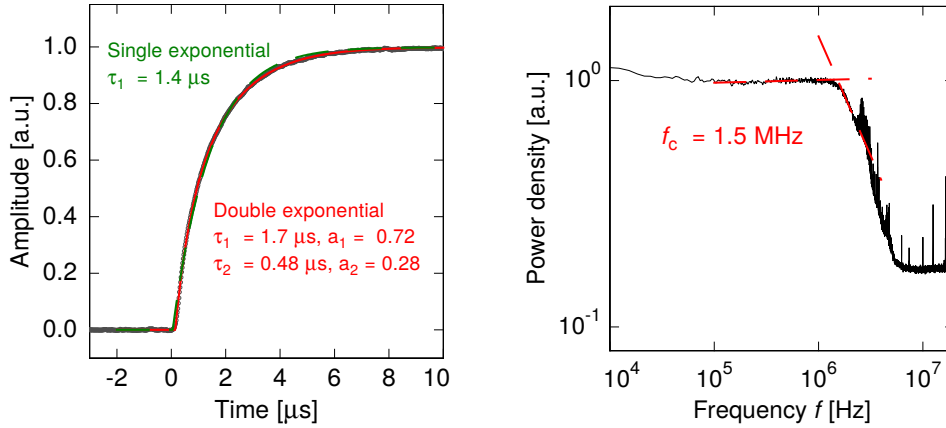

Figure 6.5: Left-hand side: Close-up of the first $10\,\mu s$ of a single pulse after the absorption of a γ_{2-0} photon from an ^{241}Am source at a nominal field generating current of $20\,\mathrm{mA}$ and a temperature of about $24\,\mathrm{mK}$. Superimposed are numerical fits in green and red according to different models of the signal rise described in the text. **Right-hand side:** Accompanying noise measurement showing a cut-off frequency of the SQUID read-out of about $1.5\,\mathrm{MHz}$, corresponding to a time constant of about $100\,\mathrm{ns}$.

The right-hand side of figure 6.5 depicts a noise spectrum that was recorded with the same acquisition settings as the signals. In the shown frequency range the dominating noise contribution is due to the white noise of the SQUID current sensor (ref. figure 4.1). At a frequency of about $f_{\mathrm{c}} = 1.5\,\mathrm{MHz}$ a cut-off can be seen due to a low-pass filter that was used during the acquisition. This frequency – and therefore the effective time resolution of the measurement – corresponds to a time constant of $\tau = 1/(2\pi f_{\mathrm{c}}) \approx 100\,\mathrm{ns}$. Therefore, both observed rise times are not influenced by the finite bandwidth of the read-out circuit. Only the very small rounding off of the signal rise within the first $100\,\mathrm{ns}$ that is not perfectly described by the fit function can probably be attributed to this effect. Table 6.1 shows the fit parameters corresponding to the signal rise of two pixels at two different energies of the absorbed photon. As expected no dependence of the signal shape on the energy of the absorbed photon was observed and the parameters are quite homogeneous throughout both investigated pixels. In the following, both contributions to the signal rise are

discussed in further detail.

	τ_1 [µs]	a_1	τ_2 [µs]	a_2
Pixel 1, γ_{2-0}	1.7	0.69	0.5	0.31
Pixel 1, γ_{2-1}	1.7	0.71	0.4	0.29
Pixel 2, γ_{2-0}	1.7	0.72	0.5	0.28
Pixel 2, γ_{2-1}	1.8	0.65	0.6	0.35

Table 6.1: Fit parameters according to equation 6.4 for two different pixels of the *maXs30* detector array at a working temperature of 24 mK after the absorption of photons with energies of 59.5 keV (γ_{2-0}) and 26.3 keV (γ_{2-1}), respectively.

Dominant rise time   The dominant contribution to the signal rise with a time constant of about 1.7 µs can be attributed to the thermal bottleneck between stems and sensor that is used to slow down the rise time artificially. It is faster than the design value of 3 µs which can be explained by several effects that are discussed in the following. One reason is the increased thermal conductivity of the new sensor material Ag:Er that was used to fabricate the sensor and the thermal bottleneck between absorber and sensor that limits the rise time. Compared to Au:Er a slightly larger residual resistivity ratio of $RRR = 2.4$ was achieved during the sputter deposition of the sensor, corresponding to a decreased number of lattice defects.
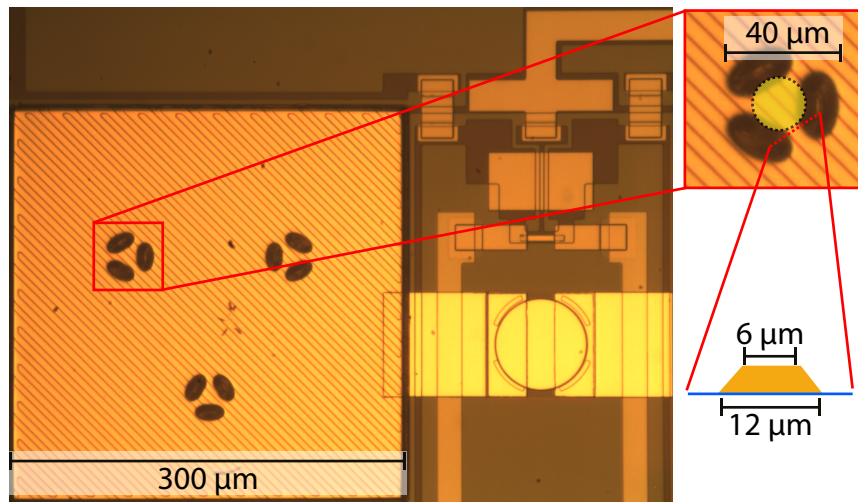

Figure 6.6: Photographic image and schematic detail of the thermal bottlenecks between the stems and the temperature sensor limiting the signal rise time. The close-up picture also indicates the contour of the contact area of one stem.

Furthermore, a photograph of the thermal bottleneck that can be seen in detail in figure 6.6 reveals small deviations from the intended geometry due to an undercut in the thick photoresist that was used to fabricate the sensor layer. From the photograph a length $l = 8\,\mu\text{m}$ and a cross-sectional area $A = 0.5 \times (6\,\mu\text{m} + 12\,\mu\text{m}) \times 3.5\,\mu\text{m}$ of the $3.5\,\mu\text{m}$ thick layer can be deduced. With $n = 3 \times 3$ thermal links per absorber and an electric resistivity of $\rho_{\underline{\text{Ag}}:\text{Er}} = \rho_{\underline{\text{Ag}}:\text{Er}}^{300\,\text{K}}/(RRR - 1) + 6.76 \times 10^{-8}\,\Omega\,\text{m} \times c = 1.14 \times 10^{-8}\,\Omega\,\text{m}$ for an Er^{3+} concentration of $c = 320\,\text{ppm}$ we get a total thermal conductivity

$$G = \frac{\mathcal{L}T}{\rho_{\underline{\text{Ag}}:\text{Er}}} n \frac{A}{l} = 1.43\,\mu\text{W/K} \tag{6.5}$$

according to the Wiedemann-Franz law for a temperature of $T = 24\,\text{mK}$ and a Lorenz number of $\mathcal{L} = 2.44 \times 10^{-8}\,\text{W}\,\Omega\,\text{K}^{-2}$. Therefore, a rise time of

$$\tau_1 = \frac{C_\text{a}C_\text{s}}{G(C_\text{a} + C_\text{s})} = 1.64\,\mu\text{s} \tag{6.6}$$

is expected which is slightly smaller than the observed time constant of about $1.7\,\mu\text{s}$. The observed deviations can for example be explained by slightly different dimensions of the thermal links. According to simulations based on section 3.3.6 with an interaction parameter $\alpha = 12.5$, a sensor heat capacity of $C_\text{s} = 11.0\,\text{pJ/K}$ at a temperature of $24\,\text{mK}$ and a field generating current of $20\,\text{mA}$ were assumed as well as an absorber thickness of $7\,\mu\text{m}$ that was determined in section 6.1.2 and results in an absorber heat capacity of $3.0\,\text{pJ/K}$.

Additional fast signal rise While the dominant rise time can be attributed to the artificial bottle neck between stems and sensor as discussed in the previous section, the additional fast rise with a time constant of about $0.5\,\mu\text{s}$ can not be explained in a simple way. A possible explanation might originate from the small sensor areas on which the stems are placed. These small areas thermalize together with the absorber and are, therefore, not affected by the thermal bottlenecks, thereby providing a rapidly increasing signal. In this case the associated time constant could be linked to the thermal diffusion inside the absorbers. Alltogether these areas account for $r = 1.1\,\%$ of the total sensor area. We can calculate the initial change $\Delta m'$ of the magnetic moment assuming a complete thermal equilibrium of absorber and these small sensor areas in relation to the overall change Δm after the thermalization of the absorber and the complete sensor. For the relative amplitude of the fast rise we

thereby get

$$a_2 = \frac{\Delta m'}{\Delta m} = r \frac{C_\mathrm{a} + C_\mathrm{s}}{C_\mathrm{a} + rC_\mathrm{s}} \ . \tag{6.7}$$

At the given experimental conditions a relative amplitude of $a_2 \approx 5\,\%$ would be expected which is much smaller than the observed $30\,\%$. For future detectors with a thicker absorber and, therefore, larger heat capacity C_e this effect should decrease further.

Another reason for the fast initial signal rise could be found in photoresist underneath the absorbers that might not have been dissolved completely and provides a direct contact between absorber and larger parts of the sensor. When removing some absorbers for the determination of their thickness as described in section 6.1.2 such remaining parts of photoresist were found beneath absorbers of a different chip from the same wafer.

6.1.6   Signal decay

For the investigated *maXs30* detectors the signal decay can not be described by a simple thermalization to a thermal bath, leading to a single exponential decay as shown in section 3.5.1. The reason for this is the relatively weak coupling between detectors and heat bath due to the missing through-wafer holes that would be filled with gold to provide a good thermal contact to the backside of the wafer. Therefore, at low temperatures the thermal coupling between the two pixels of a single detector is stronger than the coupling to the bath. As soon as both pixels of a perfectly gradiometric detector reach thermal equilibrium with each other, the signals of both pixels would compensate each other according to equation 3.31 and the resulting signal amplitude reaches zero. However, at this time both pixels are still warmer than the thermal bath, leading to a non-zero signal if the two pixels are not perfectly gradiometric. This expected behaviour is confirmed by the measurements that are shown in figure 6.7. The left-hand side depicts the signal decay of both pixels of a gradiometric detector channel of a *maXs30* detector array at a nominal temperature of $22\,\mathrm{mK}$. Several signals originating from the absorption of an ^{241}Am γ_{2-0} photon were averaged to increase the effective signal-to-noise ratio. Both pixels show a fast exponential relaxation down to zero within $5\,\mathrm{ms}$. The right-hand side shows the signal decay of the two pixels of the purposely non-gradiometric detector for the same operating parameters. These two pixels feature a fast exponential relaxation with a similar time constant, but for times above $4\,\mathrm{ms}$ they additionally show a slowly decaying offset due to the temperature of both pixels still being above the temperature of the heat bath.
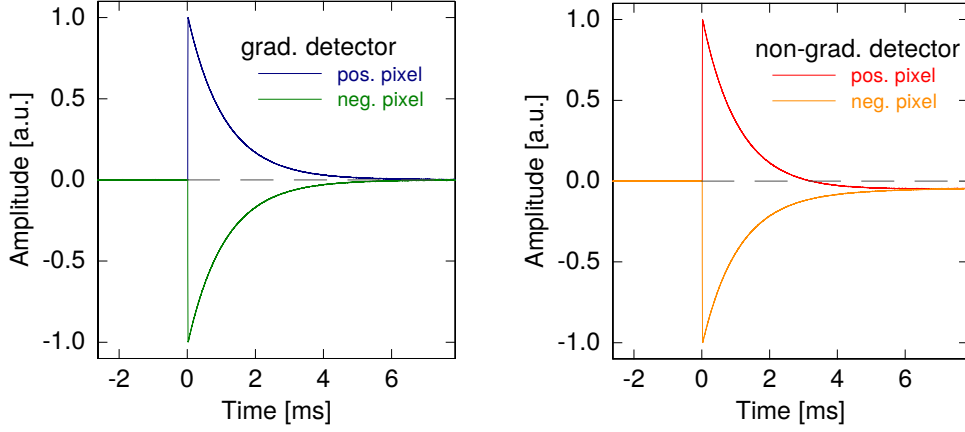
Figure 6.7: Signals of the two pixels of a gradiometric (**left**) as well as of the purposely non-gradiometric (**right**) detector channel at a nominal temperature of $22\,\mathrm{mK}$ and a nominal field-generating current of $30\,\mathrm{mA}$.

In future detectors featuring a complete through-wafer thermalization, the thermal contact to the bath should be larger than the one between the pixels and a complete fast thermalization is expected.

Thermal model and discussion of the time constants

Neglecting the thermalization to the bath we get a simple thermodynamic system of two pixels with heat capacities C_1 and C_2, connected by a thermal link with conductivity G_{pp}. Thus we can calculate the temperature changes $\Delta T_1(t)$ and $\Delta T_2(t)$ of both pixels after an energy input E into one of the two pixels and subsequently the total detector signal

$$\Delta\Phi(t) = \frac{\partial\Phi}{\partial T}\Delta T_1(t) - (1-\epsilon)\frac{\partial\Phi}{\partial T}\Delta T_2(t) \propto \Delta T_1(t) - (1-\epsilon)\Delta T_2(t) \tag{6.8}$$

where we introduced the parameter ϵ to take into account a possible asymmetry in the sensors of the detector. For the final signal after an energy input E we get

$$\Delta\Phi(t) = \frac{\partial\Phi}{\partial T}\frac{E}{C_1+C_2}\left(a_i e^{-t/\tau_{\mathrm{pp}}} + \epsilon\right) \tag{6.9}$$

with an amplitude

$$a_i = \begin{cases} (C_1+C_2-\epsilon C_1)/C_1 & \text{for absorption in pixel } i=1, \\ -(C_1+C_2-\epsilon C_1)/C_2 & \text{for absorption in pixel } i=2, \end{cases} \tag{6.10}$$

and a time constant

$$\tau_{\mathrm{pp}} = \frac{C_1 C_2}{G_{\mathrm{pp}}(C_1 + C_2)} \tag{6.11}$$

for the relaxation between the two pixels. For a perfect gradiometric detector with $\epsilon = 0$ the offset vanishes as expected, resulting in the simple single-exponential decay that can be observed on the left-hand side of figure 6.7.
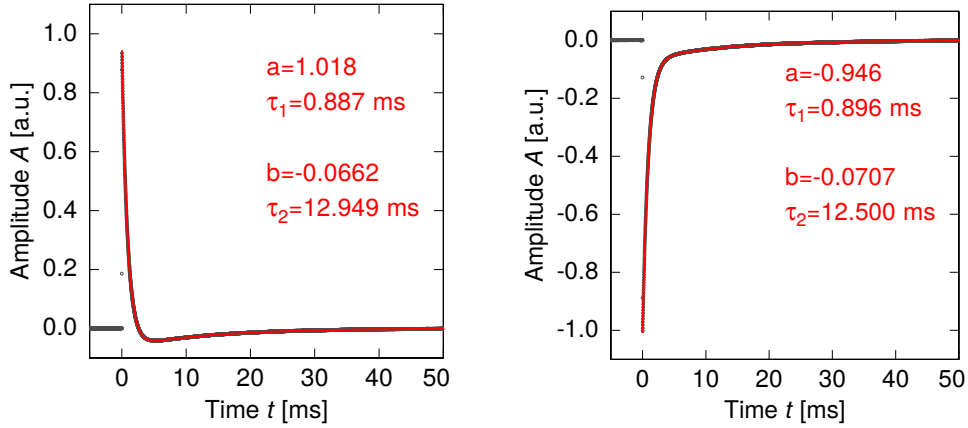

Figure 6.8: Signal decay in the positive **(left)** and in the negative **(right)** pixel of the purposely non-gradiometric detector. Superimposed in red are numerical fits according to equation 6.12.

Figure 6.8 depicts a longer time window of the signal decay after the absorption of a photon in both pixels of the non-gradiometric *maXs30* detector. The additional relaxation to the thermal bath results in an additional exponential decay and we can model the signal amplitude by

$$A(t) = a\mathrm{e}^{-t/\tau_1} + b\mathrm{e}^{-t/\tau_2} \;. \tag{6.12}$$

The data of both pixels are matched perfectly by this fit function. The fitting parameters of both pixels are shown in table 6.2 together with the corresponding parameters of the two pixels of a gradiometric detector.

As expected both time constants are in good agreement for every two pixels that belong to the same detector. For τ_1 even the difference between the gradiometric and the non-gradiometric detector is very small. The amplitudes a of both pixels of the gradiometric detector are also in very good agreement with each other as expected. Within the assumption of equation 6.10, for $\epsilon \approx 0$ the difference of both offsets relative to the amplitudes $|b_1/a_1 - b_2/a_2| \approx \epsilon$ is a measure for the asymmetry of the

	a [a.u.]	τ_1 [ms]	b [a.u.]	τ_2 [ms]
grad.; positive	1.071	0.871	-	-
grad.; negative	-1.077	0.881	-	-
non-grad.; positive	1.018	0.887	-0.0662	12.9
non-grad.; negative	-0.946	0.896	-0.0707	12.5

Table 6.2: Fit parameters according to equation 6.12 for four different pixels of the *maXs30* detector array.

detector. For the non-gradiometric detector, with $\epsilon = 0.18$ and a measured value of $|b_1/a_1 - b_2/a_2| = 0.14$, this is in good agreement with the observed behaviour.
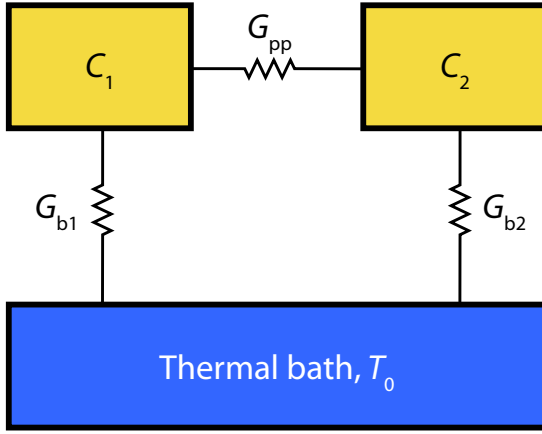

Figure 6.9: Thermal model of two single pixels with heat capacities C_1 and C_2 that are connected by a thermal link with conductivity G_{pp}. Both pixels are connected to a common heat bath by links with conductivities G_{b1} and G_{b2}, respectively.

Using the thermal model that is depicted in figure 6.9 and assuming $G_{\mathrm{b1}} \approx G_{\mathrm{b2}} =: G_{\mathrm{b}}$ and expressing the heat capacities as $C_1 =: C$ and $C_2 = (1 - \epsilon')C$, both involved time constants

$$\tau_{1/2} = \frac{2(1 - \epsilon')C}{(2 - \epsilon')(G_{\mathrm{b}} + G_{\mathrm{pp}}) \pm \sqrt{(2 - \epsilon')^2 G_{\mathrm{pp}}^2 + 2\epsilon'^2 G_{\mathrm{b}} G_{\mathrm{pp}} + \epsilon'^2 G_{\mathrm{b}}^2}} \tag{6.13}$$

can be calculated. Assuming a detector temperature of $33\,\mathrm{mK}$, a field-generating persistent current of $25\,\mathrm{mA}$ as well as an interaction parameter $\alpha = 12.5$, the total heat capacity of a *maXs30* pixel with a $7\,\mathrm{\mu m}$ thick absorber is about $C_1 = 13.2\,\mathrm{pJ/K}$, while the second pixel of the non-gradiometric detector has a heat capacity of $C_2 = 11.6\,\mathrm{pJ/K}$, corresponding to a parameter $\epsilon' = 0.12$. The thermal link between both pixels of a non-gradiometric detector is made of gold, has an effective length of $205\,\mathrm{\mu m}$ and a cross-sectional area of $80\,\mathrm{\mu m} \times 0.3\,\mathrm{\mu m}$ resulting in an electronic thermal conductivity of $G_{\mathrm{pp}} = 4.3\,\mathrm{nW/K}$ according to the Wiedemann-Franz law for a residual resistivity ratio of $RRR = 2.1$. The thermalization process to

the thermal bath can be identified with the thermal diffusion from the sensor to the substrate of the detector chip. For a rough estimate of the expected time constant of this process a thermal boundary resistance R_{tb} leading to a thermal conductivity of

$$G_b = \frac{1}{R_{tb}} A T^3 \tag{6.14}$$

is assumed, where $A = 300\,\mu\text{m} \times 300\,\mu\text{m}$ denotes the area of a temperature sensor. For a contact of silver to silicon a value of $R_{tb} \approx 13.5\,\text{K}^4\text{cm}^2/\text{W}$ has been calculated [Swa89] based on acoustic and diffuse mismatch models. With a temperature of $T = 33\,\text{mK}$ this corresponds to a thermal conductivity $G_b = 2.4\,\text{nW/K}$. According to equation 6.13 we, therefore, expect decay time constants of

$$\tau_{1/2} = \begin{cases} 1.1\,\text{ms} \\ 5.2\,\text{ms} \end{cases} \tag{6.15}$$

for the non-gradiometric detector. The expected time constant τ_1 is slightly larger than the measured value. The deviations can for example be explained by a slightly thicker thermalization layer or a deviating residual resistivity ratio RRR. The rather large deviation of τ_2, which is dominated by the thermal link to the bath, from the observed behaviour could result from the very rough assumption of a simple interface of silver and silicon. In reality an amorphous silicon oxide layer is present between the sensor made of Ag:Er and the silicon substrate and roughly $50\,\%$ of the boundary area is additionally covered by the pick-up coil made of niobium in between these materials. However, in previous developed detectors with a sensor made of Au:Er this rough approximation showed a good agreement with the observed behaviour [Sch12]. As the thermal conductivity associated with the thermal boundary resistance is highly temperature dependent, also a slightly reduced operating temperature could explain the longer decay times.

Additional fast decay due to nuclear quadrupole moments

One of the reasons to exchange the sensor material from Au:Er to Ag:Er is the additional fast decay that is described in section 3.3.5 and that is observed in detectors featuring a sensor made of Au:Er. The left-hand side of figure 6.10 depicts the signal decay of a *maXs200* detector with a sensor made of Au:Er, showing this fast initial decay with a time constant of $365\,\mu\text{s}$ and a relative amplitude of $37\,\%$. This decay is attributed to the redistribution of energy from the system of the Er^{3+} ions and the system of the conduction electrons into the system of nuclear quadrupole moments of gold.
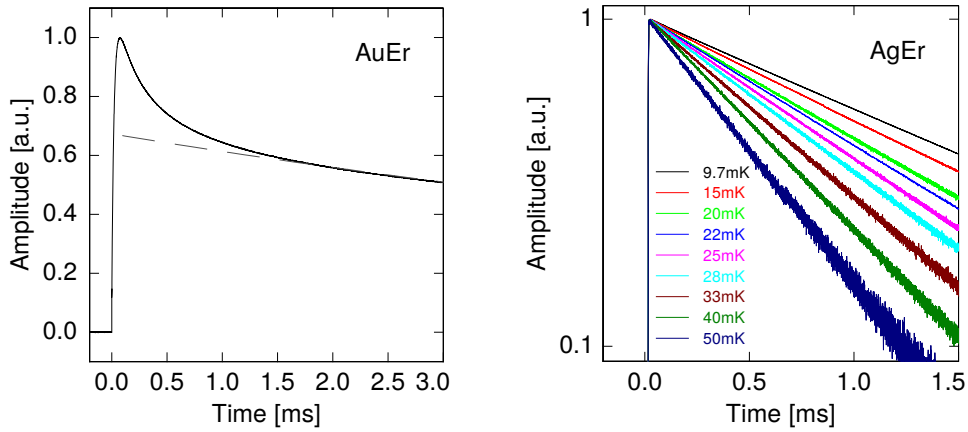
Figure 6.10: Left-hand side: Averaged pulse detected in a *maXs200* detector with a sensor made of Au:Er. Clearly visible is a fast additional decay with a time constant of 365 µs due to the nuclear quadrupole moments. The dashed grey line highlights the decay time to the thermal bath. **Right-hand side:** Logarithmic plot of averaged pulses detected in a *maXs30* detector with a sensor made of Ag:Er for different temperatures. The observed behaviour corresponds to a purely single-exponential decay.

With a nuclear spin of 1/2 the host material silver does not show this additional heat capacity and, therefore, the *maXs30* detectors with a sensor made of Ag:Er should not suffer from this fast decay. The right-hand side of figure 6.10 depicts the decay of averaged pulses after the absorption of photons with an energy of 6 keV in a gradiometric *maXs30* detector for different temperatures. The latter were measured at the mixing chamber platform and range from 9.7 mK to 50 mK. In the logarithmic plot the decay exhibits a perfectly linear behaviour for all temperatures and no additional term due to a nuclear heat capacity can be observed.

6.1.7 Crosstalk

A very important aspect in large detector arrays is thermal and electromagnetic crosstalk between different detectors of the same array that could limit the energy resolution or the achievable count rate of the whole array. To investigate this effect a detector of the *maXs30* array was irradiated with an ^{241}Am source and for every triggered event also the signal in an adjacent detector channel was recorded additionally. Figure 6.11 shows the resulting crosstalk signal in the adjacent detector in red after averaging over several signals that were coincident with a γ_{2-0} photon with an energy of 59.5 keV in the irradiated detector. For comparison a signal after a direct impact of a γ_{2-0} photon in the same detector is also shown in black. Only after additional smoothing, a signal-like structure can be seen from the crosstalk.
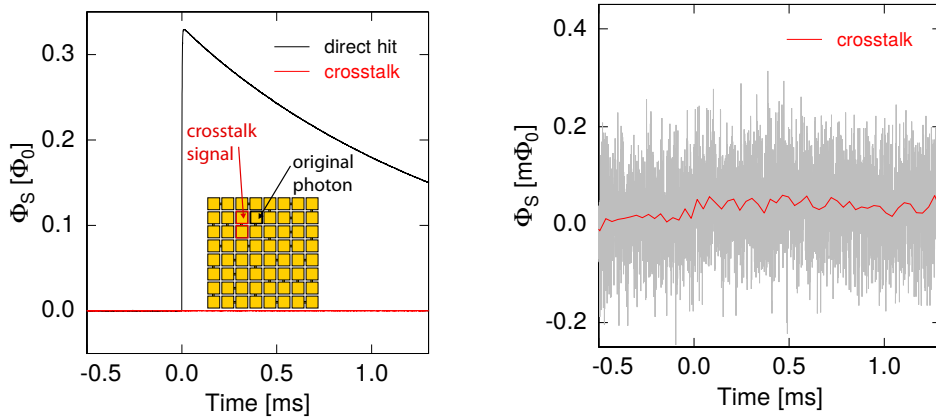
Figure 6.11: Averaged crosstalk signal in comparison with the signal originating from a direct impact (**left**) and close-up of the crosstalk signal on a roughly 500 times enlarged scale (**right**). The schematic drawing indicates the individual detectors that were involved in the measurement of the crosstalk. The close-up view shows the original averaged crosstalk signal in grey and the same signal after additional smoothing in red.

Its amplitude of about $0.04\,\mathrm{m}\Phi_0$ represents an upper limit of the crosstalk and is a factor of 8000 smaller than for a direct hit in this detector. Therefore, the crosstalk could be significantly reduced by at least one order of magnitude compared to earlier one-dimensional detector arrays of our group [Pie12, Sch12], most likely due to the higher symmetry of the individual detectors.

6.1.8   Linearity

In equation 3.3 the signal height of a magnetic calorimeter was approximated as being directly proportional to the energy input. However, as both key properties of the detector – the total heat capacity C_{tot} and the temperature dependence $\partial M/\partial T$ of the magnetization – depend on the detector temperature, these parameters change during a signal with the changing temperature. For larger photon energies E this typically leads to a reduced signal height compared to an extrapolation from smaller photon energies. At a working temperature of $20\,\mathrm{mK}$ a *maXs30* detector for example exhibits a temperature change of the order of $1\,\mathrm{mK}$ after the absorption of a $60\,\mathrm{keV}$ photon which already has a noticeable effect on the detector parameters. As shown in several works this non-linearity can very well be described with a simple quadratic term [Bat16]. Assuming such a simple quadratic energy dependence, one can describe

the signal amplitude by

$$A(E) = aE + bE^2 \propto E\left(1 - \frac{E}{E^*}\right) \tag{6.16}$$

with the two coefficients a and b. The relative non-linearity can be described with the single parameter $E^* = -a/b$.
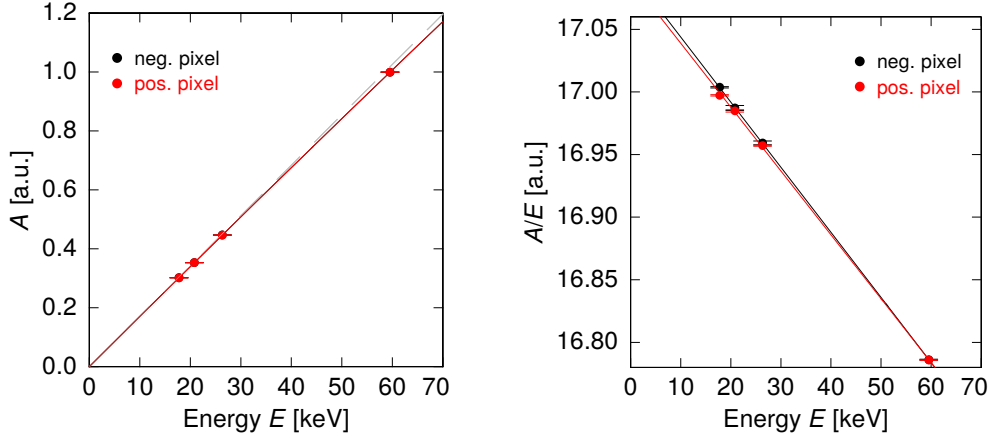

Figure 6.12: Signal amplitude A **(left)** and ratio A/E **(right)** of the amplitude and the energy of an absorbed photon in dependence of the photon energy E for two different pixels of the *maXs30* detector. Superimposed are fits based on equation 6.16.

The left-hand side of figure 6.12 shows the measured signal amplitude in dependence of the photon energy E for the two pixels of a *maXs30* detector. Due to the high conformity of both pixels only the data of the positive pixel is visible. The data is shown for the most dominant lines of the ^{241}Am calibration source, however, the $L\alpha_1$ line was not included as it shows a satellite line at higher energies that deforms the line shape and that is not well documented in literature (ref. section 6.2.1). The amplitudes were normalized to the γ_{2-0} line around 59.5 keV and the literature values for the line energies were taken from [Bea67] and [Bé10]. The data only shows a small deviation from the perfectly linear behaviour that is superimposed in grey.

	a $[10^{-3}\,\mathrm{keV}^{-1}]$	b $[10^{-6}\,\mathrm{keV}^{-2}]$	E^* [MeV]
pos. pixel	17.0899 ± 0.0021	-5.101 ± 0.059	3.35 ± 0.04
neg. pixel	17.0959 ± 0.0006	-5.199 ± 0.016	3.29 ± 0.01

Table 6.3: Resulting parameters of a quadratic fit of the non-linearity of two *maXs30* pixels.

The right-hand side of figure 6.12 depicts the ratio A/E as well as a linear fit according to equation 6.16. A very good agreement with a quadratic behaviour can be observed. As expected, the slope of the linear fit, represented by the parameter b is negative, corresponding to a relative signal amplitude that decreases for larger energies. Table 6.3 lists the resulting parameters from the numerical fits for these two pixels, while a comparison including more pixels is given in section 6.1.10. To derive a theoretical value for the non-linearity one can perform a Taylor expansion of the magnetic flux $\Delta\Phi_{\mathrm{S}}(E) = \Delta\Phi_{\mathrm{S}}(T(E))$ in the SQUID. In second order we derive the magnetic flux change

$$\Delta\Phi_{\mathrm{S}}(E) = \left.\frac{\partial\Phi_{\mathrm{S}}}{\partial E}\right|_{E=0} E + \frac{1}{2}\left.\frac{\partial^2\Phi_{\mathrm{S}}}{\partial E^2}\right|_{E=0} E^2 \tag{6.17}$$

after the absorption of a photon with energy E. In agreement with equation 3.3 the first-order term is given by

$$\left.\frac{\partial\Phi_{\mathrm{S}}}{\partial E}\right|_{E=0} E = \frac{1}{C_0}\left.\frac{\partial\Phi_{\mathrm{S}}}{\partial T}\right|_{T_0} E \tag{6.18}$$

with the total heat capacity $C_0 = C(T_0)$ of the detector at the base temperature T_0. The second order can be calculated to be

$$\frac{1}{2}\left.\frac{\partial^2\Phi_{\mathrm{S}}}{\partial E^2}\right|_{E=0} E^2 = \frac{1}{2}\left(\frac{1}{C_0}\left.\left(\frac{\partial}{\partial T}\frac{\partial\Phi_{\mathrm{S}}}{\partial E}\right)\right|_{E=0} - \frac{1}{C_0^2}\left.\frac{\partial\Phi_{\mathrm{S}}}{\partial E}\right|_{E=0}\left.\frac{\partial C}{\partial T}\right|_{T_0}\right) E^2 \ . \tag{6.19}$$

With a field-generating current of $25\,\mathrm{mA}$ and a *maXs30* detector with an absorber height of $7\,\mathrm{\mu m}$, a temperature of $T_0 \approx 32\,\mathrm{mK}$ is needed to explain the first-order term of the discussed measurement. This rather high temperature seems plausible as in this measurement 20 two-stage SQUID sensors were operated simultaneously which even had a significant influence on the temperature of the side arm of the cryostat. With this conditions the simulation yields a signal height of $\partial\Phi_{\mathrm{S}}/\partial E = 4.20\,\mathrm{\mu\Phi_0/eV}$ with a temperature dependence of $\partial^2\Phi_{\mathrm{S}}/\partial T\partial E = -198\,\mathrm{\mu\Phi_0/eVK}$ and a total heat capacity of $C_0 = 13.25\,\mathrm{pJ/K}$ with a temperature dependence $\partial C/\partial T = -70.0\,\mathrm{pJ/K^2}$. Together this corresponds to a non-linearity parameter $E^* = 3.96\,\mathrm{MeV}$ which is somewhat higher than the experimental value of $E^* \approx 3.3\,\mathrm{MeV}$ as it is shown in table 6.3. Possible reasons for the deviation could primarily be found in slightly different operating conditions.

Higher-order corrections   Figure 6.13 depicts the residuals after the quadratic correction of the non-linearity. The deviations are smaller than $3\,\mathrm{eV}$ and thereby

demonstrate a very good agreement of the data points with the literature values. The error bars include the amplitude error as well as errors of the literature energies ranging from 0.1 eV to 0.5 eV but no error due to the correction of the non-linearity.
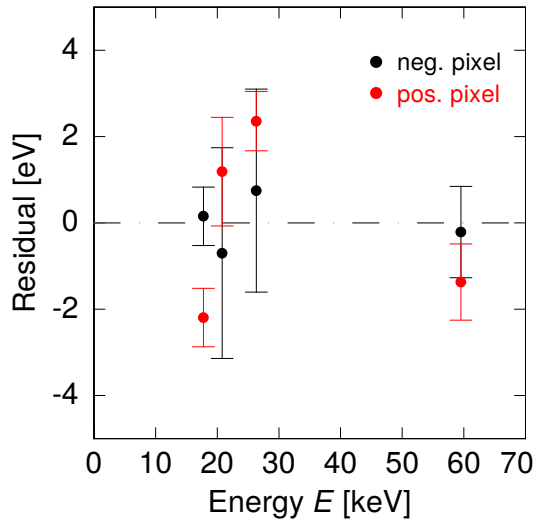

Figure 6.13: Residual energy difference after converting the measured signal amplitudes into energy.

While this quadratic non-linearity shows an excellent agreement with the negative pixel shown in black, the positive pixel shows a small but significant deviation for the $L\beta_1$ X-ray line at an energy of 17.8 keV as well as the γ_{2-1} line around 26.3 keV. This hints to higher order corrections that might be necessary. However, for a conclusive analysis of this behaviour more statistics and smaller uncertainties in the line energies would be needed. With the available data the origin of this possible contribution to the non-linearity remains unclear. It might also not originate from the detector itself but might be part of the read-out system.

6.1.9   Intrinsic energy resolution

Together with the linearity and the active detection area, the energy resolution is one of the key features of an X-ray detector. In this section the intrinsic energy resolution that was achieved with the *maXs30* detector within the framework of this thesis is discussed. The left-hand side of figure 6.14 depicts the γ_{2-0} line of the ^{241}Am source at an energy of 59.5 keV measured with a gradiometric detector. The data was taken at a temperature of 15.7 mK, measured at the end of the side arm and with a nominal field-generating persistent current of 35 mA and processed with the optimal filter algorithm mentioned in section 5.2.2. Superimposed in red is a Gaussian fit with a full width at half maximum of $\Delta E_{\mathrm{FWHM}} = 44$ eV describing the line-broadening of the detector. Being a nuclear transition, the natural width of the line can be neglected.
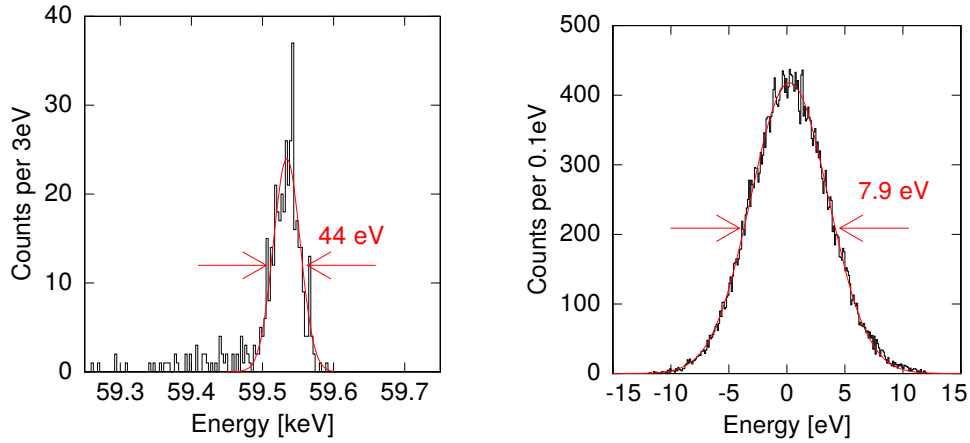
Figure 6.14: Histogram of the ^{241}Am γ_{2-0} line at $59.5\,\text{keV}$ **(left)** and baseline histogram **(right)**, measured with a *maXs30* detector with a nominal persistent current of $35\,\text{mA}$ at a nominal temperature of $15.7\,\text{mK}$. Superimposed in red are normal distributions with the specified full widths at half maximum.

This line broadening is much larger than expected for the operating parameters mentioned above. However, the width of X-ray or γ-lines is also prone to other effects, notably temperature variations of the detector chip that might not be properly corrected for in a gradiometric detector. Short time periods during which the bath temperature is increased more than the average variations could also cause the small low-energy tail. Consequently a better energy resolution of $20.3\,\text{eV}$ at $59.5\,\text{keV}$ was achieved in a non-gradiometric detector, even though that measurement suffered from a worse signal-to-noise ratio. This result and the associated high-resolution spectrum of the ^{241}Am source is discussed in section 6.2.1. As the intrinsic energy resolution of a magnetic calorimeter is almost energy-independent and is not influenced by temperature fluctuations, it is beneficial for the discussion of the energy resolution to record untriggered noise signals, so-called baselines, during the acquisition of the spectrum. Applying the same optimal filter, that is used for the actual triggered pulses, to these noise signals results in a baseline histogram that is depicted on the right-hand side of figure 6.14. The corresponding intrinsic energy resolution of $\Delta E_{\text{FWHM}} = 7.87\,\text{eV}$ mainly depends on the noise level and on the signal height, which are discussed separately in the following.

Noise   Figure 6.15 shows the measured spectral noise density of the detector at base temperature in comparison with the expected noise contributions that are discussed in sections 3.5.2 and 4.1. To match the measured noise density, an adjustment of the white noise level of the SQUID read-out to a value of $0.25\,\mu\Phi_0/\sqrt{\text{Hz}}$ is necessary. Additionally, the contribution of the magnetic moments of the Er^{3+} ions had to be

reduced to match the measurement in the range from 1 kHz to 10 kHz. This was done by an adjustment of the exponent $\zeta = 1$. However, further investigations of the different noise contributions and especially the noise density at lower frequencies would have to be done to derive precise values for the amplitude and the exponent of this contribution and to investigate possible influences of the host material silver.
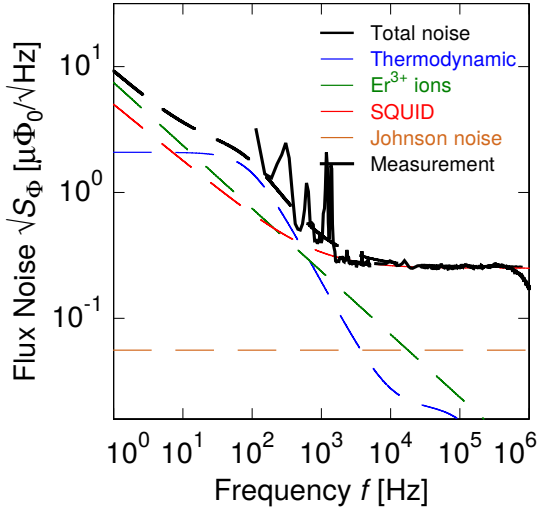

Figure 6.15: Measured spectral noise density of a *maXs30* detector at a nominal temperature of 15.7 mK in comparison with simulated noise contributions.

For the given operating conditions a signal decay time of 1.7 ms and a rise time of 1.3 µs were determined from signals of this measurement when approximating the signal rise with a single-exponential function. Taking into account these time constants, the measured noise level would allow for an expected energy resolution of 4.9 eV given the aforementioned operating temperature, persistent current and an interaction parameter of $\alpha = 12.5$.

Signal height   With the operating parameters given above and assuming a 7 µm thick gold absorber, a signal height of 11.8 mΦ_0/keV in the SQUID current sensor is expected based to the Ag:Er simulations with an interaction parameter $\alpha = 12.5$. The actually measured signal height of 7.51 mΦ_0/keV, however, is much smaller. Such a reduced signal height can be caused by several reasons. On the one hand, the temperature of the detector could deviate from the temperature of the copper side arm. Especially when many SQUID current sensors are operated simultaneously they might generate a substantial heat input to the detector chip which does not necessarily result in an increased arm temperature. In other experiments this effect was observed to lead to a drop in signal height of up to 50 %, depending on the number of operated SQUIDs and their operating currents. Although in the discussed measurement only one two-stage SQUID setup was operated, this shows that there might be a substantial decoupling between the detector and the bath temperature. In

future devices the thermal coupling between the detectors and the heat bath should be improved by the through-wafer thermalizations that are discussed in chapter 4. Additionally the development of SQUID setups with reduced power dissipation will help in reducing the heating effects. On the other hand, the field-generating persistent current itself can be smaller than the current that was injected during its preparation. A reason for this can be found in the chemical wet etching process that was used to etch the first niobium layer, resulting in an inhomogeneous and isotropic etching, that might lead to weak spots, thereby limiting the critical currents of the structures. The next generation of *maXs30* wafers are produced with a dry etching process resulting in better defined niobium structures. First test wafers were already measured to feature critical currents up to $100\,\mathrm{mA}$ at liquid helium temperatures which should allow the preparation of an optimal field-generating current. Due to the very good gradiometry of the detector a magnetization measurement as discussed in section 6.1.3 can not give a conclusive measurement of the persistent current and, therefore, the actual field-generating current can not be known precisely. The associated magnetization measurement that is shown on the right-hand side of figure 6.3, however, suggests that the nominal field-generating current of $35\,\mathrm{mA}$ was injected successfully. Other effects that could reduce the signal height can be found in an additional heat capacity of the detector, for example from remaining photoresist or other contaminations from the microfabrication processes, or in an inadequate theoretical description of the new sensor material $\underline{\mathrm{Ag}}$:Er, especially of the interaction parameter α. According to the simulations an operating temperature of $25.5\,\mathrm{mK}$ together with a field-generating current of $35\,\mathrm{mA}$ could explain the observed signal height. Given the measured reduced signal height and the measured noise the simulated energy resolution of $7.48\,\mathrm{eV}$ is in very good agreement with the measured intrinsic resolution of $7.87\,\mathrm{eV}$.

6.1.10   Chip homogeneity

For larger detector arrays the homogeneity across the detector chip is an important aspect as a higher homogeneity allows for easier detector operation and analysis of the data, especially when combining the spectra of different pixels. In the measurements that were performed in the framework of this thesis two individual *maXs30* detector chips of the same wafer were investigated at millikelvin temperatures. One of these two chips was read out with a full 32-channel read-out in two cool-downs, each time focusing on different aspects. As in both cases not all channels could be read out due to wiring problems or defective SQUID current sensors, measurements of both cool-downs were combined where possible to increase the coverage of the array. Taken both runs together, 53 of the 64 pixes of the *maXs30* array were operated successfully and showed pulses with a significant signal height. In figure 6.16 these

pixels are marked in green. The remaining 11 pixels that only featured very small or no pulses at all are marked in orange or red, respectively. For the four pixels marked in red the reason for this could be found in visible defects during the microfabrication, like broken wiring or short-circuited microstrips. In the following the homogeneity of
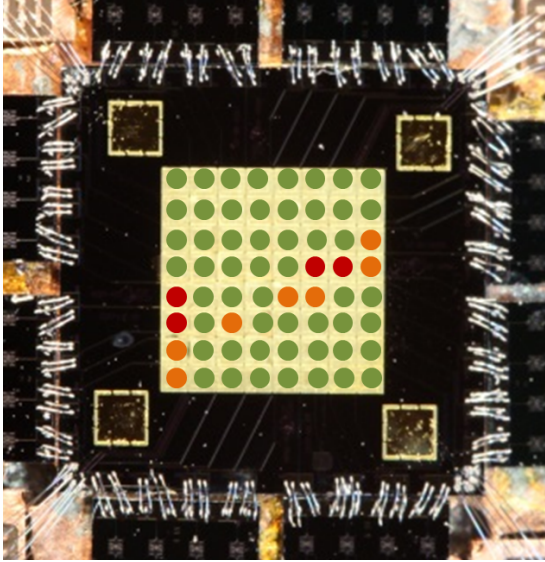

Figure 6.16: Overview of the detector chip *maXs30w1_09*, indicating pixels that showed pulses with a significant height in green. Pixels with visibly broken wiring are marked in red, while pixels without obvious defects that did not show pulses are marked in orange.

different parameters that characterize the individual detectors of a *maXs30* detector array is discussed. For this purpose the median values of the different parameter distributions give a good figure of merit and represent the typical values of the array. Unlike the average value the median value is less prone to outliers for example due to broken detectors. Accordingly the data is presented in so-called Tukey boxplots. This type of plots depicts the first ($Q1$) and third quartile ($Q3$) of a distribution as boundaries of a box, while the second quartile – or median – is shown as a vertical line within this box. Two horizontal lines extending from the box denote the position of the lowest and highest datapoint that lays within $1.5IQR$ of the lower or upper quartile, respectively. Here, $IQR = Q3 - Q1$ denotes the interquartile range that includes the inner $50\,\%$ of the data. Additional outliers are depicted as small dots. Displaying the data in such a way also gives an easy access to the skewness of the data that is represented as an asymmetry of the box with respect to the median value.

Meander inductance Figure 6.17 shows the boxplot of the inductances of 25 individual detector channels of the investigated chip. The determination of the individual meander inductances was done as described in section 6.1.1. The expected inductance of the microstrip depends on the length of the read-out lines and varies between $19\,\mathrm{pH}$ and $46\,\mathrm{pH}$. To facilitate the analysis a microstrip inductance of $35\,\mathrm{pH}$ was assumed for all detectors leading to a negligible error of up to $30\,\mathrm{pH}$ for the
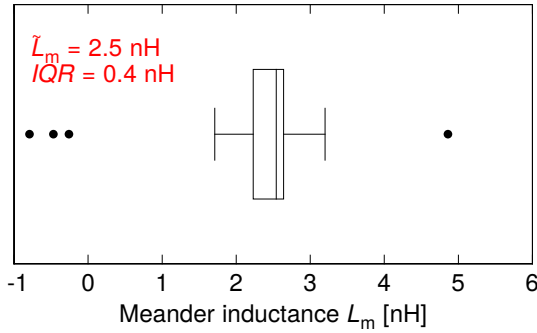
Figure 6.17: Measured inductances of 25 detectors of a *maXs30* detector array.

calculated detector inductance. A median of $\tilde{L}_{\mathrm{m}} = 2.54\,\mathrm{nH}$ with an IQR of $0.41\,\mathrm{nH}$ is calculated from the distribution. The median matches the expected inductance of $2.46\,\mathrm{nH}$ very well and with a spread of $16\,\%$ for the inner 13 detectors the fabrication homogeneity is satisfying. The negative skew can be explained by partially or completely shorted turns in one of the two meanders of each pick-up coil, leading to a slightly reduced inductance. Four significant outliers can be seen, corresponding to four detectors that could not be succesfully operated. The three outliers around $L_{\mathrm{m}} \approx 0\,\mathrm{nH}$ probably result from a shorted microstrip to the detector and maybe even feature a reduced inductance of the input coil of the SQUID, which could explain the negative values. The meander with an inductance of $L_{\mathrm{m}} = 4.9\,\mathrm{nH}$ probably is due to a detector were the pick-up coil of one of the two parallel meanders is broken. In this case the apparent inductance would be double the inductance of a single meander according to equation 6.3. Assuming one meander to be broken, the second would have an inductance of $2.5\,\mathrm{nH}$, thereby matching the other meanders of the array.

Absorber thickness   As discussed in section 6.1.2 the ratio $r = \eta_{26}/\eta_{60}$ of the absorption efficiencies of the two γ-lines at $26.3\,\mathrm{keV}$ and $59.5\,\mathrm{keV}$ of the $^{241}\mathrm{Am}$ calibration source is a good measure to compare the thicknesses of the absorbers of the *maXs30* detector array. Figure 6.18 shows a boxplot of this value including 19 pixels from chip *maXs30w1_09*. The small number of pixels that was included in this plot is due to the fact that only measurements were taken into account were no collimator was used and were the same radioactive source was used and directly placed in front on the X-ray window. Thus any distortion of the line intensities due to partial absorption by the collimator or the radiation shields is avoided. With a spread of only $3.8\,\%$ the thickness of the absorbers is very homogeneous due to the electroplating process that was used to fabricate the absorbers. In future this might even allow for very accurate intensity measurements without calibrating the absorber thickness of every single pixel individually.
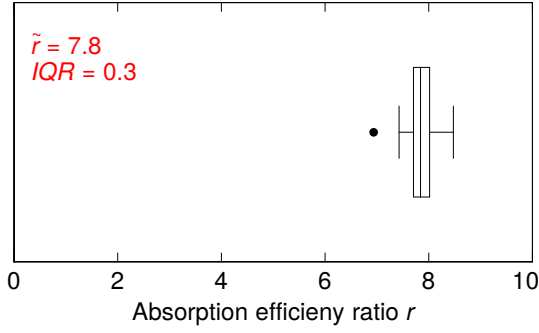
Figure 6.18: Ratio $r = \eta_{26}/\eta_{60}$ of the absorption efficiencies at $26.3\,\mathrm{keV}$ and $59.5\,\mathrm{keV}$ of 19 absorbers of a *maXs30* detector array.

Signal rise and decay time To determine the homogeneity of the signal rise and pixel-to-pixel relaxation times a fit of the function $A(t) \approx A(-\mathrm{e}^{-t/\tau_{\mathrm{r}}} + \mathrm{e}^{-t/\tau_{\mathrm{pp}}} + o)$ was performed on averaged pulses of 40 individual pixels. As the time resolution in this measurement did not allow for a high-resolution measurement of the signal rise as it was done in section 6.1.5, only a single-exponential rise was used. This is, however, sufficient for the purpose of comparing the dominant rise time of different pixels in this section. The decay was approximated based on the equation 6.12. With a mean
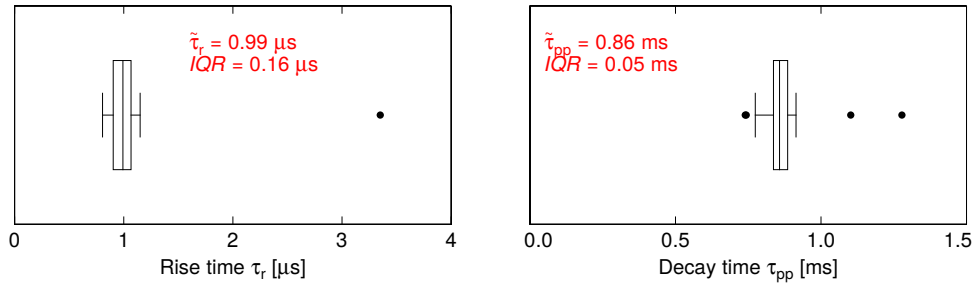

Figure 6.19: Boxplots of rise time τ_{r} (**left-hand side**) and pixel-to-pixel relaxation time τ_{pp} (**right-hand side**) of 40 pixels of a *maXs30* detector array.

value of $\tilde{\tau}_{\mathrm{r}} = 0.99\,\mathrm{\mu s}$ for the dominant rise time and $\tilde{\tau}_{\mathrm{pp}} = 0.86\,\mathrm{ms}$ for the pixel-to-pixel relaxation, both values are significantly faster than discussed in sections 6.1.5 and 6.1.6. This is most likely because of an elevated chip temperature due to heating effects of the 20 SQUIDs that were operated in this measurement. For the rise time the spread of $16\,\%$ is relatively large and also much larger than the spread of $5\,\%$ for the pixel-to-pixel relaxation time. A reason for this can be found in the structure sizes of the artifical bottleneck that slows down the signal rise which is much smaller than the thermal link between both pixels. Therefore, it is more prone to variations during microfabrication, eventually leading to a broader distribution of rise times. In the boxplot of the rise time there is one outlier at $\tau_{\mathrm{r}} \approx 3.4\,\mathrm{\mu s}$ and for the relaxation time two significant outliers at $\tau_{\mathrm{pp}} = 1.1\,\mathrm{ms}$ and $\tau_{\mathrm{pp}} = 1.3\,\mathrm{ms}$ can be seen. All three values belong to the two pixels of the same detector. By design it should be

perfectly gradiometric, however, the signal height of both pixels with respect to each other also differed by more than a factor of three in this measurement. Therefore, it is likely that the field generating persistent current in one of both meanders was greatly reduced, thereby affecting the themodynamical properties of the sensor and the whole detector.

Non-linearity   To investigate the homogeneity of the non-linearity of the detectors, figure 6.20 depicts the quadratic deviation from a perfectly linear detector response in form of the parameter E^* as discussed in section 6.1.8. Altough the spread of
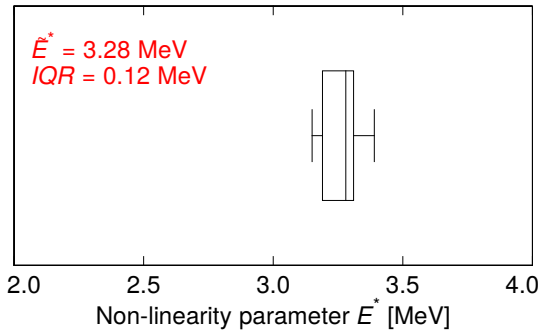

Figure 6.20: Deviation from a perfectly linear detector response of 10 pixels of the *maXs30* detector array expressed by the parameter E^* as introduced in section 6.1.8

only 3.7 % is very small on a relative scale, this corresponds to a deviation between the pixels of up to 40 eV at an energy of 60 keV. Therefore, for higher energies an individual non-linerity correction has to be applied to each single pixel when combining the spectra of different pixels.

Signal height   For the characterization of the detector array, the signal height is a better figure of merit than the energy resolution as the latter highly depends on the noise contributions of the read-out circuit. As many of the characterization measurements were performed without amplifier SQUIDs or with SQUIDs that showed a comparably high noise level, a comparability of the energy resolution would not be given in these cases. Figure 6.21 shows a boxplot of the signal height of 30 pix-
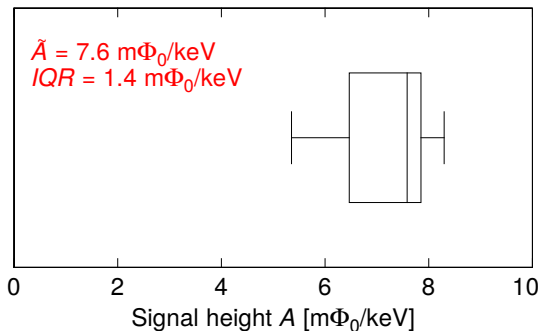

Figure 6.21: Measured signal heights of 30 pixels of a *maXs30* detector array with nominally the same temperature and field generating current.

els measured with an ^{55}Fe source at 5.89 keV. For a better comparability only pixels that were nominally operated with the same field-generating current and at the same working temperature are included. Furthermore, only the read-out SQUID of one channel was operated at a time to reduce heating effects by other SQUIDs. The median around 7.6 mΦ_0/keV would allow for energy resolutions of about 7.5 eV given a SQUID with appropriate noise performance as discussed in section 3.5.3. The data shows a relatively large negative skew, probably resulting from pixels that suffered a reduced field-generating current due to varying critical currents or local heating effects during the preparation of the persistent current. The spread in signal height of 18 % is quite large and demonstrates that an individual calibration of all pixels is necessary.

6.2   X-ray spectroscopy

In this section several energy spectra are discussed that were acquired and analysed in the framework of this thesis. The first section covers a spectrum of the ^{241}Am calibration source that was taken with the *maXs30* detector in one of our laboratories and focuses on the energy resolution. The remaining sections are dedicated to experiments that were performed at the heavy ion storage ring ESR with the *maXs200* detector as well as the *maXs30* detector array. In these sections special attention is given to the operation of the cryostat and the overall performance of a metallic calorimeter next to the storage ring, followed by a high-precision measurement of X-rays originating from interactions of highly charged Xe^{54+} ions with a Xe gas target. Finally a measurement with the two-dimensional *maXs30* detector array at the ESR is used to discuss the combining of individual spectra of several pixels in a measurement with low count rates and low X-ray energies.

6.2.1 ^{241}Am calibration source

During the characterization of the *maXs30* detector array several spectra of the ^{241}Am calibration source were taken. Figure 6.22 depicts the three most dominant γ-lines of this source after a cubic non-linearity correction based on the γ_{2-0} and γ_{2-1} transitions and the thee most dominant X-ray lines Lα_1, Lβ_1 and Lγ_1; literature values were taken from [Bé10, Des03]. Also shown is a baseline histogram that originates from untriggered noise signals as discussed in section 6.1.9. Superimposed in red is a purely Gaussian detector broadening. Due to a reduced signal-to-noise ratio the baseline resolution is slightly worse compared to the best intrinsic energy resolution of 7.9 eV that was achieved in the framework of this thesis. However, as this spectrum was taken with the purposely non-gradiometric detector, the
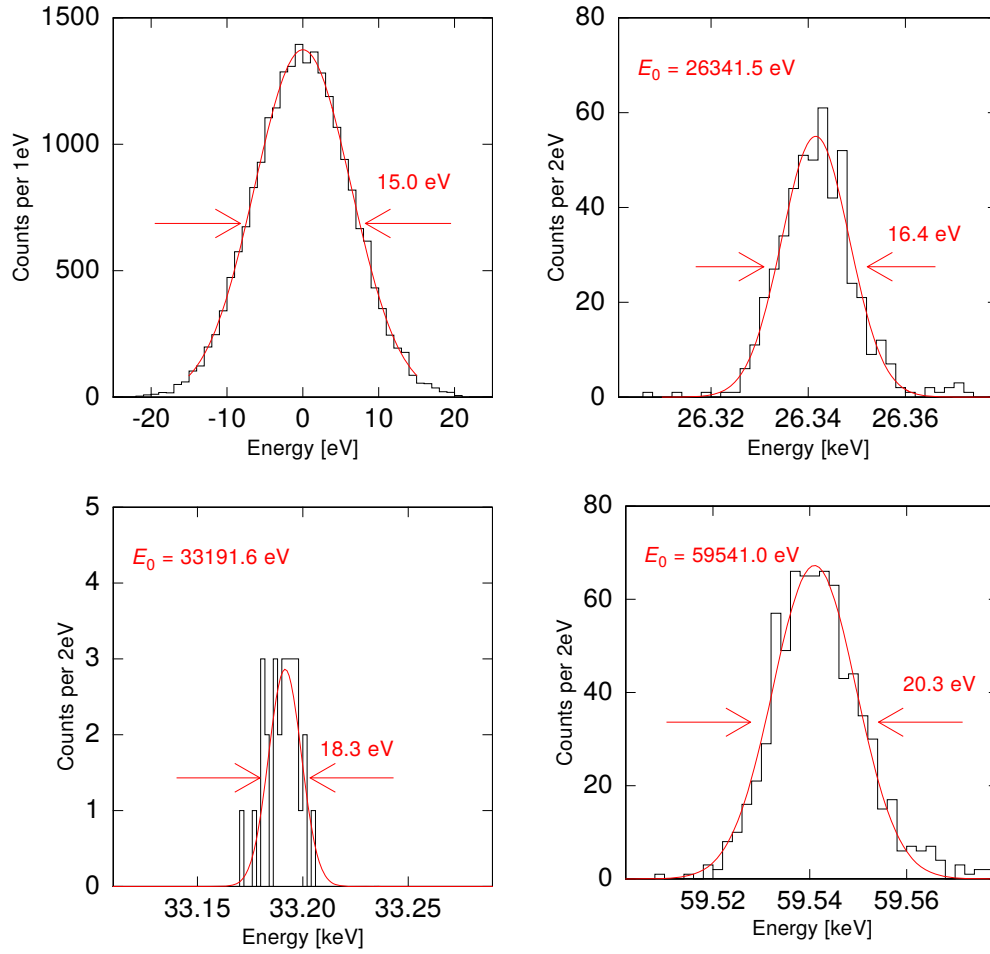
Figure 6.22: Intrinsic energy resolution (**top left**) and histograms of the γ_{2-1} (**top right**), γ_{1-0} (**bottom left**) and γ_{2-0} (**bottom right**) lines of an ^{241}Am source taken with a *maXs30* detector. Also depicted are Gaussian fits and the corresponding full widths at half maximum and the measured line centroids.

pretrigger-voltage before each pulse is proportional to the temperature of the detector. Therefore, the correlation between pretrigger-voltage and signal amplitude could be used to perform a correction of the signal height for each single pulse based on the detector temperature at the time of the pulse. The resulting energy resolution of $\Delta E_{\mathrm{FWHM}} = 20.3\,\mathrm{eV}$ at an energy of $E = 59.541\,\mathrm{keV}$ corresponds to a very good resolving power of $E/\Delta E_{\mathrm{FWHM}} = 2933$ which allows for high-resolution X-ray spectroscopy. Despite the temperature correction a small degradation of the energy resolution with the photon energy is observed which is larger than expected for metallic magnetic calorimeters. Most likely this is due to some remaining tempera-

ture variations on a 2×10^{-4} level that could not be corrected. Therefore, in future devices the asymmetry of the non-gradiometric detector will be slightly increased to enhance its sensitivity to the temperature of the detector chip.

Lα_1 satellite Figure 6.23 depicts a close-up of the Lα_1 and Lα_2 line of the ^{241}Am source. On the high-energy side of the dominant Lα_1 line a satellite can be identified. In previous measurements of the same source with the *maXs200* detector [Pie12] it was not visible but could be resolved in this measurement due to the better energy resolution.
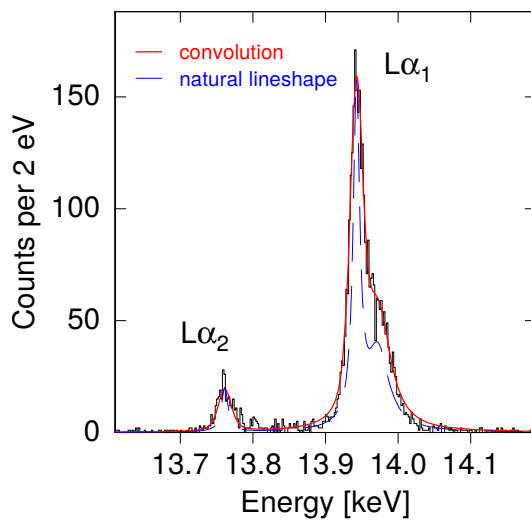

Figure 6.23: The Lα_1 and Lα_2 lines of ^{241}Am, detected with a *maXs30* detector. A satellite of the Lα_1 line can be seen towards higher energies.

Superimposed in red is a numerical fit of the spectrum based on the convolution of a Gaussian detector broadening with a full width at half maximum of 15.2 eV and a sum of three Lorentz distributions. The latter represent the natural lineshape according to $I(E) = I_0\gamma^2/(\gamma^2 + (E - E_0)^2)$ and their sum is superimposed in blue. For the numerical fit the natural linewidths $w = 2\gamma$ and relative intensities I_0 of the two main lines were fixed according to their literature values, while the energies of all three lines as well as the intrinsic width and the amplitude of the satellite line were varied. The parameters of the resulting convolution are listed in table 6.4, showing a good agreement between the resulting energies of the Lα_1 and Lα_2 lines and their literature values. Most likely the origin of the observed satellite can be found in possible additional vacancies in the electronic shell due to Coster Kronig transitions or shake-off processes. The additional vacancy changes the electronic structure and consequently the energy levels of the shells, leading to a modified transition energy. The increased width of the satellite hints that it might indeed be a blend of two or more different satellites.

Line	E_0 [eV]	E_{lit} [eV]	w [eV]	I_0 [a.u.]
Np Lα_2	13761.1	13759.8 ± 0.2	10.8	0.13
Np Lα_1	13942.7	13944.3 ± 0.2	10.8	1.00
Satellite	13972.2	-	36.6	0.24

Table 6.4: Parameters of the Lα_1 and Lα_2 lines and the Lα_1 satellite. Literature values for the energies were taken from [Des03]. The relative intensities and the natural linewidths of the Lα_1 and the Lα_2 line were taken from [Lép08] and were not varied during the numerical fit.

6.2.2   *maXs200*: First test at the GSI

The first measurement with a metallic magnetic calorimeter at a storage ring was performed in the framework of this thesis at the Experimental Storage Ring ESR (ref. section 5.4.3) at the GSI in Darmstadt [Kel14, Hen15]. It was performed with the *maXs200* detector that was introduced in section 5.3 in a distance of approximately 1.5 m to the internal gas jet target of the ESR, while Au^{76+} ions were colliding with gas jet targets of N$_2$ and Xe at a beam energy of 300 MeV/u. About 70 % of the total available measurement time could be used in a continuous, remote-controlled measurement over seven days without the need of accessing the cryostat. A large part of the unused time was due to problems with the cooling water supply of the GSI and thus even higher duty cycles can be achieved in future experiments. In this measurement, the good energy resolution and high linearity of the detector could not be demonstrated in a spectrum originating from highly charged ions as the count rate of X-rays from the Au^{76+} ions was to low. Nevertheless, the performance of the detector array in close vicinity to the storage ring could be tested. The left-hand side of figure 6.24 depicts the baseline resolution of the *maXs200* detector during its measurements at the ESR. The measured intrinsic energy resolution of 27 eV matches the expectations for the nominal field-generating current of 100 mA and a detector temperature of 17 mK and is currently the best energy resolution that was achieved with a *maXs200* detector. In particular, the energy resolution was even better than in a measurement of the same detector in our institute under comparable operating conditions. The right-hand side of figure 6.24 shows the corresponding baseline resolution of this measurement at a nominal temperature of 15 mK and with a nominal field-generating current of 110 mA. Therefore, it could be shown that metallic calorimeters can be operated next to the large magnetic fields of the storage ring without degradation of the energy resolution compared to a typical laboratory environment.
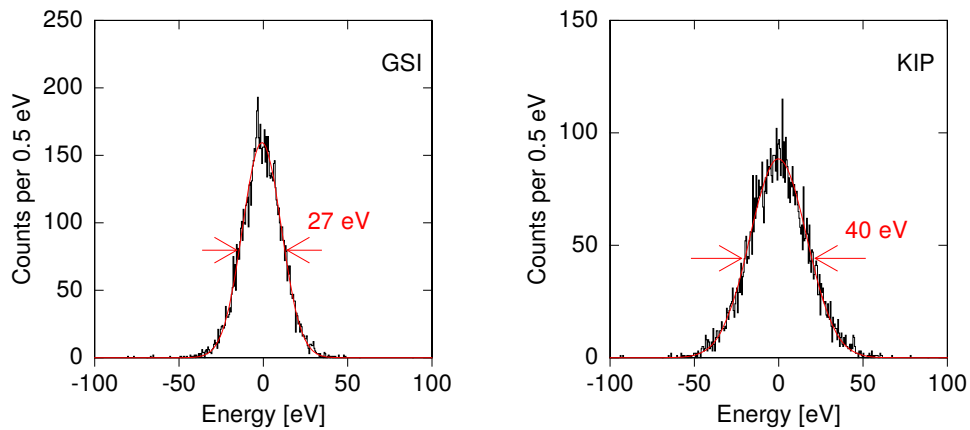
Figure 6.24: Left-hand side: Histogram of untriggered noise signals taken during the measurements at the ESR at the GSI. Superimposed in red is a Gaussian fit resulting in an energy resolution of 27 eV. **Right-hand side:** Measurement at our institute of the same detector under comparable operating conditions.

6.2.3 *maXs200*: Xe^{54+} on Xe gas target

In a second measurement campaign [Hen15] the *maXs200* detector was set up under a 60° angle with respect to the beam direction in a distance of 2 m to the interaction region of the gas target. The resulting X-ray spectrum of a beam of bare Xe^{54+} ions colliding with a Xe gas jet target at a beam energy of 50 MeV/u was measured within 48 h of measurement. To minimize the Doppler broadening, the *maXs200* detector chip was mounted such that the elongated absorbers were orientated vertically in order to minimize their effective width. For energy calibration an ^{241}Am calibration source was attached outside of the cryostat in between the detector and the gas target in such a way that the line of sight between them was not blocked by the source. The recorded data was fitted with an optimal filter algorithm described in [Fle03] and additional signal processing was done as developed and described in [Kel14] to account for variations in the signal shape of this special detector that arise most likely due to remaining photoresist between sensor and absorber or due to a position dependent thermalization within the absorber. Figure 6.25 shows the resulting spectrum of the measurement campaign in the energy range from 0 keV to 70 keV, recorded with two pixels and an effective detector area of 2 mm^2. Before combining the individual spectra of both pixels, an individual correction for non-linearity (ref. section 6.1.8) and for temperature variations was performed. The difference in Doppler shift of both pixels that have a center-to-center distance of 0.56 mm is expected to be less than 4 eV for X-rays with 40 keV energy and was therefore neglected as it is more than ten times smaller than the energy resolution of the detector in this measurement. Besides the lines that were used for the energy calibration (marked in red), additional lines
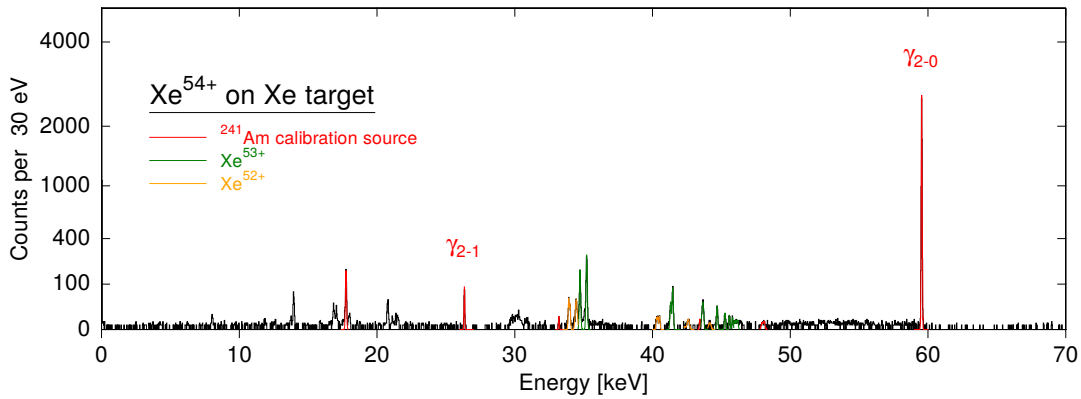
Figure 6.25: Overview over the X-ray spectrum taken with two pixels of a *maXs200* detector in the second measurement campaign at the ESR, where a bare Xe^{54+} ion beam at a beam energy of $50\,MeV/u$ was colliding with a Xe gas target. Lines from an ^{241}Am source that were used for the energy calibration are marked in red. Lines emitted from the highly charged ions are marked in green (hydrogen-like Xe^{53+}) and orange (helium-like Xe^{52+}). Below $25\,keV$ additional X-ray lines from the calibration source that were not used for the energy calibration, can be seen.

from the highly charged Xe ions can be seen marked in green (hydrogen-like Xe^{53+}) and orange (helium-like Xe^{52+}), demonstrating the large bandwidth of magnetic microcalorimeters. In the following sections the different constituents of the spectrum are discussed in more detail.

Energy calibration of the *maXs200* detector   A quadratic correction of the non-linearity of the detector response was performed individually for both pixels of the active detector, taking into account the $L\beta_1$ X-ray line and several γ-transitions (γ_{2-0}, γ_{1-0}, γ_{2-1}) of the ^{241}Am calibration source as described in section 6.1.8. Table 6.5 shows the resulting energies E_m of the γ-transitions after the final energy calibration. Two escape lines are listed additionally in the energy range of interest for the measurement of the transitions originating from the highly charged Xe ions. They originate from photons that are absorbed by the photoeffect, if one of the X-ray fluorescence photons, that are created after the absorption, leaves the detector. The agreement between the measured energies and the corresponding values taken from [Bé10] and [Bea67] is satisfying and suggests that any systematic errors due to a remaining non-linearity should be small. For a more precise verification of the quality of the energy calibration more statistics especially in the low-intensity lines γ_{1-0} and γ_{4-2} would be needed. Figure 6.26 shows the combined spectrum of both pixels of the two strongest γ-lines. These lines are suitable to discuss the energy reso-

Line	E_{m} [eV]	E_{lit} [eV]
Calibration source ^{241}Am		
γ_{2-1}	26343.4 ± 0.5	26344.6 ± 0.2
γ_{1-0}	33202 ± 2	33196.3 ± 0.3
γ_{4-2}	43438 ± 6	43420 ± 3
γ_{2-0}	59541.6 ± 0.3	59540.9 ± 0.1
Escape lines		
γ_{2-0} - Au Lβ_2	47955 ± 17	47959
γ_{2-0} - Au Lβ_1	48098 ± 11	48099

Table 6.5: Recorded energies E_{m} of the lines originating from the calibration source. The literature values E_{lit} for the γ-transitions of ^{241}Am are taken from [Bé10], while the X-ray energies of Au for the escape lines can be found in [Bea67]. The error of the measured data only includes statistical errors and no systematic errors due to a possibly remaining non-linearity.

lution as their natural linewidth is negligible compared to the detector broadening. The energy resolution shows a slight increase with energy from $\Delta E_{\mathrm{FWHM}} = 42\,\mathrm{eV}$
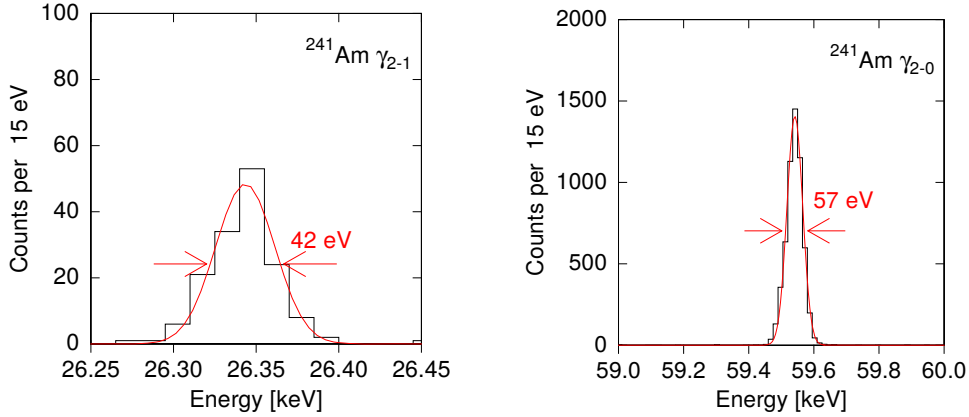
Figure 6.26: The γ_{2-1} **(left)** and γ_{2-0} **(right)** line of ^{241}Am, combined for both pixels. Superimposed in red is a gaussian fit indicating the detector broadening.

at $26.3\,\mathrm{keV}$ to $\Delta E_{\mathrm{FWHM}} = 57\,\mathrm{eV}$ at $59.5\,\mathrm{keV}$. Probably this is due to temperature fluctuations that were not fully corrected or due to a small remaining artifact of the signal shape variations which occured in all the measurements with this detector and which are discussed in detail in [Kel14]. Together with the baseline energy resolution of $\Delta E_{\mathrm{FWHM}} = 38.2\,\mathrm{eV}$ as derived from untriggered noise, this good energy resolution again shows that metallic magnetic calorimeters can be operated at the ESR without

significant negative effect on the detector performance if an appropriate shielding of the detector and the SQUID current sensors is done as shown in section 5.1.2.

Lyman series Ions of the bare Xe^{54+} ion beam may interact with the Xe gas target via (multiple) electron capture. The resulting excited hydrogen-like Xe^{53+} or helium-like Xe^{52+} ions deexcite by emitting characteristic radiation in the X-ray regime. With the given experimental setup only transitions to the ground state could be detected as Balmer radiation around 6 keV was suppressed by the air between gas jet target and cryostat by approximately 99 %. Figure 6.27 shows the part of the spectrum that was taken within 48 h containing all the lines originating from highly charged ions. The dominating part of the lines that do not originate from the calibra-
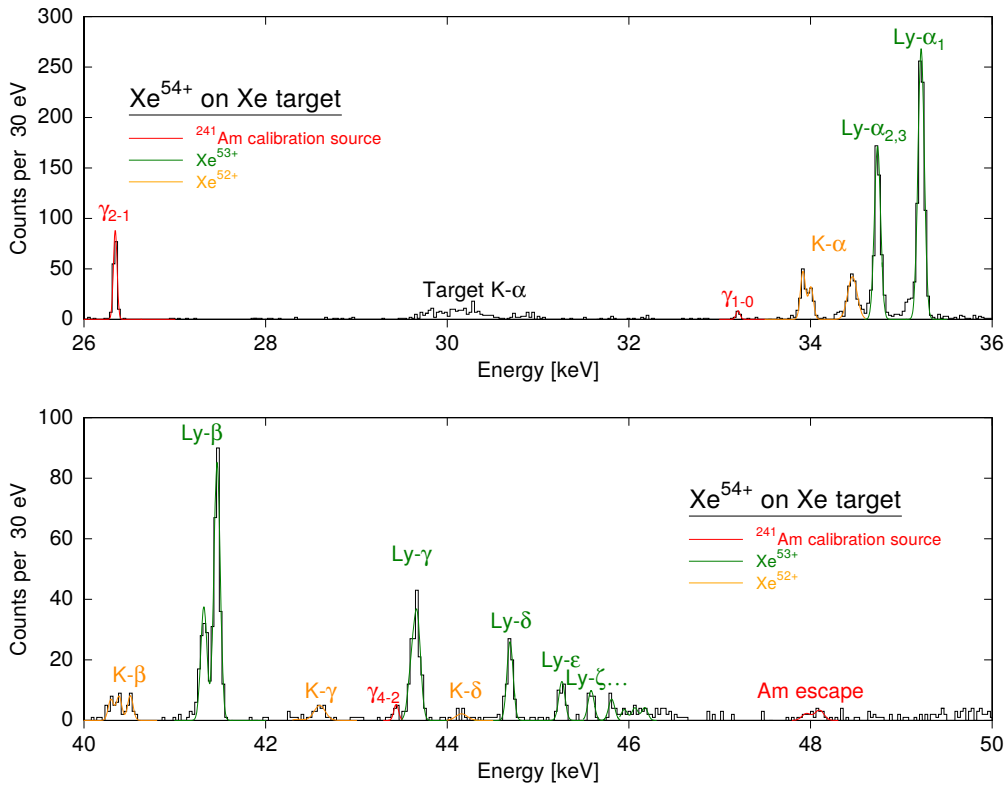
Figure 6.27: Spectrum of X-rays emitted from hydrogen-like Xe^{53+} (green) and helium-like Xe^{52+} (orange) after the collision of bare Xe^{54+} ions with a Xe gas target. Also shown are lines of the calibration source (red).

tion source represents the Lyman series of hydrogen-like Xe and is superimposed by a sum of several gaussian fits depicted in dark green. The corresponding transitions from helium-like ions, marked in orange, are discussed in the next section. Around

30 keV additional Kα radiation from the Xe gas target of different charge states can be seen. Table 6.6 shows all the lines of the Lyman series that could be clearly identified together with their energy E_{lab} in the laboratory frame. While the Ly-α, Ly-β and Ly-γ lines were fittet with two individual lines each, a single gaussian fit was used for the higher order transitions. To extract the energy E_{rest} in the rest frame

Line	E_{lab} [eV]	E_{rest} [eV]	E_{th} [eV]	Relative intensity [%]
Ly-α_2	} 34738 $\pm$ 2	30857 $\pm$ 2	30856.36	} 38.2 $\pm$ 1.6
Ly-α_3			30863.49	
Ly-α_1	35218.0 $\pm$ 1.1	31283.8 $\pm$ 1.0	31283.77	61.8 $\pm$ 2.1
Ly-$\beta_{2/3}$	41320 $\pm$ 3	36704 $\pm$ 3	36706.6	} 27.0 $\pm$ 1.4
Ly-β_1	41465.1 $\pm$ 1.3	36833.0 $\pm$ 1.2	36833.4	
Ly-γ	43604 $\pm$ 18	38733 $\pm$ 16	38736.2	} 11.5 $\pm$ 0.9
	43670 $\pm$ 11	38792 $\pm$ 10	38789.5	
Ly-δ	44690.9 $\pm$ 1.9	39697.6 $\pm$ 1.7	-	5.7 $\pm$ 0.7
Ly-ϵ	45263 $\pm$ 4	40207 $\pm$ 4	-	2.9 $\pm$ 0.4
Ly-ζ	45584 $\pm$ 7	40492 $\pm$ 6	-	2.0 $\pm$ 0.4
Ly-η	45810 $\pm$ 10	40693 $\pm$ 9	-	1.5 $\pm$ 0.3

Table 6.6: Parameters of the recorded lines of the Lyman-series of Xe^{53+}. The intensities of the lines are given relative to the combined Ly-α transitions and were corrected for the finite stopping power of the detector, while any energy-dependence of the finite transmission through the materials between source and detector can be neglected in this energy range. The noted error only includes the fitting error and no systematic errors due to non-linearity or Doppler shift. Theoretical values E_{th} are taken from [Joh85] for Ly-α transitions and [Gas16] for Ly-β and Ly-γ.

of the ion a Doppler correction of the measured energy is necessary as described in section 5.4.3. However, the exact determination of the observation angle is rather difficult as the exact position of the gas jet inside the target chamber as well as the exact position of the detector inside the cryostat are not well known. In particular, any thermal contraction within the cryostat during the cool-down influences the resulting position of the detector. As even small uncertainties in the observation angle may have large effects on the Doppler shift, an a priori correction does not seem feasible. Instead the Doppler shift was determined from the theoretical value 31 283.77 eV for the energy of the Ly-α_1 line calculated by Johnson and Soff [Joh85] to be $E_{\text{lab}}/E_{\text{rest}} = 1.12576$. This corresponds to an observation angle of 60.124° and thus a deviation of only 4 mm in the detector or gas target position which is – given the above-mentioned difficulties – within the expected uncertainty.

The Xe Ly-α_1 line is perfectly suited to discuss the line broadening of the lines

from the gas target as it can be resolved as a single line. Interpolating from the baseline resolution and the γ_{2-0} and γ_{2-1} lines of the ^{241}Am calibration source one would expect a detector broadening of $\Delta E_{\mathrm{FWHM}} = 47\,\mathrm{eV}$ at $35\,\mathrm{keV}$. The observed energy resolution of $\Delta E_{\mathrm{FWHM}} = 80\,\mathrm{eV}$ however is much larger and can not only be explained by the expected Doppler broadening which is according to equation 5.4 in the range of $25\,\mathrm{eV}$ for the given experimental setup and a gas target diameter of $5\,\mathrm{mm}$. Lacking a second electron, shake-up or shake-off processes, which could also lead to an apparently increased linewidth due to satellite transitions, are not possible for hydrogen-like ions. If possibly remaining non-linearities are different for both pixels, this could lead to an additional broadening of a few eV. Another contribution to the line width could result from the natural line width of the transition itself which scales with Z^4 and is expected to be of the order of $10\,\mathrm{eV}$ to $20\,\mathrm{eV}$[1]. Probably all these effects and maybe a larger diameter of the gas jet target contribute to the increased line width.

The relative intensities of the individual lines compared to the Ly-α transition are also listed in table 6.6 and are depicted in figure 6.28. While the energy-dependence of the transmission through the X-ray windows and the air between gas target and cryostat is negligible for the considered energy range, the measured line intensities were corrected by the energy-dependent absorption efficiency of the absorbers made of $200\,\mathrm{\mu m}$ thick gold according to section 3.2. The experimental data can be described
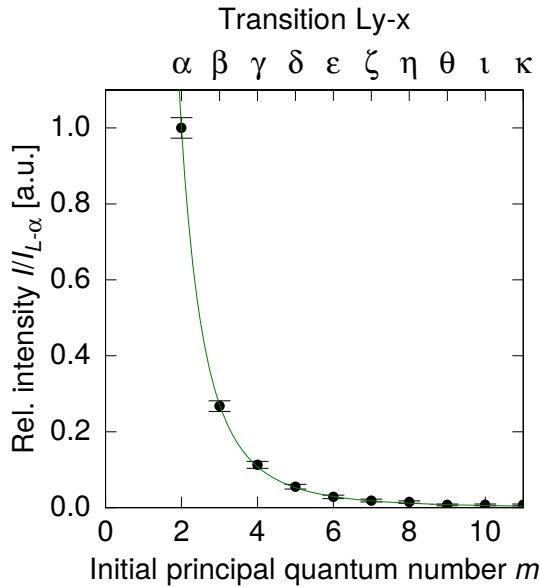
Figure 6.28: Intensities of the Lyman transitions of Xe^{53+} in relation to the Ly-α transition (black dots) and a fit in green according to the function $I/I_{Ly-\alpha} = 2^\xi/m^\xi$ with a resulting value of $\xi = 3.21$.

very well by the function $I/I_{Ly-\alpha} = 2^\xi/m^\xi$, where m denotes the principal quantum number of the corresponding initial state of each $m \to 1$ transition. The best fit is obtained with the parameter $\xi = 3.21$ and is overlaid in green. This behaviour

---

[1]Private communication with Th. Stöhlker

is close to the expected $I \propto 1/m^3$ behaviour for the electron capture cross section in high energy collisions, while for low energy collisions with beam energies around $0\,\text{eV/u}$ a dependence of $I \propto 1/m$ would be expected [Reu06].

Spectrum from He-like Xe^{52+} ions Some of the bare Xe^{54+} ions in the experiment captured two instead of only one electron from the Xe gas target and subsequently emitted X-rays from excited helium-like Xe^{52+} ions. Figure 6.29 shows the corresponding $K\alpha$ transitions that are also marked in the energy level scheme in figure 2.2. A gaussian fit of the y- and z-lines and of the combined x/w-doublet is also depicted in orange. Table 6.7 shows the resulting energies and intensities together
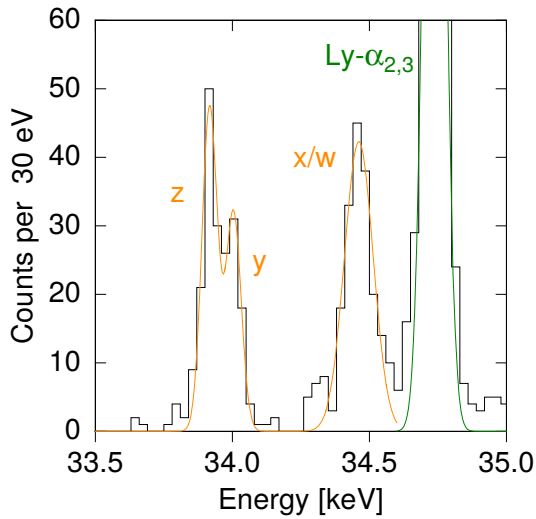

Figure 6.29: Histogram of the K$_\alpha$ transitions of helium-like Xe^{52+}. Superimposed in orange are gaussian fits of the individual lines.

with transitions from higher shells. The energies in the rest frame of the ion were calculated with the Doppler shift determined from the Ly-α_1 transition as discussed in the previous section, while the intensities were again normalized to the Ly-α line. Theoretical values $E_{\text{lit}}^{\text{th}}$ from [Pla94] are also listed as well as experimental data $E_{\text{lit}}^{\text{exp}}$ by Widmann et al. , measured with a crystal spectrometer on Xe ions originating from an electron beam ion trap [Wid00]. The agreement with the theoretical values is very good for the z- and y-transition. Also any systematic uncertainties regarding the non-linearity of the detector should be very small for these two lines as the finite energy calibration is done together with the Doppler correction with respect to the Ly-α_1 line which has an only $1\,\text{keV}$ higher energy. The doublet of the w- and possible x-transitions could not be resolved. The much broader line profile compared to the individual lines of the y/z doublet could either be due to a larger natural linewidth or due to a non-negligible contribution of the x-line which is a magnetic quadrupole transition.

Line	E_{lab} [eV]	E_{rest} [eV]	$E_{\text{lit}}^{\text{th}}$ [eV]	$E_{\text{lit}}^{\text{exp}}$ [eV]	Rel. intensity [%]
z	33917.1 ± 1.4	30128.2 ± 1.2	30128.8	30131 ± 4	
y	34004.0 ± 2.2	30205.4 ± 2.0	30205.9	30215 ± 5	28.0 ± 1.5
x	34461 ± 5	30610 ± 4	30593.9	-	
w			30629.7	30625 ± 5	
	40297 ± 7	35795 ± 6	-	-	
Kβ	40386 ± 6	35874 ± 5	-	-	4.4 ± 0.6
	40510 ± 5	35985 ± 4	-	-	
Kγ	42595 ± 8	37837 ± 7	-	-	1.8 ± 0.4
Kδ	44157 ± 28	39224 ± 25	-	-	0.7 ± 0.2

Table 6.7: Transition energies of the K-transitions in helium-like Xe^{52+} in the laboratory frame E_{lab} and in the rest frame E_{rest} of the ions. The noted uncertainties of the data of this work only include fitting errors and no systematic errors due to Doppler shift or a possibly remaining non-linearity. Literature values are taken from [Pla94] ($E_{\text{lit}}^{\text{th}}$, theoretical) and [Wid00] ($E_{\text{lit}}^{\text{exp}}$, experimental).

6.2.4 *maXs30*: U^{89+} on N$_2$ gas target

In a third measurement campaign at the internal gas target of the ESR the newly developed *maXs30* detector array was used in an experiment where lithium-like U^{89+} ions with a beam energy of 75 MeV/u interacted with a N$_2$ gas target. The cryostat with the detector was set up at the 90° port of the ESR in a distance of about 1.5 m from the interaction point. A special challenge was imposed by the expected transition energies that go down to 4 keV and request a high transmission between gas target and cryostat for low-energy X-rays, including high transmission X-ray windows.

Setup for the detection of low-energy X-rays   The X-ray windows that were used inside the cryostat are discussed in section 5.1.2. The radiation windows have a combined transmission of 86 % for photons with an energy of 4 keV. For the vacuum window the 25 µm thin beryllium window with a transmission above 90 % for X-rays with energies above 3 keV was chosen. Thus, the main loss of photons would result from absorption within 1.25 m of air between the X-ray window of the interaction chamber of the ESR and the one of the cryostat. As this would lead to practically complete absorption, a tube that was filled with helium gas slightly above ambient pressure was inserted between the ESR and the cryostat. Figure 6.30 depicts a photograph of this tube and the side arm of the cryostat. The absorption inside the tube with a length of about 120 cm only amounts to less than 2 % for X-rays
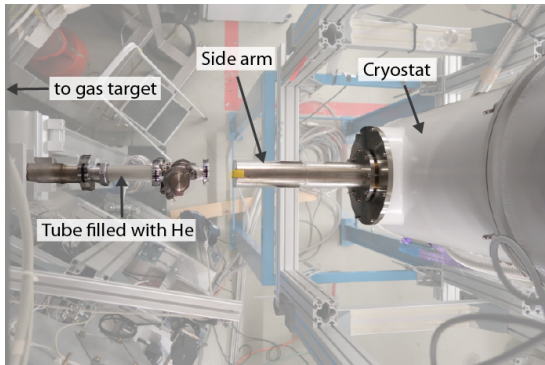
Figure 6.30: Top view of the side arm of the cryostat and the tube that was filled with helium and that was inserted between the cryostat and the ESR to minimize the absorption of low energy X-rays by air.

with an energy of 4 keV, leaving the remaining approximately 7 cm of air as the most relevant loss mechanism with an absorption of 40 % at this photon energy. Due to the non-existance of a dead-layer, the detector itself does not limit the capability to detect photons in the keV-range.

General detector performance   Five of the 32 read-out channels, could not be operated due to shortages or broken wires in the cryostat or due to defective SQUID current sensors. In five additional channels no signal could be detected, most likely due to defective meanders or read-out lines on the detector chip. Of the remaining 44 detector pixels, four pixels suffered from external noise coupling to the detector and 40 pixels were used for data acquisition together with the newly developed 32-channel digitizer system that is described in section 5.2.2. Altogether these pixels feature an active detection area of 10 mm^2. A more detailed analysis of the detector performance and homogeneity across a *maXs30* detector array is found in section 6.1.10. However, many detector channels suffered from a highly increased noise level as most of the SQUID current sensors that were available at the time of the measurement were contaminated with magnetic impurities due to fabrication problems. Therefore, the following analysis is based on the 10 pixels with the best signal-to-noise ratio.

Linearity and energy resolution   The non-linearity corrections were based on the $L\beta_1$, $L\gamma_1$, γ_{2-1} and γ_{1-0} lines of an ^{241}Am calibration source. To correct the non-linearity of the detector a quadratic as well as a cubic correction were performed as discussed in section 6.1.8 to test the influence of the corrections on the line centroids. At energies of 4 keV and 26.3 keV the difference between both corrections amounts to 2.5 eV which can be seen as the systematic error of the non-linearity correction. All spectra that are shown and discussed in this section use the cubic correction. Figure 6.31 shows the deviation from the line centroids of the four calibration lines from the literature values for the different pixels after the non-linearity correction. A very good agreement between the different pixels and with values from literature is found. Several additional lines that can be identified in the combined spectrum
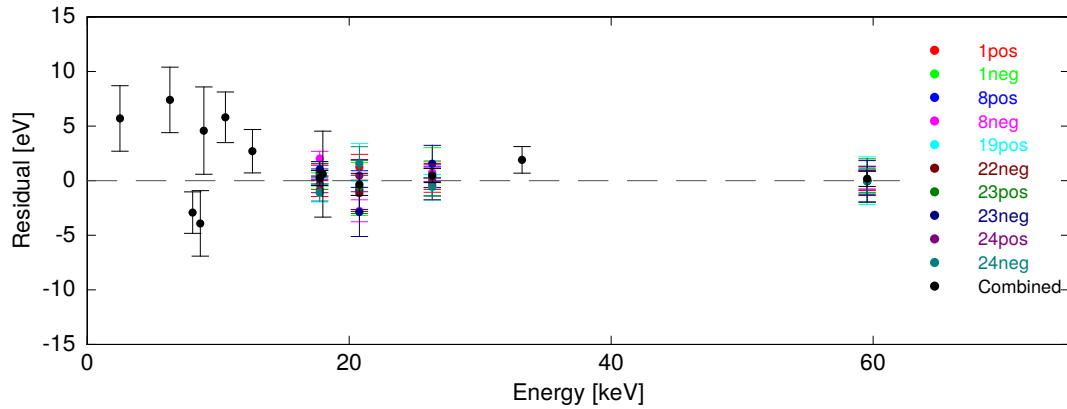
Figure 6.31: Deviations of the line centroids of the four calibration lines from the literature values after the non-linearity correction for ten different pixels that are shown in different colours. Also shown in black are the deviations for several other lines after the combination of the individual spectra. The errorbars include the fitting errors from the determination of the line centroids.

of all pixels are also shown; notably the γ_{1-0} and $L\beta_3$ of the ^{241}Am source as well as the fluorescence lines of several materials that can be found near the detector or the source, notably Pb $L\alpha_1$, Pb $L\beta_1$, Cu K_α, Cu K_β, Zn K_α and several escape lines below 7 keV. Within their errorbars these lines agree with the expectation, yet, at lower energies a trend to higher residuals can be seen. This tendency, however, is within the uncertainty of the non-linearity correction that was mentioned above.

The combined line broadening of the detector at 26.3 keV is around 43 eV, while the single pixel energy resolution ranges from 30 eV to 60 eV. Therefore, no degradation of the line broadening due to the combination of the different pixels can be observed. With a combined line broadening of 72 eV at 59.5 keV an energy dependence is observed that is likely due to temperature variations on a level of 1.1×10^{-3}, corresponding to variations of the order of 20 μK. In future experiments this problem should be overcome with improved thermometry and temperature regulation.

Detector response function   The measurement with an ^{241}Am calibration source shows that the detector response was not purely Gaussian during this measurement, in contrast to the measurements that were discussed in section 6.2.1. Instead, in all operated pixels of the detector array satellite peaks occured at lower and higher energies. Figure 6.32 shows these satellites for the 26.3 keV and 59.5 keV lines of the americium source. For both lines the actual detector response to a mono-energetic
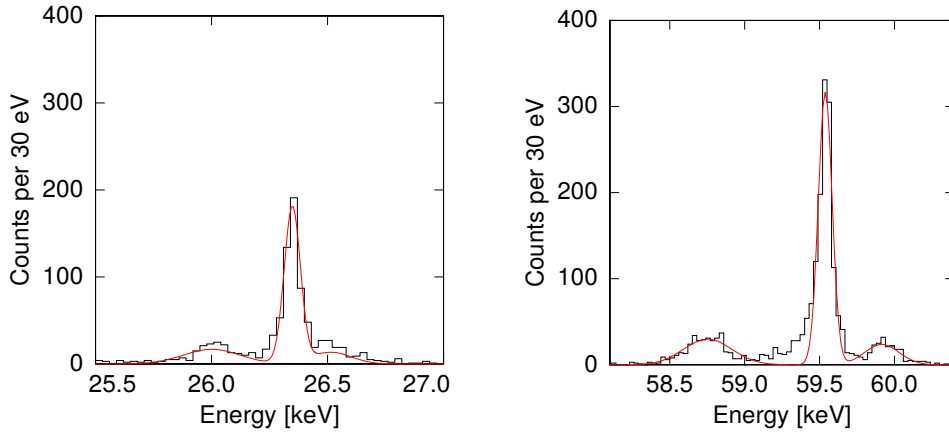
Figure 6.32: Histograms of the γ_{2-1} **(left)** and γ_{2-0} **(right)** lines of the ^{241}Am calibration source. Both lines show additional satellite peaks that are discussed in the text. Numerical fits based on equation 6.20 describing these satellites are superimposed in red.

source with an energy E_0 can empirically be well described by

$$I(E) = I_0 \left(G(E, E_0, \sigma) + i_{s1}G(E, e_{s1}E_0, s_{s1}\sigma) + i_{s2}G(E, e_{s2}E_0, s_{s2}\sigma) \right) \qquad (6.20)$$

with the Gaussian distribution $G(x, x_0, s) = \exp(-(x - x_0)^2/2s^2)$. The energy-independent parameters $i_{s1} = 0.094$, $i_{s2} = 0.075$, $e_{s1} = 0.98682$, $e_{s2} = 1.00636$, $s_{s1} = 3.5$ and $s_{s2} = 2.5$ define the detector response function while the line intensity I_0 and the width σ as well as the energy E_0 depend on the investigated line. Numerical fits based on this equation are superimposed in red, showing a good agreement for both lines. The reason for these satellites can be found in an operating temperature that varies between several distinct temperatures, each responsible for one of the observed (satellite) peaks. This assumption can be verified by a look at the purposely non-gradiometric, and therefore temperature-sensitive, detector channel. Figure 6.33 shows the relative amplitude of the γ_{2-0} line in dependence of the pretrigger voltage for a gradiometric and the purposely non-gradiometric detector of the *maXs30* detector array. In both plots up to four groups can be identified, representing the predominant peak as well as its satellites. In case of the non-gradiometric detector the pretrigger voltage depends on the magnetic flux as well as the temperature of the detector as shown in section 3.4.3. The linear relationship between pretrigger voltage and signal amplitude in this detector channel shows that the reason for the satellite peaks can be found in several distinct detector temperatures during the measurement. The occurance of such distinct temperatures as opposed to smooth temperature fluctuations can for example be explained with one or several SQUID current sensor(s) with multiple working points. Depending on the working point
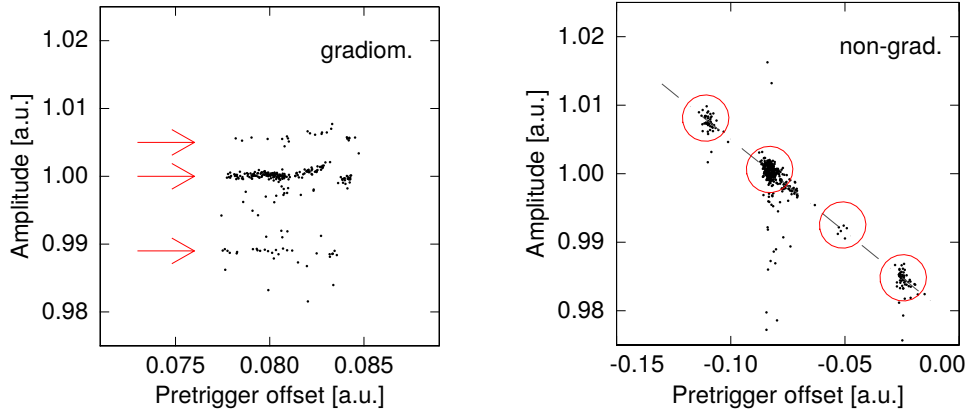
Figure 6.33: Relative amplitude of the γ_{2-0} line of ^{241}Am in dependence of the pretrigger voltage for a gradiometric **(left)** and a non-gradiometric **(right)** detector channel. Up to four distinct groups, corresponding to four different operating temperatures of the detector chip, can be identified.

a different feedback current would be driven through the feedback coil of the flux locked loop setup (ref. section 5.2.1). This in turn would lead to distinct levels of power dissipation in any remaining normal conducting parts of the wiring, thereby heating the detector chip. Based on this explanation, the parameters i_{s1} and i_{s2} in equation 6.20 are linked to the relative time duration during which the detector is at the corresponding working temperature.

By applying the approximately linear correlation between amplitude and pretrigger voltage of the non-gradiometric detector to all signals of this detector, the signal amplitudes can be corrected for the different temperatures. However, for fully gradiometric detectors this can not be done as the pretrigger voltage does not depend on the detector temperature as depicted on the left-hand side of figure 6.33. To apply a temperature correction for gradiometric detectors it would be essential to acquire the pretrigger voltage of the non-gradiometric detector together with each photon that is detected by the detector array. This feature was later added to the 32-cannel acquisition system but was not yet available for the measurements that are discussed in this section.

Experimental results   Figure 6.34 shows an overview of the combined spectrum that was taken with 10 pixels of a *maXs30* detector array over 29.8 h as a beam of lithium-like U^{89+} ions was interacting with a N$_2$ gas jet target at a beam energy of 75 MeV/u. The spectrum is dominated by the intrashell transition in the L shell of the uranium ion at an energy of about 4 keV while at energies between 10 keV and 20 keV the Balmer series can be observed. The dominating part of the detected X-rays
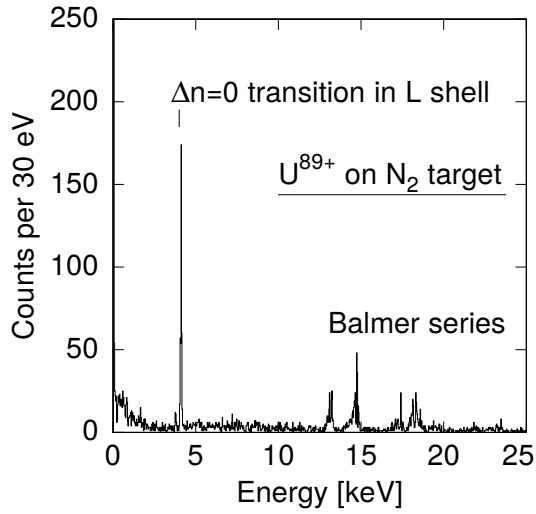
Figure 6.34: Overview of the lines that were emitted by lithium-like U^{89+} ions that were interacting with a N_2 gas jet target at a beam energy of $75\,\mathrm{MeV/u}$. The energies on the x-axis are given in the laboratory frame.

originate from lithium-like U^{89+} ions that were excited during the interaction with the gas target, but also X-rays from beryllium-like U^{88+} originating from recombination processes are possible.

Intrashell transition   The energy range around $4\,\mathrm{keV}$ is depicted in figure 6.35, showing the dominant $2p_{3/2} \to 2s_{1/2}$ intrashell transition of singly excited U^{89+}. Superimposed is a numerical fit based on equation 6.20. The only free parameters were the total amplitude $I_0 = 29.3 \pm 1.6$, the energy $E_0^{\mathrm{lab}} = (4125.8 \pm 1.0)\,\mathrm{eV}$ and the width $\sigma = (15.3 \pm 1.0)\,\mathrm{eV}$ of the predominant peak. Based on the nominal detection angle of $90°$ and a beam energy of $75\,\mathrm{MeV/u}$, the Doppler shift of $E_0^{\mathrm{lab}}/E_0^{\mathrm{rest}} = 0.92549$ leads to a transition energy of $E_0^{\mathrm{rest}} = (4458.0 \pm 1.1)\,\mathrm{eV}$ in the rest frame of the ions. This is in very good agreement with the theoretical value of $(4459.4 \pm 0.4)\,\mathrm{eV}$ for this
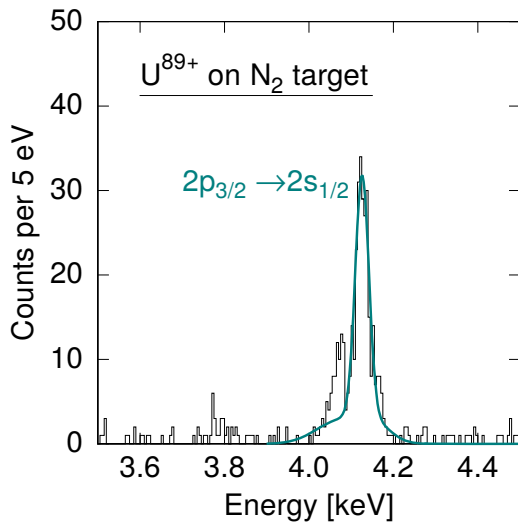

Figure 6.35: Histogram of the $2p_{3/2} \to 2s_{1/2}$ intrashell transition in singly excited U^{89+}. Superimposed is a numerical fit based on equation 6.20 that describes the detector line shape.

transition [Bei93]. The additional peak that can be seen around $E_0^{\text{lab}} = 4.07\,\text{keV}$, corresponding to $E_0^{\text{rest}} = 4.40\,\text{keV}$ can most likely be identified with the low-energy satellite that originates from the varying operating temperature and that is expected at an energy of $4.071\,\text{keV}$ according to equation 6.20. Together with the small high-energy shoulder one can conclude that the relative amplitudes of the satellites with respect to the predominant peak changed compared to the calibration measurement. This can be explained, if the relative time period during which the detector chip is at a certain operating temperature, changes over time, and has to be considered during the further analysis of this spectrum.

Balmer series   Figure 6.36 shows the Balmer series resulting from the interaction of U^{89+} with a N_2 gas target. At this energy range we expect the satellites due to different operating temperatures to be in a distance of around $-200\,\text{eV}$ and $+100\,\text{eV}$ with respect to the predominant peak. Therefore, these satellites might be respon-
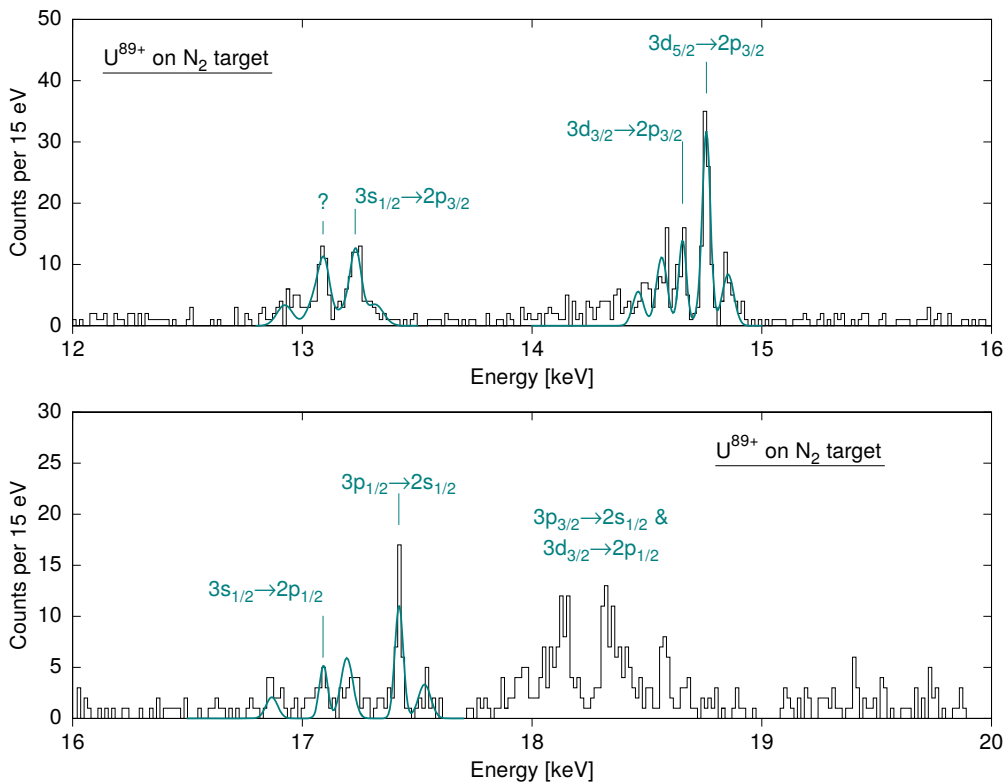

Figure 6.36: Observed Balmer series following the interaction of U^{89+} ions with a N_2 gas target at a beam velocity of $75\,\text{MeV/u}$ taken during $29.8\,\text{h}$ with 10 pixels of the *maXs30* detector array. Energies are given in the laboratory frame.

sible for some of the structures that can be seen within the lines of the Balmer series. Possibly varying amplitudes of the satellites – also due to their low statistics – make an identification of distinct transitions quite challenging. This problem is further increased as additional lines originating from transitions in beryllium-like U^{88+} ions might also be present. Several numerical fits are superimposed, each based on equation 6.20 with relative amplitudes and widths that were extracted from the measurement of the $2p_{3/2} \rightarrow 2s_{1/2}$ intrashell transition. The predominant peaks are labeled with possible transition candidates while the associated satellites are not labeled. The energy ranges from 12.5 keV to 13.5 keV, from 14.5 keV to 15.0 keV and from 16.5 keV to 17.5 keV can be described with two observed lines each. While two of these doublets can most likely be attributed to transitions in U^{89+}, only one line of the first doublet can be explained with the $3s_{1/2} \rightarrow 2p_{3/2}$ transition of this ion species. The energies of all these lines are listed in table 6.8 together with the possible transition candidates. From the observed energies of the $3s_{1/2} \rightarrow 2p_{1/2}$ and the

E_0^{lab} [eV]	E_0^{rest} [eV]	candidate
13096 ± 5	14150 ± 5	?
13233 ± 3	14298 ± 3	$3s_{1/2} \rightarrow 2p_{3/2}$
14655 ± 4	15834 ± 4	$3d_{3/2} \rightarrow 2p_{3/2}$
14759 ± 2	15947 ± 2	$3d_{5/2} \rightarrow 2p_{3/2}$
17092 ± 6	18468 ± 6	$3s_{1/2} \rightarrow 2p_{1/2}$
17421 ± 3	18823 ± 3	$3p_{1/2} \rightarrow 2s_{1/2}$

Table 6.8: Energies of the observed lines following the interaction of U^{89+} ions with a N_2 gas target at a beam velocity of 75 MeV/u and possible transition candidates of U^{89+}. The Doppler shift was determined for an observation angle of $90°$ while the listed uncertainties only include fitting uncertainties and no uncertainty due to Doppler correction or non-linearity correction.

$3s_{1/2} \rightarrow 2p_{3/2}$ transitions together with the measured $2p_{3/2} \rightarrow 2s_{1/2}$ transition that was discussed in the previous section, one can calculate the energy splitting between the $2p_{1/2}$ and the $2s_{1/2}$ state to be around (288 ± 7) eV which is in good agreement with the value of (280.6 ± 0.1) eV that was optained by Doppler-tuned spectroscopy [Sch91]. The uncertainty is dominated by the small statistics of the $3s_{1/2} \rightarrow 2p_{1/2}$ transition. Although the measurement suffered from the variation of the detector temperature resulting in the observed satellites, it also shows that individual spectra of several pixels can be reliably combined. Together with the very small background this allowed the observation of lines with a small intensity, that could not be detected with a single pixel. As it was shown in figure 6.33, the temperature variations can be corrected for with the help of a temperature sensitive detector. Meanwhile, the acquisition system was extended in such a way that the signal of the temperature sensitive

detector can be acquired for every triggered signal in other channels of the detector array. Thereby, the voltage value of this special channel that scales with the detector temperature can be used to estimate the temperature of the detector chip for each single detected photon and to correct for potential temperature variations during the measurement. In this way also the non-Gaussian detector response that was observed in this experiment can be accounted for, making high precision measurements with the *maXs30* detector array feasible. This experiment also demonstrated very well the main advantages of metallic magnetic calorimeters, which is the high absorption efficiency and above all the capability to simultaneously measure transitions that cover a larger energy range with a high energy resolution.

7. Conclusion and Outlook

With 8x8 pixels the two-dimensional micro-calorimeter array *maXs30* that was developed, fabricated and characterized in the framework of this thesis, provides an active detection area of $4\,\text{mm} \times 4\,\text{mm}$. The 64 absorbers are connected to 64 temperature sensors made of $\underline{\text{Ag}}$:Er that are combined in 32 detector channels. The designed detector is optimized for X-rays with energies up to $30\,\text{keV}$. Based on thermodynamic principles and including all relevant noise contributions, a complete numerical optimization of the detector was performed, resulting in an expected energy resolution below $7\,\text{eV}$ (FWHM) at a working temperature of $20\,\text{mK}$. Here, the stronger RKKY interaction of the sensor material $\underline{\text{Ag}}$:Er that can be expressed by the parameter α was extrapolated by appropriate scaling from numerical simulations of the well-understood sensor material $\underline{\text{Au}}$:Er. The actual detector arrays discussed in this thesis were fabricated in-house, feature absorbers with a thickness of around $7\,\mu\text{m}$ and were thoroughly characterized in a dry dilution refrigerator.

The signal rise time is slowed down as expected from the artificial thermal bottleneck that was introduced between the absorber and the temperature sensor of each detector. Thereby, a position dependent signal shape as it was observed in [Pie12] can be prevented. An investigation of the signal decay leads to the conclusion that at low temperatures the thermal coupling between the two pixels of each detector channel is stronger than the coupling to the thermal bath of the cryostat. Apart from this effect the signal decay shows a pure exponential behaviour down to the lowest temperatures and the additional fast signal decay, observed for detectors with sensors made of $\underline{\text{Au}}$:Er, is not seen. This supports the previous interpretation that this decay component is caused by quadrupole moments of the gold nuclei as the new host material silver does not exhibit a nuclear quadrupole moment. In future *maXs30* detector arrays the thermal coupling to the heat bath will be improved by a through-wafer thermalization based on holes through the chip substrate that are filled with gold. The first step of this new process was successfully developed in the framework of this thesis and makes use of an anisotropic etching of the silicon substrate by a mixture of SF_6 and O_2 in a reactive ion etching process.

The observed temperature-dependences of the sensor magnetization as well as of the signal height can be described by assuming the RKKY interaction with an interaction parameter $\alpha = 10 \ldots 15$, where $\alpha = 12.5$ results in a very good agreement of the measurements with the expected detector behaviour. The non-linearity of the detector that was investigated in the range from $0\,\text{keV}$ to $60\,\text{keV}$ can very well be described with a quadratic behaviour and agrees well with the expectations from a

second-order Taylor expansion of the detector response function. Small deviations from the quadratic behaviour that were found for some detector channels might be attributed to possible non-linearities of the detector read-out.

To reduce crosstalk between the individual detector channels of the close-packed array, the detectors make use of a new highly-gradiometric geometry. From a magnetization measurement the remaining asymmetry of such a detector could be determined to be less than 2×10^{-4}. Accordingly the crosstalk between two neighbouring detectors is one order of magnitude smaller than for earlier linear detector arrays that were developed in our group [Pie12, Sch12]. One detector pair of each array is purposely produced with a defined asymmetry to make it sensitive to the temperature of the detector chip. This allows an individual correction of the signal height – also for the gradiometric detector channels – based on the chip temperature, resulting in a measured energy resolution of $\Delta E_{\mathrm{FWHM}} = 20.3 \, \mathrm{eV}$ at an energy of $E = 59.541 \, \mathrm{keV}$, measured with the γ_{2-0} line of an ^{241}Am calibration source. Most likely the corresponding resolving power of $E/\Delta E_{\mathrm{FWHM}} = 2933$ is still limited by small temperature fluctuations that were not fully corrected. Nevertheless, with this energy resolution a satellite of the Lα_1 line of the ^{241}Am calibration source with an energy of $13.972 \, \mathrm{keV}$ could be resolved that most likely results from one or more additional vacancies in the electronic shell after a Coster Kronig transition or a shake-off process. In a separate measurement the intrinsic energy resolution of the detector was determined to be $7.87 \, \mathrm{eV}$ which is in good agreement with the expected resolution of $7.48 \, \mathrm{eV}$ for a detector with $7 \, \mu\mathrm{m}$ thick absorbers and a field-generating current of $35 \, \mathrm{mA}$ at an operating temperature of $25.5 \, \mathrm{mK}$.

Of one *maXs30* detector array 53 of the 64 detector pixels were successfully operated. Four of the remaining 11 pixels showed visible defects from the microfabrication like broken or short-circuited wiring. Most of the detector parameters that were investigated show a good homogeneity across the different detector channels of the chip. Larger inhomogeneities were found for the signal height and the inductance of the pick-up coil. Both most likely result from the inhomogeneous and isotropic wet etching process that was used to microfabricate the first niobium layer of the detector. This process can result in short-circuited meander stripes and also in weak spots in the niobium structure. The latter may limit the critical currents and, therefore, the field-generating persistent current of the detectors and the signal height. Hence, future devices make use of a first niobium layer that is fabricated in a more homogeneous dry etching process.

With an absorber thickness of $30 \, \mu\mathrm{m}$ the *maXs30* detector array would feature absorption efficiencies above $40 \, \%$ up to energies of $45 \, \mathrm{keV}$. Therefore, it would be for example perfectly suited for the high-resolution X-ray spectroscopy of highly charged heavy ions. Such ions can be produced with high-energy accelerators and

are stored and investigated in storage rings as the Experimental Storage Ring ESR at the GSI. Subsequently, for the application of the *maXs30* detector at storage rings or other places with a restricted access during the measurement, a dry ^{3}He/^{4}He dilution refrigerator, that can be remotely operated, was set up and equipped for the read-out of up to 32 two-stage SQUID channels. The cryostat allows different detector arrays to be mounted at the end of a side arm to reduce the distance between X-ray source and detectors. Special care was taken to shield the detector and the SQUID current-sensors from external magnetic fields with the use of soft-magnetic and superconducting shieldings.

The first tests at the ESR were performed with a *maXs200* detector and it was shown that magnetic micro-calorimeters can be operated in the environment of the storage ring without significant degradation of the energy resolution. The detector system, including the remote-controlled cryostat reached duty cycles above 70 %, limited by the cooling water supply of the GSI. After the interaction of a bare Xe^{54+} ion beam with a neutral Xe gas jet target the transitions in hydrogen-like Xe^{53+} and helium-like Xe^{52+} were investigated and the Lyman series of Xe^{53+} could be observed up to Ly-η. The Kα transition of Xe^{52+} was measured and the M1 transition at $(30\,128.2 \pm 1.2)\,\mathrm{eV}$ and the intercombination K$_\alpha$ line at $(30\,205.4 \pm 2.0)\,\mathrm{eV}$ could be resolved.

The newly developed *maXs30* detector was applied in an experiment at the ESR where low-energy X-rays with energies down to 4 keV, originating from lithium-like U^{89+} ions that were interacting with a N_2 gas jet target, were investigated. A new 32-channel data acquisition system that was developed during this thesis and already was successfully deployed in several other measurements was used. During the measuring campaign with low photon flux the combining of the spectra of several individual detector pixels to a single spectrum was demonstrated.

In future the number of pixels and, therefore, the detection area is expected to increase further by implementing multiplexing techniques [Weg13]. Additionally detector arrays that include different types of magnetic calorimeters might open new interesting applications. Such a detector array could combine large-area pixels with smaller pixels that provide an energy resolution around 1 eV. This type of detector might be especially interesting in conjunction with X-ray lenses that focus a certain energy range on these high-resolution pixels. Such lenses have already been tested together with a *maXs30* detector [Sch16].

However, with the fast signal rise time, large dynamic range, very good linearity and with the high energy resolution, the two-dimensional *maXs30* detector array is already a very good device for future experiments in the regime of high-resolution X-ray spectroscopy. Besides the measurements that are discussed in this thesis, the *maXs30* detector array has already been deployed in several other experiments

[Sch16, Pon17]. Especially highly-charged heavy ions, that are interesting candidates for high-precision QED tests in the limit of large electric and magnetic fields, can be studied with this detector for example at the Experimental Storage Ring or at electron beam ion traps. New facilities that are currently being set-up at the GSI/FAIR, notably the low-energy storage ring CRYRING [Les16], the ion trap HITRAP [Qui01] and the electron beam ion trap S-EBIT, will greatly reduce the velocity of the investigated highly charged ions and the associated Doppler shift and Doppler broadening and, therefore, provide very interesting experimental conditions for the *maXs* detector system.

A. Microfabrication

Figure A.1: Photographic images of the fabrication process of the *maXs30* detector after the individual layers that are specified in table 4.5. (1) First niobium layer, (2) anodization and first 120 nm of the first SiO$_2$ layer, (3) remaining 180 nm of the first SiO$_2$ layer, (4) AuPd heater, (5) second niobium layer, (6) second isolation layer made of 180 nm of SiO$_2$.
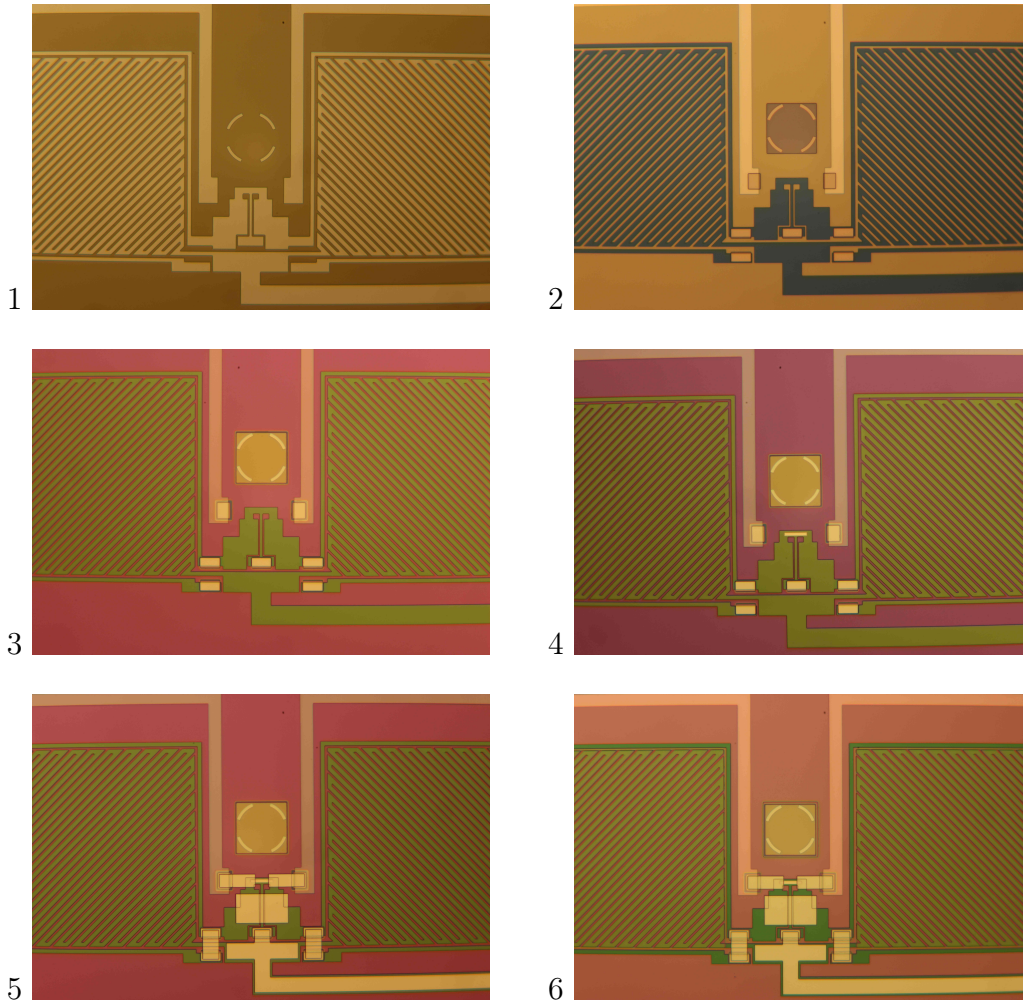
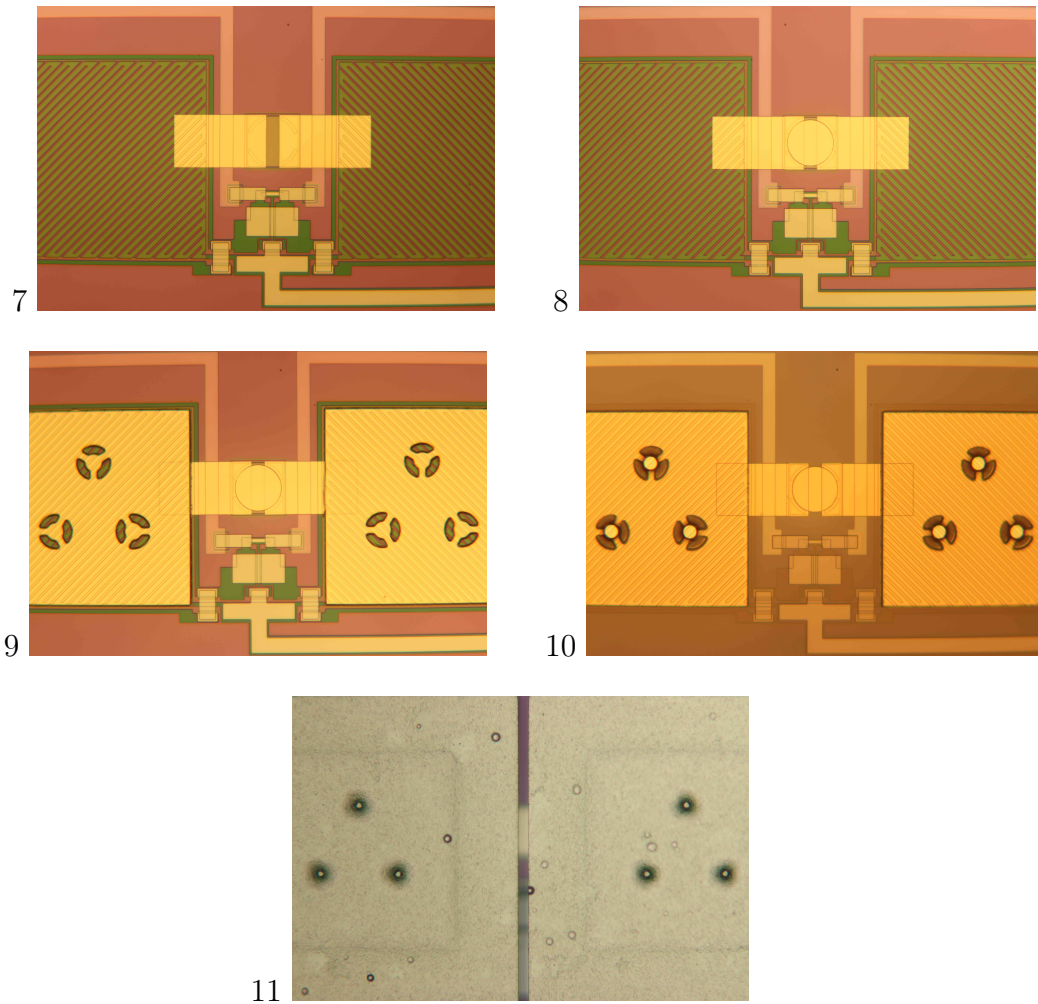**Figure A.2:** Photographic images of the fabrication process of the *maXs30* detector after the individual layers that are specified in table 4.5. (7) first and (8) second part of the thermalization layer, (9) paramagnetic temperature sensor, (10) photoresist with holes for the stems between absorbers and sensors, (11) finished detector after electroplating of the absorbers together with the stems in a two-layer process.

Bibliography

[Abr70]   A. Abragam and B. Bleaney, Electron Paramagnetic Resonance of Transition Metals, Claredon Press Oxford, 1970.

[Bat16]   C. R. Bates, C. Pies, S. Kempf, D. Hengstler, A. Fleischmann, L. Gastaldo, C. Enss, and S. Friedrich, Reproducibility and calibration of MMC-based high-resolution gamma detectors, *Applied Physics Letters*, **109**(2), 023513, 2016.

[Bé10]   M.-M. Bé, V. Chisté, C. Dulieu, X. Mougeot, E. Browne, V. Chechev, N. Kuzmenko, F. Kondev, A. Luca, M. Galán, A. Nichols, A. Arinc, and X. Huang, Table of Radionuclides, Volume 5 in *Monographie BIPM-5*, Bureau International des Poids et Mesures, Pavillon de Breteuil, F-92310 Sèvres, France, 2010.

[Bea67]   J. A. Bearden, X-ray wavelengths, *Rev. Mod. Phys.*, **39**, 78–124, 1967.

[Bei93]   P. Beiersdorfer, D. Knapp, R. E. Marrs, S. R. Elliott, and M. H. Chen, Structure and Lamb shift of $2s_{1/2}$-$2p_{3/2}$ levels in lithiumlike U^{89+} through neonlike U^{82+}, *Phys. Rev. Lett.*, **71**, 3939–3942, 1993.

[Bey97]   H. F. Beyer, H.-J. Kluge, and V. P. Shevelko, X-Ray Radiation of Highly Charged Ions, Springer-Verlag, Berlin, Heidelberg, New York, 1997.

[Bey99]   H. F. Beyer and V. P. Shevelko (Ed.), Atomic Physics with Heavy Ions, Springer-Verlag, Berlin, Heidelberg, New York, 1999.

[Bro08]   A.-D. Brown, S. R. Bandler, R. Brekosky, J. A. Chervenak, E. Figueroa-Feliciano, F. Finkbeiner, N. Iyomoto, R. L. Kelley, C. A. Kilbourne, F. S. Porter, S. Smith, T. Saab, and J. Sadleir, Absorber materials for transition-edge sensor x-ray microcalorimeters, *J. Low Temp. Phys.*, **151**(1), 413–417, 2008.

[Bru82]   J. J. P. Bruines, V. J. de Waal, and J. E. Mooij, Comment on: 'Dc SQUID: Noise and optimization' by Tesche and Clarke, *J. Low Temp. Phys.*, **46**(3), 383–386, 1982.

[Büh88]   M. Bühler and E. Umlauf, A Magnetic Bolometer for Single-Particle Detection, *Europhys. Lett.*, **5**(4), 297–301, 1988.

[Bur04]   A. Burck, Entwicklung großflächiger magnetischer Kalorimeter zur energieaufgelösten Detektion von Röntgenquanten und hochenergetischen Teilchen, Diploma thesis, Kirchhoff-Institut für Physik, Universität Heidelberg, 2004.

[Bur08]   A. Burck, Entwicklung großflächiger mikrostrukturierter magnetischer Kalorimeter mit Au:Er- und Ag:Er-Sensoren für den energieaufgelösten Nachweis von Röntgenquanten und hochenergetischen Teilchen, PhD Thesis, Kirchhoff-Institut für Physik, Universität Heidelberg, 2008.

[Cha06]   S. Chatterjee, H. F. Beyer, D. Liesen, T. Stöhlker, A. Gumberidze, C. Kozhuharov, D. Banas, D. Protic, K. Beckert, P. Beller, T. Krings, F. Bosch, B. Franzke, S. Hagmann, J. Hoszowska, P. Indelicate, H.-J. Kluge, X. Ma, B. Manil, I. Mohos, et al., The FOCAL spectrometer for accurate X-ray spectroscopy of fast heavy ions, *Nuclear Instruments and Methods in Physics Research*, **245**(1), 67 à 71, 2006.

[Cla04]   J. Clarke and A. I. Braginski (Ed.), The SQUID Handbook, WILEY-VCH, 2004.

[Col70]   H. K. Collan, M. Krusius, and G. R. Pickett, Specific heat of antimony and bismuth between 0.03 and 0.8 k, *Phys. Rev. B*, **1**, 2888–2895, 1970.

[Coo56]   L. N. Cooper, Bound electron pairs in a degenerate fermi gas, *Phys. Rev.*, **104**, 1189–1190, 1956.

[Cos93]   E. Cosulich, F. Gatti, and S. Vitale, Further results on μ-calorimeters with superconducting absorber, *J. Low Temp. Phys.*, **93**(3), 263–268, 1993.

[Dan05]   T. Daniyarov, Metallische magnetische Kalorimeter zum hochauflösenden Nachweis von Röntgenquanten und hochenergetischen Molekülen, PhD Thesis, Kirchhoff-Institut für Physik, Universität Heidelberg, 2005.

[Des03]   R. D. Deslattes, E. G. Kessler, P. Indelicato, L. de Billy, E. Lindroth, and J. Anton, X-ray transition energies: new approach to a comprehensive evaluation, *Rev. Mod. Phys.*, **75**, 35–99, 2003.

[dG17]   S. E. de Graaf, A. A. Adamyan, T. Lindström, D. Erts, S. E. Kubatkin, A. Y. Tzalenchuk, and A. V. Danilov, Direct Identification of Dilute Surface Spins on Al_2O_3: Origin of Flux Noise in Quantum Circuits, *Phys. Rev. Lett.*, **118**, 057703, 2017.

[Ens00]   C. Enss, A. Fleischmann, K. Horst, J. Schönefeld, J. S. Adams, Y. H. Huang, Y. H. Kim, and G. M. Seidel, Metallic magnetic calorimeters for particle detection, *J. Low Temp. Phys.*, **121**(3), 137–176, 2000.

[Ens05]   C. Enss and S. Hunklinger, Low-Temperature Physics, SpringerLink: Springer e-Books, Springer Berlin Heidelberg, 2005.

[Fer15]   A. Ferring, Entwicklung von dc-SQUIDs zur Auslesung von metallischen magnetischen Kalorimetern, Master's thesis, Kirchhoff-Institut für Physik, Universität Heidelberg, 2015.

[Fle98]   A. Fleischmann, Hochauflösendes magnetisches Kalorimeter zur Detektion von einzelnen Röntgenquanten, Diploma thesis, Kirchhoff-Institut für Physik, Universität Heidelberg, 1998.

[Fle00]   A. Fleischmann, J. Schönefeld, J. Sollner, C. Enss, J. S. Adams, S. R. Bandler, Y. H. Kim, and G. M. Seidel, Low temperature properties of erbium in gold, *J. Low Temp. Phys.*, **118**(1), 7–21, 2000.

[Fle03]   A. Fleischmann, Magnetische Mikrokalorimeter: Hochauflösende Röntgenspektroskopie mit energiedispersiven Detektoren, PhD Thesis, Kirchhoff-Institut für Physik, Universität Heidelberg, 2003.

[Fle05]   A. Fleischmann, C. Enss, and G. Seidel, Metallic magnetic calorimeters, in C. Enss (Ed.), *Cryogenic Particle Detection*, 151–216, Springer Berlin Heidelberg, Berlin, Heidelberg, 2005.

[Fle09]   A. Fleischmann, L. Gastaldo, J. Porst, S. Kempf, A. Kirsch, A. Pabinger, C. Pies, P. Ranitzsch, S. Schäfer, F. Seggern, T. Wolf, C. Enss, and G. Seidel, Metallic magnetic calorimeters, *AIP Conf. Proc.*, **1185**, 2009.

[Fra17]   J. v. Fraunhofer, Bestimmung des Brechungs- und Farbenzerstreuungs-Vermögens verschiedener Glasarten, in Bezug auf die Vervollkommnung achromatischer Fernröhre., in *Denkschriften der Königlichen Academie der Wissenschaften zu München für die Jahre 1814 und 1815*, 193–226, Königliche Academie der Wissenschaften, 1817.

[Fra76]   S. Fraga, Handbook of Atomic Data, Elsevier Scientific Publishing Company, Amsterdam, 1976.

[Fra87]   B. Franzke, The heavy ion storage and cooler ring project esr at gsi, *Nucl. Instrum. Methods B*, **24**, 18 – 25, 1987.

[Gab72]   A. H. Gabriel, Dielectronic satellite spectra for highly-charged helium-like ion lines, *Mon. Not. R. Astron. Soc.*, **160**(1), 99–119, 1972.

[Gam13]   L. Gamer, Ein großflächiges magnetisches Kalorimeter zur energie- und ortsauflösenden Detektion von Molekülfragmenten, Master's thesis, Kirchhoff-Institut für Physik, Universität Heidelberg, 2013.

[Gas16]   T. Gassner, High Precision X-Ray Spectroscopy of Highly Charged Heavy
          Ions, PhD Thesis, Friedrich-Schiller-Universität Jena, 2016.

[Gru89]   A. Gruber, W. Bourgeois, B. Franzke, A. Kritzer, and C. Treffert, Internal
          gas-jet target for the esr at gsi, *Nucl. Instr. Meth. Phys. Res. A*, **282**(1),
          87 – 93, 1989.

[Hah92]   W. Hahn, M. Loewenhaupt, and B. Frick, Crystal field excitations in dilute
          rare earth noble metal alloys, *Phys. B.*, **180**, 176–178, 1992.

[Har68]   J. Harding and J. Zimmerman, Quantum interference magnetometry and
          thermal noise from a conducting environment, *Physics Letters A*, **27**(10),
          670 – 671, 1968.

[Hen12]   D. Hengstler, Untersuchung der Eigenschaften von supraleitenden Re-, Zn-
          und Zn:Mn-Absorbern für magnetische Mikrokalorimeter, Diploma thesis,
          Kirchhoff-Institut für Physik, Universität Heidelberg, 2012.

[Hen15]   D. Hengstler, M. Keller, C. Schötz, J. Geist, M. Krantz, S. Kempf,
          L. Gastaldo, A. Fleischmann, T. Gassner, G. Weber, R. Märtin, T. Stöh-
          lker, and C. Enss, Towards fair: first measurements of metallic magnetic
          calorimeters for high-resolution x-ray spectroscopy at gsi, *Physica Scripta*,
          2015(T166), 014054, 2015.

[Her00]   T. Herrmannsdörfer, R. König, and C. Enss, Properties of er-doped au at
          ultralow temperatures, *Phys. B*, **284–288, Part 2**, 1698 – 1699, 2000.

[Her16]   F. Herrmann, Enwicklung und numerische Simulation von supraleiten-
          den Quanteninterferenzdetektoren mit Hilfe von InductEx, B.sc. thesis,
          Kirchhoff-Institut für Physik, Universität Heidelberg, 2016.

[Heu11]   S. Heuser, Entwicklung mikrostrukturierter magnetischer Kalorimeter mit
          verbesserter magnetischer Flusskopplung für die hochauflösende Röntgen-
          spektroskopie, Masters Thesis, Kirchhoff-Institut für Physik, Universität
          Heidelberg, 2011.

[Hoe06]   H. Hoevers, Thermal physics of transition edge sensor arrays, *Nucl. Instr.
          Meth. Phys. Res. A*, **559**(2), 702 – 705, 2006, Proceedings of the 11th
          International Workshop on Low Temperature Detectors.

[Hof12]   V. Hoffmann, Messung der AC-Suszeptibilität von paramagnetischem
          Au:Er bei Temperaturen oberhalb des Spinglasübergangs, B.sc. thesis,
          Kirchhoff-Institut für Physik, Universität Heidelberg, 2012.

[Höl97] G. Hölzer, M. Fritsch, M. Deutsch, J. Härtwig, and E. Förster, $K\alpha_{1,2}$ and $K\beta_{1,3}$ x-ray emission lines of the 3d transition metals, *Phys. Rev. A*, **56**, 4554–4568, 1997.

[Hoo06] A. S. Hoover, M. W. Rabin, C. R. Rudy, D. M. Tournear, D. T. Vo, J. A. Beall, W. B. Doriese, R. D. Horansky, K. D. Irwin, J. N. Ullom, B. L. Zink, and K. E. Chesson, Monte carlo studies of high resolution microcalorimeter detectors, in *2006 IEEE Nuclear Science Symposium Conference Record*, Volume 2, 1268–1272, 2006.

[Hub95] J. Hubbell and S. Seltzer, Tables of X-Ray Mass Attenuation Coefficients and Mass Energy-Absorption Coefficients 1 keV to 20 MeV for Elements Z = 1 to 92 and 48 Additional Substances of Dosimetric Interest, *Nat Inst Stand*, 1995.

[Irw05] K. D. Irwin and G. C. Hilton, Transition Edge Sensors., in C. Enss (Ed.), *Cryogenic Particle Detection, Topics in Applied Physics*, Volume 99, Springer-Verlag, Berlin, heidelberg, New York, 2005.

[Iyo04] N. Iyomoto, J. E. Sadleir, E. Figueroa-Feliciano, T. Saab, S. R. Bandler, C. A. Kilbourne, J. A. Chervenak, D. Talley, F. M. Finkbeiner, R. P. Brekosky, M. A. Lindeman, R. L. Kelley, F. S. Porter, and K. R. Boyce, Optimization of x-ray absorbers for TES microcalorimeters, in *Proceedings of the SPIE*, Volume 5501, 145–154, 2004.

[Jan94] H. Jansen, M. de Boer, R. Legtenberg, and M. Elwenspoek, The black silicon method: a universal method for determining the parameter setting of a fluorine-based reactive ion etcher in deep silicon trench etching with profile control, in *MME '94 Workshop Digest*, 60–64, 1994.

[Joh85] W. Johnson and G. Soff, The lamb shift in hydrogen-like atoms, $1 \leq Z \leq 110$, *Atomic Data and Nuclear Data Tables*, **33**(3), 405 – 446, 1985.

[Jos62] B. D. Josephson, Possible new effects in superconductive tunnelling, *Phys. Lett.*, **1**, 251–253, 1962.

[Kar92] V. Karasiev, L. Labzowsky, and A. Nefiodov, Parity violation in heliumlike uranium, *Physics Letters A*, **172**(1), 62 – 65, 1992.

[Kas56] T. Kasuya, A Theory of Metallic Ferro- and Antiferromagnetism on Zener's Model, *Prog. Theor. Phys.*, **16**(1), 45, 1956.

[Kaz14] G. Kazakov, V. Schauer, J. Schwestka, S. Stellmer, J. Sterba, A. Fleischmann, L. Gastaldo, A. Pabinger, C. Enss, and T. Schumm, Prospects

for measuring the 229Th isomer energy using a metallic magnetic microcalorimeter, *Nucl. Instr. Meth. Phys. Res. A*, **735**, 229 – 239, 2014.

[Kel14] M. Keller, Erster Test eines metallischen magnetischen Kalorimeters am Experimentellen Speicherring ESR der GSI, B.sc. thesis, Kirchhoff-Institut für Physik, Universität Heidelberg, 2014.

[Kem16] S. Kempf, A. Ferring, and C. Enss, Towards noise engineering: Recent insights in low-frequency excess flux noise of superconducting quantum devices, *Applied Physics Letters*, **109**(16), 162601, 2016.

[Kir60] G. Kirchhoff and R. Bunsen, Chemische Analyse durch Spectralbeobachtungen, *Annalen der Physik*, **186**(6), 161–189, 1860.

[Kit05] C. Kittel, Introduction to Solid State Physics, Wiley, 8th. edition, 2005.

[Kla94] I. Klaft, S. Borneis, T. Engel, B. Fricke, R. Grieser, G. Huber, T. Kühl, D. Marx, R. Neumann, S. Schröder, P. Seelig, and L. Völker, Precision Laser Spectroscopy of the Ground State Hyperfine Splitting of Hydrogen-like ^{209}Bi^{82+}, *Phys. Rev. Lett.*, **73**, 2425–2427, 1994.

[Koc07] R. H. Koch, D. P. DiVincenzo, and J. Clarke, Model for $1/f$ Flux Noise in SQUIDs and Qubits, *Phys. Rev. Lett.*, **98**, 267003, 2007.

[Kog81] S. M. Kogan, 1/f noise in spin glasses and in the disordered kinetic ising model, *Solid State Commun.*, **38**(11), 1015 – 1018, 1981.

[Koz00] A. G. Kozorezov, A. F. Volkov, J. K. Wigmore, A. Peacock, A. Poelaert, and R. den Hartog, Quasiparticle-phonon downconversion in nonequilibrium superconductors, *Phys. Rev. B*, **61**, 11807–11819, 2000.

[Koz12] A. Kozorezov, Energy Down-Conversion and Thermalization in Metal Absorbers, *J. Low Temp. Phys.*, **167**, 473–484, 2012.

[Koz13] A. G. Kozorezov, C. J. Lambert, S. R. Bandler, M. A. Balvin, S. E. Busch, P. N. Nagler, J.-P. Porst, S. J. Smith, T. R. Stevenson, and J. E. Sadleir, Athermal energy loss from x-rays deposited in thin superconducting films on solid substrates, *Phys. Rev. B*, **87**, 104504, 2013.

[Kra13a] S. Kraft-Bermuth, V. Andrianov, A. Bleile, A. Echler, P. Egelhof, P. Grabitz, S. Ilieva, C. Kilbourne, O. Kiselev, D. McCammon, and J. Meier, High-precision x-ray spectroscopy of highly charged ions with microcalorimeters, *Physica Scripta*, **2013**(T156), 014022, 2013.

[Kra13b] M. Krantz, Entwicklung, Mikrofabrikation und Charakterisierung von metallischen magnetischen Kalorimetern für die hochauflösende Röntgenspektroskopie hochgeladener Ionen., Master's thesis, Kirchhoff-Institut für Physik, Universität Heidelberg, 2013.

[Kra17] S. Kraft-Bermuth, V. Andrianov, A. Bleile, A. Echler, P. Egelhof, P. Grabitz, S. Ilieva, O. Kiselev, C. Kilbourne, D. McCammon, J. P. Meier, and P. Scholz, Precise determination of the 1s Lamb shift in hydrogen-like lead and gold using microcalorimeters, *Journal of Physics B: Atomic, Molecular and Optical Physics*, **50**(5), 055603, 2017.

[Kub14] K. Kubiček, P. H. Mokler, V. Mäckel, J. Ullrich, and J. R. C. López-Urrutia, Transition energy measurements in hydrogenlike and heliumlike ions strongly supporting bound-state QED calculations, *Phys. Rev. A*, **90**, 032508, 2014.

[Kum16] P. Kumar, S. Sendelbach, M. A. Beck, J. W. Freeland, Z. Wang, H. Wang, C. C. Yu, R. Q. Wu, D. P. Pappas, and R. McDermott, Origin and reduction of $1/f$ magnetic flux noise in superconducting devices, *Phys. Rev. Applied*, **6**, 041001, 2016.

[Lam47] W. E. Lamb and R. C. Retherford, Fine structure of the hydrogen atom by a microwave method, *Phys. Rev.*, **72**, 241–243, 1947.

[Lép08] M. Lépy, J. Plagnard, and L. Ferreux, Measurement of 241Am L X-ray emission probabilities, *Applied Radiation and Isotopes*, **66**(6–7), 715 – 721, 2008, Proceedings of the 16th International Conference on Radionuclide Metrology and its Applications.

[Les16] M. Lestinsky, V. Andrianov, B. Aurand, V. Bagnoud, D. Bernhardt, H. Beyer, S. Bishop, K. Blaum, A. Bleile, A. Borovik, F. Bosch, C. Bostock, C. Brandau, A. Bräuning-Demian, I. Bray, T. Davinson, B. Ebinger, A. Echler, P. Egelhof, A. Ehresmann, et al., Physics book: CRYRING(at)ESR, *European Physical Journal Special Topics*, **225**, 797, 2016.

[Lin07] M. Linck, Entwicklung eines metallischen magnetischen Kalorimeters für die hochauflösende Röntgenspektroskopie, PhD Thesis, Kirchhoff-Institut für Physik, Universität Heidelberg, 2007.

[McC93] D. McCammon, W. Cui, M. Juda, J. Morgenthaler, J. Zhang, R. Kelley, S. Holt, G. Madejski, S. Moseley, and A. Szymkowiak, Thermal calorimeters for high resolution x-ray spectroscopy, *Nucl. Instr. Meth. Phys. Res. A*, **326**(1), 157 – 165, 1993.

[McC05] D. McCammon, Semiconductor Thermistors., in C. Enss (Ed.), *Cryogenic Particle Detection, Topics in Applied Physics*, Volume 99, Springer-Verlag, Berlin, Heidelberg, New York, 2005.

[Möh15] G. Möhl, Optimierung von Ionenätzprozessen zur Herstellung metallischer magnetischer Kalorimeter, B.sc. thesis, Kirchhoff-Institut für Physik, Universität Heidelberg, 2015.

[New30] I. Newton and R. Kirchhoff, Opticks, or a treatise of the reflections, refractions, inflections and colours of light, William Innys, 1730.

[Pie08] C. Pies, Entwicklung eines Detektor-Arrays basierend auf magnetischen Kalorimetern für die hochaufgelöste Röntgenspektroskopie an hochgeladenen Ionen, Masters Thesis, Kirchhoff-Institut für Physik, Universität Heidelberg, 2008.

[Pie12] C. Pies, maXs200: Entwicklung und Charakterisierung eines Röntgendetektors basierend auf magnetischen Kalorimetern für die hochauflösenden Spektroskopie hochgeladener Ionen, PhD Thesis, Kirchhoff-Institut für Physik, Universität Heidelberg, 2012.

[Pla94] D. R. Plante, W. R. Johnson, and J. Sapirstein, Relativistic all-order many-body calculations of the n=1 and n=2 states of heliumlike ions, *Phys. Rev. A*, **49**, 3519–3530, 1994.

[Pob92] F. Pobell, Matter and Methods at Low Temperatures, Springer-Verlag, 1992.

[Pon17] R. Pons, Aufbau und Test eines maXs30-Detektors zur hochauflösenden Röntgenspektroskopie, Masters Thesis, Kirchhoff-Institut für Physik, Universität Heidelberg, 2017.

[Poo95] C. Poole, H. Farach, and R. Creswick, Superconductivity, Academic Press, 1995.

[Por08] F. S. Porter, P. Beiersdorfer, G. V. Brown, W. Doriese, J. Gygax, R. L. Kelley, C. A. Kilbourne, J. King, K. Irwin, C. Reintsema, and J. Ullom, The EBIT Calorimeter Spectrometer: A New, Permanent User Facility at the LLNL EBIT, *Journal of Low Temperature Physics*, **151**(3), 1061–1066, 2008.

[Pow74] R. Powers, P. Martin, G. Miller, R. Welsh, and D. Jenkins, Muonic 197Au: A test of the weak-coupling model, *Nucl. Phys. A*, **230**(3), 413 – 444, 1974.

[Qui01]   W. Quint, J. Dilling, S. Djekic, H. Häffner, N. Hermanspahn, H.-J. Kluge, G. Marx, R. Moore, D. Rodriguez, J. Schönfelder, G. Sikler, T. Valenzuela, J. Verdú, C. Weber, and G. Werth, Hitrap: A facility for experiments with trapped highly charged ions, *Hyperfine Interactions*, **132**(1), 453–457, 2001.

[Rei97]   H. Reich, W. Bourgeois, B. Franzke, A. Kritzer, and V. Varentsov, The ESR internal target, *Nucl. Phys. A*, **626**(1), 417 – 425, 1997.

[Reu06]   R. Reuschl, A. Gumberidze, T. Stöhlker, C. Kozhuharov, J. Rzadkiewicz, U. Spillmann, S. Tashenov, S. Fritzsche, and A. Surzhykov, The Balmer spectrum of H-like uranium produced by radiative recombination at low velocities, *Radiation Physics and Chemistry*, **75**(11), 1740 – 1743, 2006, Proceedings of the 20th International Conference on X-ray and Inner-Shell Processes.

[Rod14]   M. Rodrigues, M. Loidl, C. Pies, A. Fleischmann, and C. Enss, Development of large bismuth absorbers for magnetic calorimeters applied to hard x-ray spectrometry, *J. Low Temp. Phys.*, **176**(3), 610–616, 2014.

[Rös04]   U. Rössler, Solid State Theory: An Introduction, Advanced Texts in Physics, Springer Berlin Heidelberg, 2004.

[Rud54]   M. A. Ruderman and C. Kittel, Indirect exchange coupling of nuclear magnetic moments by conduction electrons, *Phys. Rev.*, **96**, 99–102, 1954.

[Saa07]   T. Saab, E. Figueroa-Feliciano, N. Iyomoto, S. R. Bandler, J. A. Chervenak, R. L. Kelley, C. A. Kilbourne, F. S. Porter, and J. E. Sadleir, Determining the thermal diffusivity in microcalorimeter absorbers and its effect on detector response, *Journal of Applied Physics*, **102**(10), 104502, 2007.

[Sch51]   J. Schwinger, On gauge invariance and vacuum polarization, *Phys. Rev.*, **82**, 664–679, 1951.

[Sch91]   J. Schweppe, A. Belkacem, L. Blumenfeld, N. Claytor, B. Feinberg, H. Gould, V. E. Kostroun, L. Levy, S. Misawa, J. R. Mowat, and M. H. Prior, Measurement of the Lamb shift in lithiumlike uranium (U^{89+}), *Phys. Rev. Lett.*, **66**, 1434–1437, 1991.

[Sch00]   J. Schönefeld,   Entwicklung eines mikrostrukturierten magnetischen Tieftemperaturkalorimeters zum hochauflösenden Nachweis von einzelnen Röntgenquanten, PhD Thesis, Kirchhoff-Institut für Physik, Universität Heidelberg, 2000.

[Sch12]   S. Schäfer, Entwicklung einer Detektorzeile aus metallischen magnetischen Kalorimetern zur hochauflösenden Röntgenspektroskopie an hochgeladenen Ionen, PhD Thesis, Kirchhoff-Institut für Physik, Universität Heidelberg, 2012.

[Sch16]   P. Schneider, Spektroskopische Messungen an Thorium-229 mit einem Detektor-Array aus metallischen magnetischen Kalorimetern, Masters Thesis, Kirchhoff-Institut für Physik, Universität Heidelberg, 2016.

[Sim35]   F. Simon, Application of Low Temperature Calorimetry to Radioactive Measurements, *Nature*, **135**, 763–763, 1935.

[Smi12]   S. J. Smith, J. S. Adams, C. N. Bailey, S. R. Bandler, M. E. Chervenak, J. A.and Eckart, F. M. Finkbeiner, R. L. Kelley, F. S. Kilbourne, C. A.and Porter, and J. E. Sadleir, Small pitch transition-edge sensors with broadband high spectral resolution for solar physics, *Journal of Low Temperature Physics*, **167**(3), 168–175, 2012.

[Spi05]   U. Spillmann, Charakterisierung und erster experimenteller Einsatz von ortsauflösenden, energiedispersiven Germanium-Detektoren zur Präzisionsspektroskopie an schweren Ionen, PhD Thesis, Universität Frankfurt am Main, 2005.

[Swa89]   E. T. Swartz and R. O. Pohl, Thermal boundary resistance, *Rev. Mod. Phys.*, **61**, 605–668, 1989.

[Tao71]   L. J. Tao, D. Davidov, R. Orbach, and E. P. Chock, Hyperfine Splitting of Er and Yb Resonances in Au: A Separation between the Atomic and Covalent Contributions to the Exchange Integral, *Phys. Rev. B*, **4**, 5–9, 1971.

[Tes77]   C. D. Tesche and J. Clarke, dc SQUID: Noise and optimization, *J. Low Temp. Phys.*, **29**(3), 301–331, 1977.

[Vai04]   J. Vaillancourt, C. Allen, R. Brekosky, A. Dosaj, M. Galeazzi, R. Kelley, D. Liu, D. McCammon, F. Porter, L. Rocks, W. Sanders, and C. Stahle, Large area bismuth absorbers for x-ray microcalorimeters, *Nucl. Instr. Meth. Phys. Res. A*, **520**(1–3), 212 – 215, 2004, Proceedings of the 10th International Workshop on Low Temperature Detectors.

[Weg13]   M. Wegner, Entwicklung eines 64-Pixel-Detektor-Arrays basierend auf mikrostrukturierten metallischen magnetischen Kalorimetern mit integriertem Mikrowellen-SQUID-Multiplexer, Masters thesis, Kirchhoff-Institut für Physik, Universität Heidelberg, 2013.

[Wid00] K. Widmann, P. Beiersdorfer, G. V. Brown, J. R. C. López-Urrutia, A. L. Osterheld, K. J. Reed, J. H. Scofield, and S. B. Utter, High–resolution measurements of the K-shell spectral lines of hydrogenlike and heliumlike xenon, *AIP Conference Proceedings*, **506**(1), 444–466, 2000.

[Wil69] G. Williams and L. L. Hirst, Crystal-field effects in solid solutions of rare earths in noble metals, *Phys. Rev.*, **185**, 407–415, 1969.

[Wiß13] V. Wißdorf, Magnetisches 1/f-Rauschen und Imaginärteil der magnetischen Suszeptibilität von Erbium dotiertem Gold bei Millikelvin Temperaturen, B.sc. thesis, Kirchhoff-Institut für Physik, Universität Heidelberg, 2013.

[Yos57] K. Yosida, Magnetic Properties of Cu-Mn Alloys, *Phys. Rev.*, **106**, 893–898, 1957.

[Zao06] R. Zaouk, B. Y. Park, and M. J. Madou, Introduction to microfabrication techniques, in S. D. Minteer (Ed.), *Microfluidic Techniques: Reviews and Protocols*, 5–15, Humana Press, Totowa, NJ, 2006.